THE UNIVERSITY of EDINBURGH

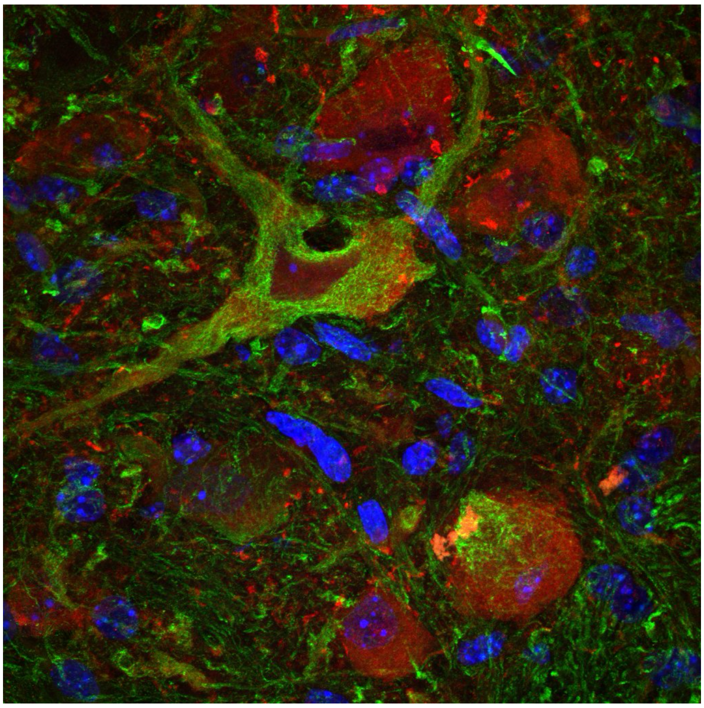

Investigating Pathological Mechanisms in the Thy1-hTDP43 ALS Mouse Model

Zara Lilly Ridgway

Master of Science by Research (MSc by Research)
Thesis

Primary Supervisor: Prof. Tom Gillingwater

Secondary Supervisor: Dr. Helena Chaytow

Word Count: 23,271

Acknowledgments

My deepest thanks and gratitude to Tom and Helena for your constant support and supervision through this project. To Tom, thank you for welcoming me back into the lab for this project and for your constant advice and support throughout the year. To Helena, thank you for your constant and unwavering support throughout this project. Thank you for answering all of my questions, for teaching me all of the methods and skills needed for this project, and for constantly being there to offer advice and support. Both of your support has made me grow immensely as a scientist, for which I will be forever grateful.

A special thanks to Bernát and Hannah Smith. Bernát, thank you for your constant support and for teaching me the qPCR techniques. To Hannah, thank you for teaching me skills in the lab, for answering all of my questions, and for your support over these last couple of weeks.

A further thanks to the whole Gillingwater lab for always being supportive and willing to answer any and all of my questions: Kim, Rachel, Nikky, Kiterie, Federica, Hattie, Abdullah, Hannah Crick, Shahd, Rizwan. All of you have made my time in the Gillingwater Lab an amazing experience that I will never forget.

Additionally, thank you to my parents and grandmother for supporting me during this degree.

Declaration

Unless otherwise acknowledged, the work presented here is entirely my own and has not been submitted for any other qualification.

Zara Ridgway

August 2024

Table of Contents

List of Figures

List of Tables

Abbreviations

ALS – Amyotrophic Lateral Sclerosis

ANOVA – analysis of variants

BCA – bicinchoninc acid

BSA – bovine serum albumin

C9ORF72 – chromosome 9 open reading frame 72

cDNA – complementary deoxyribonucleic acid

ChAT - Anti-Choline Acetyltransferase

CNS – central nervous system

CytC – Cytochrome C

DAPI – 4’ 6-diamidino-2-phnylindole

DS – Donkey Serum

FUS – fused in sarcoma

G3BP1 - Ras GTPase-activating protein-binding protein 1

G3BP2 - Ras GTPase-activating protein-binding protein 2

GCLC - glutamate-cysteine ligase catalytic subunit

GCLM - Glutamate-Cysteine Ligase Modifier Subunit

HMOX1 - heme oxygenase 1

hTDP43 – human TDP43

HuR (also known as ELAV1) - human antigen R or embryonic lethal abnormal vision-like protein 1

iPSC – induced pluripotent stem cell

JAX – Jackson Laboratory

KEAP1 - Kelch-like ECH-associated protein 1

LC3B - microtubule-associated protein 1 light chain 3 beta

MN – motor neuron

MND – motor neuron disease

mNOS - Nitric oxide synthase

MRP1- Multidrug resistance protein 1

mXO - Xanthine oxidase

NLRP3 - nucleotide-binding domain, leucine-rich–containing family, pyrin domain–containing-3

NOX3 - NADPH oxidase 3

NQO1 - NAD(P)H quinone oxidoreductase 1

NrF2 - Nuclear factor erythroid 2-related factor 2

NTg – non transgenic

OCT – optimal cutting temperature

P – postnatal day

P62 or SQSTM1 - sequestosome 1

PBS – phosphate-buffered saline

PCR- polymerase chain reaction

PFA – paraformaldehyde

PVDF – polyvinylidene flouride

qPCR – Quantitive polymerase chain reaction

RIPA – radioimmunoprecipitation assay

ROI – region of interest

ROS – Reactive oxygen species

RT – room temperature

SEM – standard error of the mean

SG – Stress Granule

SOD1- superoxide dismutase 1

SOD2 - superoxide dismutase 2

SPC – spinal cord

TARDBP – TAR DNA-binding protein

TBS -T – tris buffered saline with tween 20

TBS – Tris-buffered saline

TDP43 – TAR DNA-binding protein 43

Tg/0 – heterozygous transgenic

Tg/Tg – homozygous transgenic

Thy-1 – thymocyte differentiation antigen 1

TIA-1 - TIA1 Cytotoxic Granule Associated RNA Binding Protein

TPS – total protein stain

ULK1 - Unc-51-like kinase 1

VCP - Valosin-containing protein

Abstract

Amyotrophic Lateral Sclerosis (ALS) is a fatal neurodegenerative disease caused by the death of both upper and lower motor neuron populations, which are responsible for initiating and controlling movement. ALS is a complex and heterogeneous disease, with only 10% of cases arising from an inherited genetic mutation. Although over 40 genes have been linked to ALS pathology, the cause of disease is still unknown for the vast majority of patients, and treatment options remain limited.

Multiple pathological mechanisms are subsequentially activated in ALS, making the development of therapeutic options difficult. The activation of these pathways does seem to have a common link, causing the generation of cellular stress. The generation of cellular stress induces the activation of many protective mechanisms, such as the formation of stress granules (SGs). SGs are typically transient structures that sequester translationally-stalled mRNA, RNA-binding proteins, ribosomal components, and translation initiation factors to promote cell survival upon stress induction. In ALS and other neurodegenerative diseases, SGs are, however, hypothesised to play pathological roles, with changes in SG composition and morphology observed in ALS models. SGs in ALS are further seen to colocalise with ALS-associated proteins in patient tissues, hinting at a causative role in disease pathogenesis.

SGs have only been investigated in ALS using an external stressor. As SGs are dynamic structures, their composition and morphology have been seen to change depending on the external stressor. Therefore, we sought to investigate the role of SG formation and related mechanisms for the first time *in vivo* without the use of an external stressor using the Thy1-hTDP-43 mouse model. At the late symptomatic disease stage, we found a significant upregulation of SG formation in spinal motor neurons, significant upregulation of SG formation markers in both brain and spinal cord tissue at both the protein level and the transcription level in Tg/Tg mice. These SGs were seen to colocalise with an ALS-associated protein, TDP43, in spinal motor neurons, implying a pathological role for their formation. Additionally, key factors suppressed by protective SG formation were upregulated ROS and NLRP3, indicating altered SG function in ALS. Pathological stress granules are typically broken down by autophagy degradation. Autophagy degradation was unchanged at the time of SG upregulation and significantly decreased at later time points, implying a defective clearance of SGs in the hTDP43 mouse model. As SG formation can occur from several different cellular stress response pathways, we next wanted to explore potential upstream causes of SG formation in ALS. We saw a significant upregulation of inflammation and oxidative stress at the late symptomatic stage, implicating these as possible SG-activating mechanisms. This work identifies a novel pathway that is dysfunctional during ALS disease progression that could present a possible target for future therapeutic options.

Lay Abstract

Amyotrophic Lateral Sclerosis (ALS) is a fatal disease in which nerve cells responsible for controlling movement and survival (motor neurons) die. This disease has a complex genetic history and is extremely fast-acting, with most people dying 3-5 years after symptoms arise. This has made developing treatment options extremely difficult, with only one treatment option currently available in the UK, Riluzole. This drug, however, only lengthens patients' lifespans for a couple of months. Therefore, the development of more treatment options for ALS is needed.

Understanding how the disease develops is essential to developing new treatment options. However, the cause of ALS is still unknown. Therefore, we sought to identify key pathways in the body that could impact ALS development.

Recently, it has been discovered that chronic cellular stress is developed during ALS. Chronic cellular stress causes stress granules to form. Under normal conditions, stress granules are temporary structures that promote cell survival. However, under chronic cellular stress, stress granules can harm the body. In ALS patients, stress granules and ALS-associated proteins have been found in the same cells, indicating that they could be interacting.

Therefore, we sought to determine the role of stress granule formation in ALS. To do this, we used an established ALS animal model, the Thy1-hTDP-43 model. We found significantly more stress granules in motor neurons in disease mice compared to healthy controls. This suggests that stress granule formation is being impacted in ALS. These stress granules were seen to associate with ALS-associated proteins. Additionally, key factors regulated by normal stress granules were significantly upregulated, implying a pathological role for these stress granules. The pathway responsible for breaking down SGs was also not activated at the time of SG formation, and at later time points had decreased activity, implying that these SGs are failing to be broken down during ALS disease. As many pathways within ALS can lead to SG formation, we next wanted to examine pathways that could be causing SG formation in ALS. We found a significant upregulation of oxidative stress and inflammation in disease mice compared to healthy controls, indicating that these pathways could be responsible for SG formation in ALS.

This work suggests that stress granule formation could be playing a role in ALS disease and could, therefore, be a viable treatment target for ALS treatment options.

Introduction

Amyotrophic Lateral Sclerosis (ALS)

Amyotrophic lateral sclerosis (ALS), the most common motor neuron disease (MND), is a fatal neurodegenerative disease in which both upper and lower motor neurons degenerate, causing muscle wasting, paralysis, and eventual death 3-5 years after symptom onset (Brown & Al-Chalabi, 2017). ALS is predominately a sporadic disease, accounting for 90% of cases, with only 10% resulting from an inherited genetic mutation, typically in the genes *SOD1, TARDBP, FUS, or C9ORF72* (Nógrádi et al., 2024). This means that for the majority of people who develop ALS, there is no prior indication that they will develop the disease. Another key feature of this disease is incomplete disease penetrance (Douglas & Baralle, 2023), meaning that not everyone with an ALS mutation will develop ALS. The series of steps that trigger the onset of disease in ALS is unknown, but it is currently believed that ALS is developed through a multistep process in which ALS-associated genetic mutations act as a potential trigger (Chiò et al., 2018). There are currently several established risk factors for ALS development, such as having a family history of ALS, being of advanced age, and male gender (Al-Chalabi et al., 2010; Bagyinszky et al., 2023; Ingre et al., 2015; Logroscino et al., 2010; Manjaly et al., 2010; Niccoli et al., 2017). Several other factors have been associated with ALS, such as environmental toxin exposure, military service, and head injury (Andrew et al., 2021; H. Chen et al., 2007; G. Liu et al., 2021).

The clinical onset of ALS is extremely heterogeneous (Bendotti et al., 2020). Symptom onset typically starts focally, resulting in either a lumbar, bulbar, or respiratory onset (Schram et al., 2020; Verma, 2021). As such, patients at the early onset of ALS often present with a variety of non-specific symptoms, such as tripping or abnormal fatigue in the arms or legs, issues gripping, twitching in the limbs or tongue, slurred speech or trouble swallowing (Verma, 2021). These often mimic symptoms of other neurodegenerative diseases and/or benign physiological states (e.g., muscle twitching), therefore making the disease particularly hard to diagnose (Singh et al., 2018). On average, it takes 8-15 months after initial symptom onset to reach an ALS diagnosis (Paganoni et al., 2014).

After diagnosis, treatment options are incredibly limited for ALS patients. In the UK, there is currently only one treatment option available: riluzole. Riluzole delays disease progression and extends the time to ventilator dependence by 2-3 months to 1 year. (Andrews et al., 2020; Fang et al., 2018; Saitoh & Takahashi, 2020). Another approved drug for use in the US and Europe, Tofersen, similarly has beneficial effects in reducing disease progression (Wiesenfarth et al., 2024). However, Torfersen, an antisense oligonucleotide, works by targeting mutated SOD1 mRNA, reducing SOD1 misfolding and protein aggregation, and, as such, is only useful for patients with SOD1 mutations, a relatively small population of ALS patients (Wiesenfarth et al., 2024).

Chronic Cellular Stress

Despite a growing understanding of the clinical basis of disease, there are still major gaps in understanding the cellular and molecular mechanisms that contribute to disease pathogenesis. Paralysis and death in ALS are driven by the loss of motor neurons, with dysregulation of neuromuscular junctions and synapse loss heavily contributing to motor neuron dysfunction (Aly et al., 2023; McIntosh et al., 2023). However, the reason for this selective degeneration of motor neuron populations in ALS is unknown. Many pathological mechanisms have been found to be dysfunctional in ALS, including oxidative stress, glutamate excitotoxicity, neuroinflammation, RNA dysfunction, and protein aggregation. These pathways are interconnected, making the determination of primary disease mechanisms in ALS particularly difficult (Figure 1).

Mitochondrial dysfunction is a central feature in ALS pathogenesis, with dysregulations occurring early in pathogenesis (Gautam et al., 2022). The dysregulation of mitochondria can be caused by several factors in ALS, including an increase in ROS (reactive oxygen species) production leading to intracellular calcium increase, protein aggregation, inflammation activation, oxidative stress, and glutamate excitotoxicity (Figure 1) (Annunziato et al., 2002; Melachroinou et al., 2013; Smith et al., 2019). Mitochondrial dysfunction, in turn, leads to an increase in ROS, inflammation activation, and oxidative stress (Parvanovova et al., 2024; Peggion et al., 2024). Neuroinflammation, characterized by activation of microglia and reactive astrocytes and infiltration of macrophages and lymphocytes, plays a role in ALS (J. Liu & Wang, 2017). Neuroinflammation can be triggered by the aggregation of proteins, signals from damaged cells, or ROS induction (Béland et al., 2020; Solleiro-Villavicencio & Rivas-Arancibia, 2018; W. Zhang et al., 2023) (Figure 1). Neuroinflammation, in turn, causes mitochondria dysfunction and damages motor neurons (Peggion et al., 2024; W. Zhang et al., 2023). Oxidative stress, occurring when there is an imbalance between the production of ROS and antioxidant species, can be induced by mitochondrial dysfunction, glutamate excitotoxicity, and neuroinflammation (Figure 1). (Cunha-Oliveira et al., 2020; Ikawa et al., 2020; Parfenova et al., 2006; Schubert & Piasecki, 2001; Xiong et al., 2022). Oxidative stress, in turn, causes further damage to mitochondria, neuroinflammation activation, and endoplasmic reticulum stress (Chong et al., 2017; Kowalczyk et al., 2021; Solleiro-Villavicencio & Rivas-Arancibia, 2018). In ALS, TDP43, a nuclear protein, mislocalises to the cytoplasm, causing toxic aggregate formation impairing mRNA transport and causing alterations in alternative splicing, leading to a global mitochondrial imbalance and causing the further generation of ROS, inflammation activation, oxidative stress, and mitochondrial stress (Figure 1) (Alami et al., 2014; W. Zhao et al., 2015; Zuo et al., 2021). Therefore, the pathogenesis leading to ALS is uncertain, with multiple pathways activated in pathogenesis and causing the subsequent activation of each other.

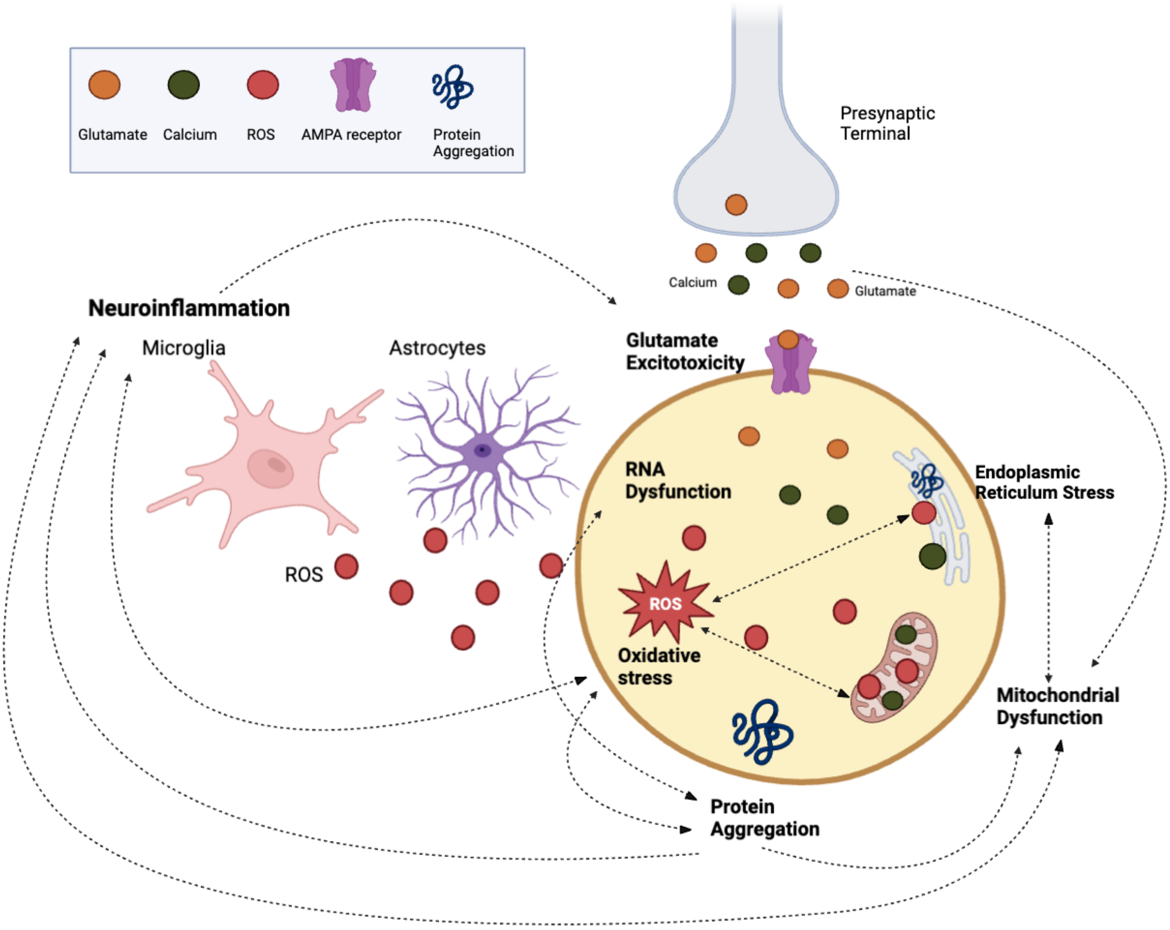

Figure 1: Pathological pathways implicated in ALS development. Multiple pathways are implicated in ALS pathology; however, whether they play primary or secondary roles in pathogenesis is still debated. These pathways are interconnected and can cause subsequent activation of each other (indicated by dashed lines). Created using BioRender.

However, a common theme with regard to the activation of all of these pathways is the generation of cell stress. Therefore, it is likely that in motor neurons - which are highly specialised cells - the generation of chronic cellular stress during ALS disease pathogenesis exceeds the threshold that can be compensated for, leading to degeneration.

Chronic cellular stress caused by the activation of deleterious pathways leading to protein, RNA, DNA, and lipid damage leads to the induction of reactive oxygen species (ROS) such as superoxide anions, hydrogen peroxide, hydroxyl radicals, and xanthine oxidase (Poljšak & Milisav, 2012). To counteract ROS production, protective pathways are activated, including the NrF2-ARE pathway. The Nrf2-ARE pathway plays essential roles in reducing ROS production, oxidative stress, and inhibiting cellular death pathways through the production of antioxidant enzymes (Figure 2). Motor neurons, however, have decreased antioxidant enzyme production compared to other cell types, possibly contributing to the selective death of motor neurons. In ALS, a decrease in the Nrf2-ARE pathway has been observed, allowing the perturbation of ROS and oxidative stress (Bono et al., 2021; Hemerková & Vališ, 2021). Decreased production of Nrf2-ARE pathway antioxidants leads to the accumulation of lipid peroxidation triggering the ferroptosis cell death pathway, a pathway implicated to play roles in motor neuron cell death in ALS (Yan et al., 2023). Dysregulation in this pathway, therefore, is suggested to have a pathological role in ALS, with mutations in antioxidant enzymes, SOD1, seen to cause ALS (Gagliardi et al., 2023). The dysregulation of this pathway further enables the production of ROS, leading to further motor neuron damage through the activation of deleterious pathways such as oxidative stress.

A

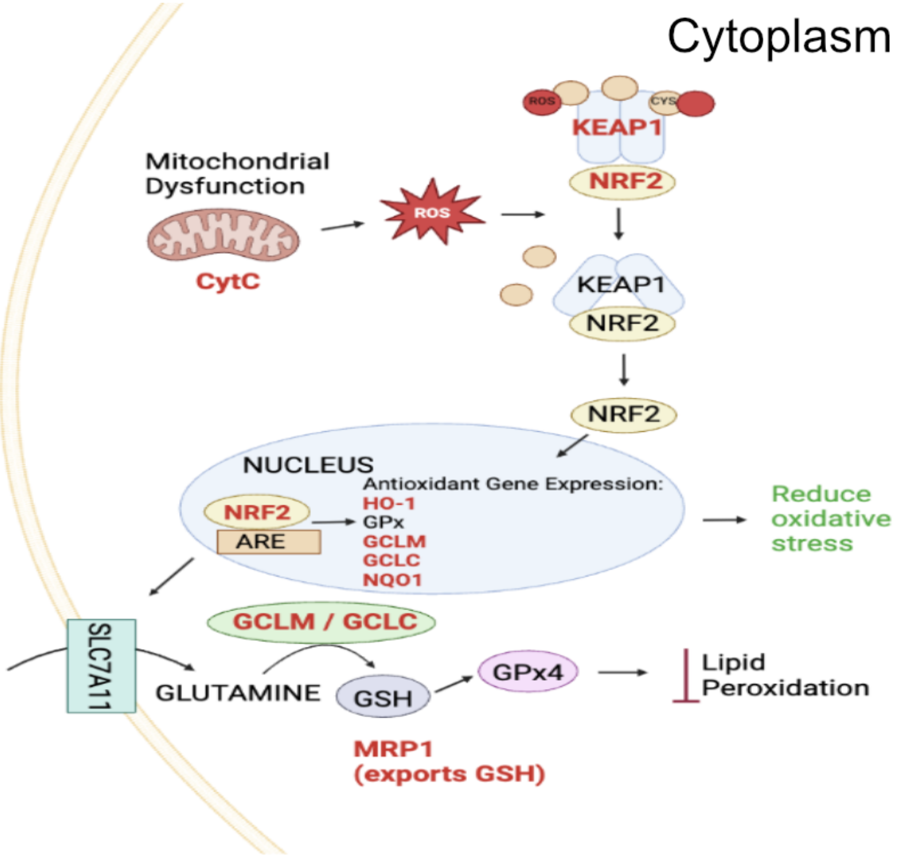
Cytoplasm
ROS
CYS
KEAP1
NRF2
Mitochondrial Dysfunction
CytC
ROS
KEAP1
NRF2
NRF2
NUCLEUS
Antioxidant Gene Expression:
NRF2
ARE
HO-1
GPx
GCLM
GCLC
NQO1
Reduce oxidative stress
SLC7A11
GCLM / GCLC
GLUTAMINE
GSH
GPx4
Lipid Peroxidation
MRP1 (exports GSH)

B

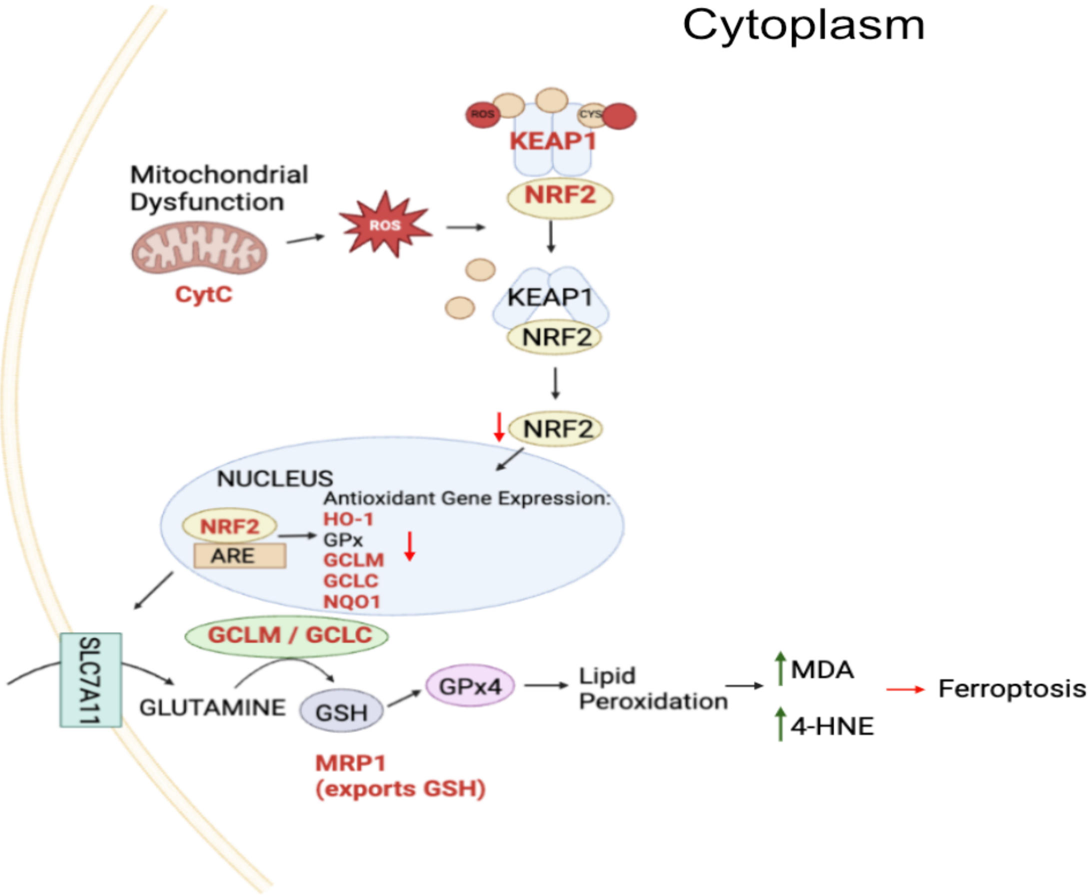
Cytoplasm
ROS
CYS
KEAP1
NRF2
Mitochondrial Dysfunction
CytC
ROS
KEAP1
NRF2
NRF2
NUCLEUS
Antioxidant Gene Expression:
NRF2
ARE
HO-1
GPx
GCLM
GCLC
NQO1
SLC7A11
GCLM / GCLC
GLUTAMINE
GSH
GPx4
Lipid Peroxidation
MDA
4-HNE
Ferroptosis
MRP1 (exports GSH)

Figure 2: NrF2-ARE pathway dysfunction in ALS A. Schematic showing the regular functioning of the NrF2-ARE pathway. NrF2-ARE is a protective pathway that, when activated, works to reduce oxidative stress by activating antioxidants and also inhibits ferroptosis from occurring through its inhibition of lipid peroxidation. This inhibition relies on the production of key antioxidants (GCLM, GCLC, GPx4) which inhibit both lipid peroxidation and ferroptosis through the SLC7A11/GPX4 axis. B. Schematic showing NrF2-ARE pathway function in ALS. In ALS, there is decreased activity of the pathway, leading to decreased transcription of antioxidants, causing oxidative stress to persist and activation of the ferroptosis death pathway. The production of Nrf2-ARE antioxidants inhibits the ferroptosis cell death pathway through the SLC7A11/GPX4 axis through inhibiting lipid peroxidation. However, when there is decreased antioxidant gene expression, key elements of this axis (GCLM, GCLC, GPx4) are not produced thereby allowing lipid peroxidation. Lipid peroxidation then causes the build-up of malondialdehyde (MDA) and 4 hydroxy-2-nonenal (4-HNE) which trigger the ferroptosis cell death pathway. Red bolded elements indicate specific aspects investigated in this project. Created with BioRender.

Increased levels of ROS cause an increase in intracellular calcium in motor neurons through the binding of ROS to plasma membranes, ion channel proteins, and sarco/endoplasmic reticulum ca+2 ATPase transporters (SERCA), leading to mitochondrial dysfunction and endoplasmic reticulum stress (Annunziato et al., 2002; Kiselyov & Muallem, 2016; A. Li et al., 1998; Melachroinou et al., 2013). Motor neurons have a low amount of calcium ions present intracellularly and also lack calcium-binding proteins such as parvalbumin and calbindin-D28K that would aid in the regulation of calcium (Alexianu et al., 1994; Halliwell, 2006). Therefore, this increase in intracellular calcium can cause damage to motor neurons and death by causing mitochondrial dysfunction, endoplasmic reticulum stress, and ROS production (Annunziato et al., 2002; Bernardi et al., 2023; Kiselyov & Muallem, 2016; Melachroinou et al., 2013). This, therefore, creates a detrimental feedback loop in which there is further increased ROS production, further causing dysregulation and death of motor neurons.

Treatments targeting chronic cellular stress in ALS have been seen to have beneficial outcomes. Edavorone, a newly approved ALS drug, is a free ROS scavenger and has been seen to halt ALS disease progression in ALS patients by reducing ROS (Cho & Shukla, 2021), thus indicating that the induction of chronic cellular stress is an important pathological feature and presents a targetable aspect for treatment options.

Stress Granules (SGs)

This induction of chronic cellular stress causes the activation of protective pathways to achieve cellular homeostasis. Under conditions of cellular stress, multiple kinases are activated, which causes the phosphorylation of eIF2α kinase (Wek, 2018) (Figure 3). The phosphorylation of eIF2α, a kinase crucial for initiating protein synthesis, causes a global translation inhibition, resulting in the accumulation of untranslated messenger RNP complex and polysomes in the cytoplasm (Figure 3). This then causes the recruitment of stress granule nucleators (G3BP1 and G3BP2) to form multimers, leading to the formation of stress granules (Matsuki et al., 2013) (Figure 3). These stress granules form mature structures, forming a stable core structure surrounded by a less concentrated shell through the recruitment of translationally stalled mRNA, RNA-binding proteins (G3BP1, G3BP2, TIA-1, and HuR), ribosomal components, and translation initiation factors (eIF3, eIF4E, and eIF4G) (Campos-Melo et al., 2021) (Figure 3). The formation of stress granules plays crucial protective roles in regard to homeostasis, with their main role being pausing translation to allow the cell to recover from stress.

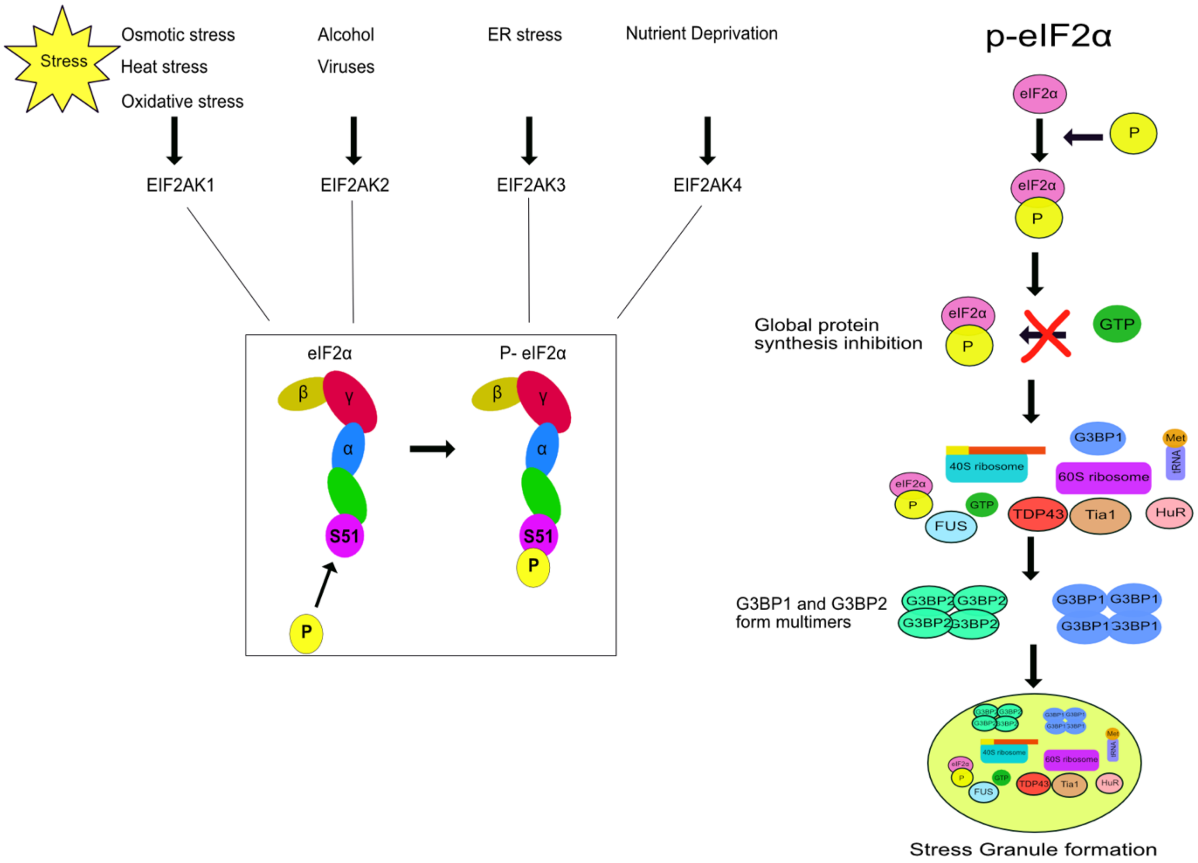

Figure 3: Stress Granule formation. Upon the induction of chronic cellular stress, eIF2α becomes phosphorylated, leading to a global halt in protein homeostasis. In response, G3BP1 and G3BP2 form multimers forming stress granules, which disassembled translation initiation complexes, along with many RNA-binding proteins (such as G3BP1, G3BP2, HuR, and TiaR), are incorporated into.

The formation of stress granules is extremely dynamic, with differences in SG composition and properties dependent on cell type, stressor, and stress duration. Multiple stressors, including mitochondrial, oxidative, hypoxic, thermal, endoplasmic reticulum, and osmotic stress, can induce SG formation, however these SG have been shown to differ depending on the stress-inducing trigger (Campos-Melo et al., 2021; Desai & Bandopadhyay, 2020). Despite these differences in composition, short-term cellular stress largely triggers the formation of canonical SGs which contain proapoptosis factors such histone deacetylase 6 (HDAC6), JUN N-terminal kinase (JNK), receptor of activated protein C kinase 1 (RACK1), Ras homolog family member A (RhoA), suppressing their function (Campos-Melo et al., 2021). These canonical SGs, therefore, prevent apoptosis and promote cell survival by inhibiting protein translation of pro-apoptotic factors.

These SGs have also been observed to play secondary roles in regulating homeostasis, including inhibiting inflammasome activation, maintaining proteostasis, reducing mitochondrial dysfunction, and oxidative stress-linked nucleocytoplasmic transport (Dudman & Qi, 2020). For brevity, focus will now be placed on SGs relationship with inflammation and oxidative stress.

SGs and inflammation have a direct role in regulating one another. Upon the induction of inflammation, pro-inflammatory cytokines are released, such as tumor necrosis factor-alpha (TNF-α) and interferon-gamma (IFN-y) that phosphorylate eIF2α inducing SG formation in mouse epithelial cells (S. Hu et al., 2010). SG formation then works to directly inhibit inflammation through inhibiting NLRP3 inflammasome activation.

NLRP3 inflammasome activation is a central component in the inflammatory response, activating caspase-1 and causing the release of pro-inflammatory cytokines IL-1B and IL-18 (Blevins et al., 2022). NLRP3 inflammasome also activates the membrane pore-forming gasdermin D (GSDMD), a protein involved in the pyroptosis cell death pathway, causing cell death (Malik & Kanneganti, 2017). Upon SG formation, DDX3X, a component of SGs and a main activator of the NLRP3 inflammasome, is sequestered into the granule, thus inhibiting inflammasome activation and, furthermore, inhibiting pyroptosis (Samir et al., 2019). NLRP3 inflammasome activation conversely inhibits SG formation. A key common step in NLRP3 inflammasome activation, the decrease in intracellular potassium concentration, inhibits SG formation (Yoshioka et al., 2024). Thus, the inflammation activation triggers SG formation, which in turn reduces the inflammatory response.

SGs and oxidative stress also have a direct role in regulating one another. Oxidative stress induces phosphorylation of eIF2α, leading to SG formation (Wu et al., 2023). SGs, in turn, interact with mitochondria by regulating metabolic functions and reducing oxidative stress. SG formation causes downregulations of fatty acid beta oxidation by reducing mitochondrial voltage-dependent anion channels responsible for importing fatty acids into the mitochondria (Amen & Kaganovich, 2021). This decrease in fatty acid beta oxidation reduces the amount of oxidative stress and damage in cells (Amen & Kaganovich, 2021).

Thus, SGs play key roles in inflammasome inhibition, mitochondrial homeostasis, oxidative stress, and nucleocytoplasmic transport, enabling cell survival upon the insult of cellular stress (Dudman & Qi, 2020). Upon the alleviation of cellular stress in healthy cells, these SGs readily disable, allowing for protein synthesis and normal cellular functions to resume (Marcelo et al., 2021).

Proposed Role of Stress Granules in ALS

Despite the largely protective role attributed to SG formation, in cases of chronic cellular stress, SG components can be modified to cause non-canonical SG formation that has altered functioning. In cases of chronic cellular stress, SGs composition differs losing factors such as eukaryotic translation initiation factor 3B (eIF3B), RACK1, and caspase 3 and 7 causing a shift towards pro-apoptotic functions (Campos-Melo et al., 2021; Fujikawa et al., 2023; Fujimura et al., 2012; E. F. Lee et al., 2014; Reineke & Neilson, 2019). Changes in SG components have been denoted in ALS, with FUS SGs having diminished nucleocytoplasmic transport factors, proteasome subunits, depleted signal transduction proteins, depleted disassembly factors, increased splicing factors, and mitochondrial proteins compared to normal SGs (An et al., 2022). Similarly, in human bone cells with ALS-associated C9ORF72 dipeptides expressed, depletion of multiple classical stress granule proteins, including essential SG clearance factors such as SUMO-conjugating enzymes, were observed in SGs (Marmor-Kollet et al., 2020). SUMO-conjugating enzymes play key roles in SG disassembly; thus, the lack of these factors indicates a persistent role for SGs in ALS (Hofmann et al., 2021). In a C9ORF72 mutant model, the overexpression of UBE2I, a sumo-conjugating enzyme, alleviated eye degeneration, thus indicating that increasing SG disassembly could be beneficial in ALS (Marmor-Kollet et al., 2020). Taken together this indicates persistent SGs are formed during ALS pathology.

The presence of these SGs was found at early disease stages in patient spinal cords with mutations in core SG proteins, Ataxin-2 and TIA1, additionally linked to ALS development (Elden et al., 2010; Mackenzie et al., 2017). In ALS, key ALS disease-associated proteins (TDP43, FUS, and SOD1) are observed to colocalise with SGs (Cui et al., 2024). FUS, an RNA binding protein, regulates expressions of genes involved in cell adhesion, synaptogenesis, and apoptosis, as well as having roles in alternative splicing (De Santis et al., 2017). ALS-associated FUS mutations cause slicing changes in over 300 genes in genes involved in axonal growth and cytoskeletal organization and mRNA alterations (Lagier-Tourenne et al., 2012; Reber et al., 2016). TDP43 plays critical roles in regulating mRNA transport, alternative slicing, and regulates the expression of multiple mRNAs (Fiesel & Kahle, 2011). In ALS, TDP43 dysfunction is a central disease feature, with TDP43 aggregation observed in 97% of all patients, irrespective of whether patients carry a mutation in the *TARDBP* gene (Suk & Rousseaux, 2020). Thus, irrespective of disease cause, TDP43 mislocalisation is present, presenting a unifying factor in an extremely heterogeneous disease.

TDP43 mislocalisation induces vacuole fragmentation, abnormal protein clearance, inflammation activation and desensitises the cell to respond disproportionately to incoming signals, thereby increasing the damage caused by ROS and oxidative stress (Leibiger et al., 2018; W. Zhao et al., 2015). Additionally, TDP43 mislocalization causes a significant increase in stress granule formation, increased cellular stress response, and increased cell death (Q. Ding et al., 2021; Mann et al., 2019; Smethurst et al., 2020). TDP43 is able to localise to SGs through the PAR-binding motif and is able to impact SG components and function (McGurk et al., 2018). Through a global proteomic study performed in HEK 293 and HeLa cells, TDP43 was identified to interact with multiple SG components, including TIA1, EIF2C2, G3BP, and EIF4G, causing alterations in SG nucleation and secondary aggregation of SGs (Liu-Yesucevitz et al., 2010a; McDonald et al., 2011).

The exact mechanism by which SGs contribute to pathology is unknown. The recruitment of TDP43 to SGs, leads to TDP43 becoming insoluble and immobilised and thus might act as a potential trigger to TDP43 aggregation in ALS (Cui et al., 2024). The persistence of TDP43 aggregates is seen after inhibition of stress and SG disassembly, suggesting that these SGs may act as essential mechanisms for the formation of TDP43 aggregates but aren't required for later pathological stages (Cui et al., 2024).

Modulating SG dynamics has been shown to reduce ALS pathology in multiple models. In ALS animal models, eIF2α phosphorylation is upregulated (D. Chen et al., 2015; Kim et al., 2014). Genetic and pharmacological inhibition of eIF2α phosphorylation rescued TDP43 toxicity in an ALS *Drosophila* model and mammalian primary neurons, implying that inhibiting SG formation is beneficial in ALS (Kim et al., 2014). Additionally, treatment with SG modulators, cycloheximide and emetine, in cells overexpressing an TDP43 mutant inhibited TDP43 aggregation (Liu-Yesucevitz et al., 2010a). In C9ORF72 patient iPSC-derived neurons inhibiting c-Jun N-terminal kinase (JNK) pathway activation, which is responsible for SG formation, suppressed SG formation and neurotoxicity (Sahana et al., 2023).

Multiple treatments that have protective effects in ALS have been found to alter SG dynamics. Trehalose, which has been shown to delay disease onset and increase lifespan in SOD1 mutant ALS mice, affects SG disassembly by regulating eIF2 α (Castillo et al., 2013; Dimasi et al., 2017). Rapamycin, a drug shown to have a beneficial effect in ALS, inhibits SG formation (L. D. Hu et al., 2022). Taken together, this suggests that despite SG's protective role under normal conditions, in ALS SG formation could be playing a deleterious role.

Autophagy-Dependent Degradation of SGs

SGs are kept in homeostatic balance largely through the autophagy pathway. The autophagy pathway is responsible for breaking down SGs upon the alleviation of cellular stress and upon the formation of pathological SGs (Ryan & Rubinsztein, 2024a; Ryu et al., 2014). Dysfunctions in autophagy play a role in ALS, with both an increase and a decrease evident in different ALS models (Amin et al., 2020; Beckers et al., 2023). The knockdown of autophagy proteins (ATG3, ATG5, ATG7) resulted in the accumulation of SGs without the induction of stress in mammalian cells (Chitiprolu et al., 2018; Krisenko et al., 2015; Ryu et al., 2014). Additionally, multiple autophagy proteins such as p62, LC3B, ULK1, and VCP colocalize with SGs and SG proteins have been found inside structures resembling autolysosomes, indicating a role in autophagy for SG degradation (Chitiprolu et al., 2018)(Figure 4).

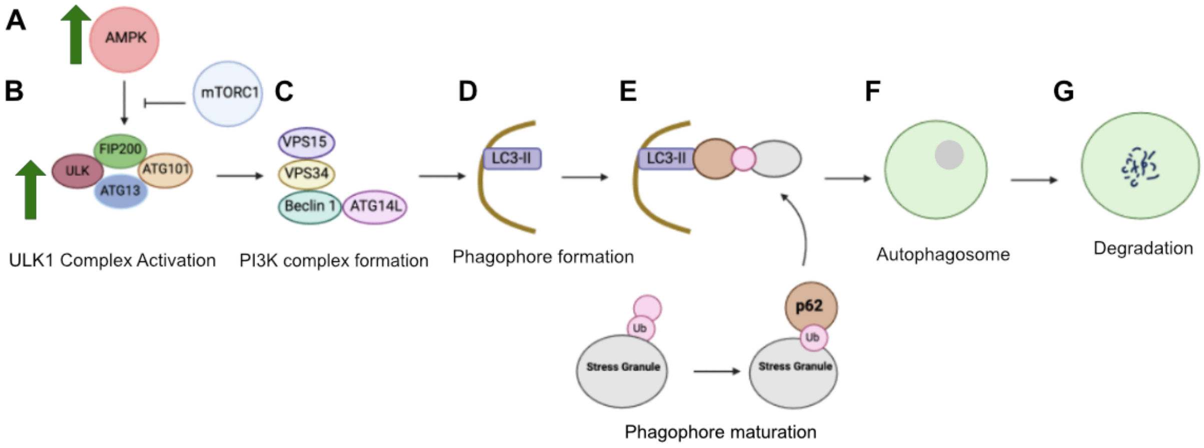

Figure 4: Schematic overview of SG degradation by autophagy. A. AMPK activates autophagy while activation of mTORC1 inhibits autophagy. B. AMPK upregulation leads to the formation of the ULK1 complex: ULK1/2, FIP200, ATG101, ATG13. C. ULK1 complex activation triggers PI3K complex formation: VPS15, VPS34, Beclin-1, and ATG14L. D. PI3K complex formation triggers phagophore formation. LC3B-II then binds to the phagophore, regulating the closure of the phagophore (Y. K. Lee & Lee, 2016). E. Stress granules are marked for degradation by ubiquitin. P62 then binds to ubiquitin, transporting the stress granule into the phagophore. F. The phagophore closes and forms an autophagosome. G. The autophagosome then degrades the stress granule, allowing normal translation to then continue. Figure created using BioRender.

In Hela cells with overexpressed C9ORF72, p62 is attached to the periphery of 20-30% of SGs with LC3 coating p62 upon arsenite stress induction (Chitiprolu et al., 2018). LC3 is an essential part of the elongating phagophore, indicating autophagy was occurring (Chitiprolu et al., 2018) (Figure 4D-E). LC3 has previously been seen to localise to SGs under a variety of stress conditions (Ryu et al., 2014; Seguin et al., 2014). P62 localises to SGs and interacts with G3BP1 and G3BP2 (C. Yang et al., 2023) (Figure 4E). Additionally, the knockdown of p62 resulted in defective SG clearance, indicating a central role for P62 in SG clearance. *In vivo* P62 forms phase-separated liquid droplets in response to binding to SGs (Krause et al., 2022; Sun et al., 2018; Zaffagnini et al., 2018). These P62 liquid droplets act as sites for autophagosome formation with core autophagy proteins (ULK1, FIP200, ATG16L1, AIPI2) all found to be recruited to the outside of the droplets with multiple double membraned structures forming (Kageyama et al., 2021). These p62 droplets can serve as platforms with either selective autophagy or bulk autophagy (Kageyama et al., 2021).

ULK1 and ULK2 also co-localise with SGs and promote their clearance in an autophagy-independent manner (B. Wang et al., 2019) (Figure 4B). SG clearance is accelerated by an ULK1/2 agonist, while inhibition impairs the clearance of SGs and causes TDP-43 positive inclusions, indicating a primary role for ULK1/2 in SG regulation (B. Wang et al., 2019). ULK1 and ULK2 phosphorylates VCP, a multifactorial chaperone-like AAA-ATPase, increasing its activity (B. Wang et al., 2019). In mammalian cells, VCP colocalises with SGs under several different stressors (Buchan et al., 2013). VCP mediates the degradation of substrates by either the ubiquitin-proteasome system or the autophagy-lysosome system (Jentsch & Rumpf, 2007; Meyer et al., 2012). VCPs roles in regulating autophagy are dependent on Beclin-1 (Hill et al., 2021) (Figure 4C). Inhibition of VCP impaired the clearance of SG under arsenite and heat-induced stressors; however, inhibition under other stressors has little effect on SG formation, therefore suggesting a stressor-dependent response to clearance (Tolay & Buchberger, 2021). Mutations in VCP have been associated with causing ALS, leading to 1-2% of fALS cases (Koppers et al., 2012). Autophagy is, therefore, an important mechanism in SG regulation, breaking down SGs when the stressor is alleviated or breaking down pathological SGs to inhibit disease progression.

Animal Models of ALS

To understand the role of stress granules in ALS in an *in vivo* context, animal models are an incredibly useful tool. In ALS, it has become increasingly apparent that noncell autonomous mechanisms such as neuroinflammation and proteostasis imbalance play significant roles in ALS pathology. As such, the use of animal models which can recapitulate this multi-cell environment has become a vital tool in identifying the role of these pathways in ALS.

Many animal models have been developed for ALS, including Caenorhabditis elegans (C. elegans), zebrafish, *drosophila* and mouse models. Most animal models used for ALS research have homologs for genes associated with causing ALS in humans, making them valuable models in studying both ALS disease pathogenesis and investigating viable treatment options (Chai et al., 2008). These models, however, do not model ALS perfectly and do have limitations; therefore, the use of multiple model systems in ALS research is needed to advance the field.

Simple model systems such as Caenorhabditis elegans (C. elegans), zebrafish, and drosophila are incredibly useful for the identification of pathological mechanisms in neurodegenerative diseases with a high degree of conserved genes and processes compared to humans (X. Chen et al., 2015; Cotterill & Yamaguchi, 2024; Oliveira et al., 2023). C. elegans have been primarily used to investigate pathological mechanisms benefiting from a translucent body, distinctive behavioral phenotypes, and characterized nervous systems (X. Chen et al., 2015). Zebrafish are incredibly useful for testing therapeutic options, with large clutch sizes, embryos developing ex vivo, fast development transparent bodies, and numerous transgenic lines available (Oliveira et al., 2023). ALS model zebrafish also induce a reliable axon pathology, causing shorter and more branched motor axons, creating a distinct phenotype to evaluate the effectiveness of therapeutics (Oliveira et al., 2023). *Drosophila* has been used as a genetic model for ALS, with transgenic ALS flies reliably producing ALS phenotypes such as mitochondrial dysfunction, motility, axonal transport, shorter lifespan, and cellular inclusions (Baldwin et al., 2016; Y. Li et al., 2010; Sanhueza et al., 2014; Yamaguchi et al., 2021).

Mice display high physiological, anatomical, and genomic proximity with humans (Bryda, 2016). Most ALS mouse models replicate hallmarks of ALS, with protein inclusions in glial and neuronal cells, motor neuron degeneration, and progressive muscle weakness and paralysis (Bonifacino et al., 2021; Philips & Rothstein, 2015). Genetic mouse models have been primarily used in ALS research, with SOD1 models being the most common. However, these models lack key clinical features observed in the majority of ALS patients, such as the aggregation of TDP43 inclusions, and have lacked success in translating effective therapies to humans (Stephenson & Amor, 2017).

TDP43 mutant ALS mouse models have therefore been created, such as the Thy1-TARDBP model (hTDP43), which exhibits an overexpression of human *TARDBP* in neuronal cells (Wils et al., 2010). As the majority of ALS patients do not have a genetic mutation, but do contain TDP43 pathology, a TDP43 overexpression model may offer greater translatability for research to the patient population. The hTDP43 mouse model has been extensively used for ALS research over the past decade, with hTDP43 homozygous mice developing a severe ALS-like phenotype and recapitulating many pathological features present in ALS patients with evident neuroinflammation, motor neuron loss, progressive hindlimb weakness, NMJ denervation in hindlimb muscles, cytoplasmic mislocalisation of TDP43, and mitochondrial dysfunction (Alhindi et al., 2023; Chaytow et al., 2022; Wils et al., 2010). Thus, the hTDP43 mouse model has become invaluable in ALS research for both investigating mechanisms and therapeutic options.

Hypothesis and Aims

Due to these aforementioned reasons, investigating the role of SG formation in ALS may lead to a deeper understanding of ALS pathology and the mechanisms that drive it. SG formation in ALS has primarily been investigated using *in vitro* models, with conflicting reports suggesting either an increase or decrease in SG formation being implicated in disease pathogenesis (Besnard-Guérin, 2020; Fernandes et al., 2018).

Little work has been done to evaluate the role of SG formation *in vivo*, with only two studies currently in the literature. These studies both used acute stressors and found a significant decrease in SG formation in ALS animal models (Dubinski et al., 2023; X. Zhang et al., 2020).

Differences in SG dynamics in ALS models could be due to a number of reasons. All of these previous studies have made use of an external stressor to stimulate stress granule formation. Many different external stressors have been used during investigations including sorbitol, arsenite, oxidative stress, hyperthermia, and oxalate (Colombrita et al., 2009; Dewey et al., 2011; Dubinski et al., 2023; Ratti et al., 2020).

As previously discussed, SG morphology and composition are seen to differ depending on the external stressor used (Campos-Melo et al., 2021; Desai & Bandopadhyay, 2020; Ratti et al., 2020). Therefore, in ALS, it is unknown whether there is an increase or decrease in SG formation present as a direct result of intrinsic pathology.

Therefore, during this project, we aimed to analyse the role of SG formation in ALS *in vivo*. As SG formation has not been investigated *in vivo* without the use of an external stressor, we therefore sought to fill this gap in understanding using the hTDP43 mouse model. Due to previous research, it was hypothesised that **SGs play a pathological role in ALS pathogenesis *in vivo***.

First, we aimed to determine whether there are changes in SG formation in the hTDP43 mouse model *in vivo*. We therefore sought to determine whether SGs can be visualised without the use of an external stressor, whether there is an increase or decrease in SG formation, and the disease stage in which SG dynamics are altered in the hTDP43 mouse model.

Secondly, we aimed to determine what chronic cellular pathways could be leading to altered SG dynamics in ALS. We selected two established chronic cellular stress pathways, neuroinflammation, and oxidative stress, and sought to determine whether they could induce SG formation.

Next, we aimed to determine whether SG formation plays a pathological role in ALS. Previous evidence has hinted that SGs are pathological in ALS, with an increase in eIF2α phosphorylation and alterations in SGs being reported. However, this pathological role has not been investigated in an *in vivo* setting. Therefore, we sought to determine whether SGs are pathological through analysing key factors that SGs regulate upon formation: ROS and NLRP3 inflammasome activation.

Next, we aimed to determine whether there are changes in the autophagy degradation pathway that could be contributing to the pathological role of SGs in ALS. Therefore, using autophagy markers (ULK1, p62, Beclin, LC3B), we sought to determine whether there were changes in autophagy at the same time point as alterations in SG dynamics in the hTDP43 mouse model.

Finally, we aimed to determine whether SG dynamics could be restored *in vivo*. Previous beneficial treatment options have been seen to restore SG dynamics, such as the use of Ataxin-2 ASO therapies, SG inhibitors, rapamycin, and trehalose, hinting that restoring SG dynamics might be an important aspect to alleviate ALS pathology (Becker et al., 2017; Dimasi et al., 2017; Elden et al., 2010; Mandrioli et al., 2018). Therefore, we sought to determine whether terazosin, a drug which improves motor phenotypes in multiple ALS models by targeting PGK1, restores SG dynamics *in vivo* (Chaytow et al., 2022).

Materials and Methods

Animal Model

Mice were maintained under the project license PPL P92BB9F93 and Personal Licenses IAC4805FD and 1567597.

The hTDP-43 mouse model, B6; SJL-TG(Thy1-TARDBP)4Singh/J mice (JAX stock #012836), was obtained from Jackson Laboratory. In this mouse model, human *TARDBP*, an ALS-linked protein, is overexpressed under the murine neuron-specific mThy1 promoter, causing evident motor neuron pathology in homozygous mice (Tg/Tg) (Wils et al., 2010). Tg/Tg mice develop a severe ALS-like phenotype, resulting in progressive hindlimb weakness and eventual paralysis (Alhindi et al., 2023). Animals were maintained under a standard 10-hour light, 14-hour dark cycle at the University of Edinburgh. Experimental animals were obtained by breeding heterozygous mice (Tg/0), resulting in Tg/Tg, Tg/0, and control littermates (NTg). As hTDP-43 mice developed a severe phenotype affecting quality of life, a severity limit was established prior to experimentation. From postnatal day (P)15, the recorded pre-symptomatic stage of this mouse model (Wils et al., 2010), mice were evaluated daily for severity using an established clinical scoring system (Alhindi et al., 2023; Chaytow et al., 2022). Mice were culled at the desired time point or if the predetermined severity limit was reached. Both sexes were used throughout the experimentation.

Genotyping PCR

hTDP-43 mice genotypes were determined through PCR using the quick DNA purification protocol (Truett et al., 2000). DNA was extracted from ear notches of each individual mouse using 50µl of “hotshot lysis buffer” (Table 3) at 95°C for 30 minutes. Afterward, the sample was neutralised using 50µl of neutralising buffer and mixed via flicking (Table 3). 2µl of DNA was added to 14µl of the master mix (Table 3). A negative control was utilized for each gel, consisting of 2µl of DEPC-free H20 and 14µl of master mix to check for contamination within the master mix (Table 3).

The samples were then run with the recommended reagents on the recommended JAX touchdown TDP-43 program for this mouse model (protocol 25492 from Jackson Laboratory) using the T100 thermal cycler (BioRad). Samples were heated at 94°C for 2 minutes, followed by heating at 94°C for 20 seconds for 10 cycles, then at 65°C for 15 seconds with a 0.5°C decrease occurring per cycle, and 68°C for 10 seconds. The samples were then heated for 28 cycles at 94°C for 15 seconds, 60°C for 15 seconds, and 72°C for 10 seconds. Afterward, samples were heated at 72°C for 2 minutes before they were held at 12°C until needed.

Genotypes were then determined by running samples on a 1.5% agarose gel with an 100bp ladder (Newtown) at 120 volts for 20 minutes. Genotypes were detected by the presence of the TDP-43 WT murine band at 303bp and/or the human transgenic TDP-43 band at 500bp (Figure 5).

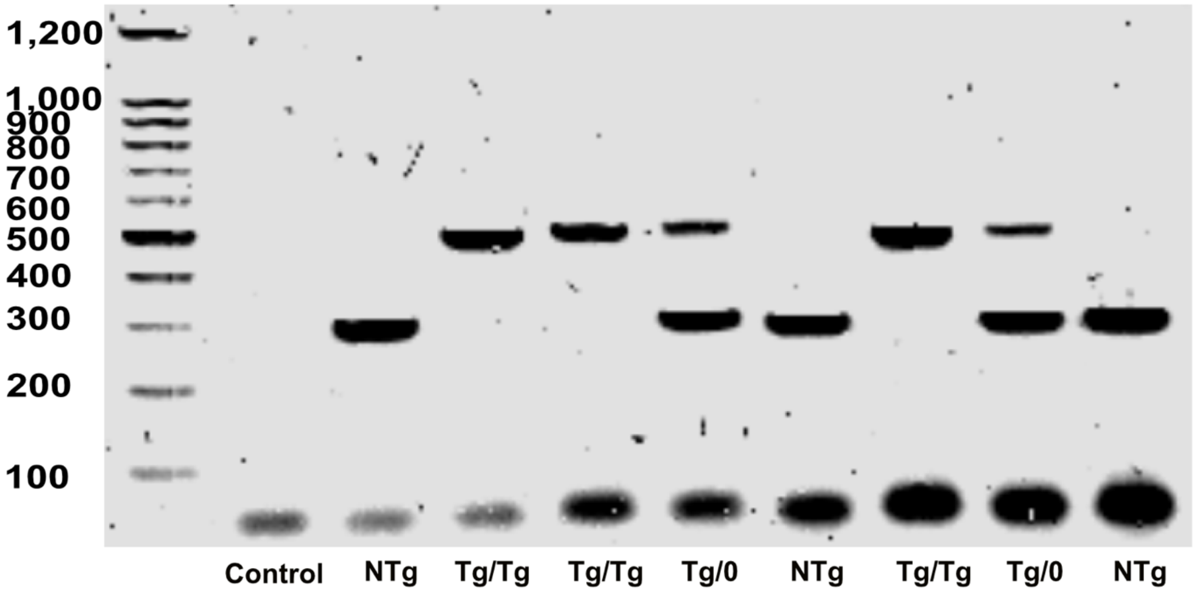

Figure 5: 1.5% agarose gel showing genotypes of hTDP43 mice. Bands below 100 base pairs are primer dimers, a by-product typically generated by PCRs, which do not affect the interpretation of relevant bands. The recorded heights for bands are as follows: 303bp for the TDP43 WT band and 500bp for the human transgenic TDP43 band.

Tissue Collection

To evaluate the involvement of selected pathways on disease pathology, mice were culled at either early symptomatic (P15), late symptomatic (P19), or at clinical end-stage (typically occurring around P22-23), determined by mice meeting criteria for a clinical score of 3 (Alhindi et al., 2023; Chaytow et al., 2022). Mice were humanely culled via an overdose of anesthetic with exsanguination to confirm death after reflexes were checked. The brain and spinal cord were then dissected out quickly to be either used for protein or RNA or histological purposes. The spinal cord was extracted using hydraulic extrusion (Richner et al., 2017).

Protein or RNA

Brains and spinal cords were dissected and flash-frozen using liquid nitrogen. These samples were then stored at -80°C until required for western blot quantification or quantitative PCR (qPCR) quantification.

Western Blot Preparation

Protein homogenisation

To quantify changes in protein levels, western blotting was utilised. To homogenise samples, 100µl of the homogenisation solution was added to SPC and 500µl was added to brain samples (Table 3). Samples were then homogenised using a plastic pestle and left at 4°C for 10 minutes (Eaton et al., 2013) (Table 3). Samples were then centrifuged at 4°C on full speed for 10 minutes. Afterwards, the supernatant containing the homogenised protein was taken. For SPC samples, 150µl of the supernatant was taken, while for brain samples, 500µl was taken. For brain samples, a 1 in 5 dilution was conducted using RIPA buffer. Samples were then left at -20°C until required.

BCA Assay

To quantify the amount of protein in each sample, a Bicinchoninic acid (BCA) assay (Protein Chemistry) was performed using a 96-well plate (Y. T. Huang et al., 2019). Triplicate protein standard wells using albumin were created with the concentrations of 0, 2, 4, 6, 8, 10, 20, and 40 µg, respectively. Duplicates of protein samples were created by pipetting 1µl of the sample in the corresponding wells. BCA reagent mixture was created according to the manufacturers' instructions (protein chemistry) with 200µl of the mixture added to each well (Table 3). The plate was then heated for 10 min at 60°C (Y. T. Huang et al., 2019). The optical density of the plate was determined by using the GloMax explorer plate reader (Promega), measuring the absorbance at 560 nm for each well (Figure 6A).

The absorbance quick read output was then analysed to create working 20µg samples to use during western blotting (Figure 6) (Y. T. Huang et al., 2019). Absorbance reading was determined for each well by subtracting the background absorbance (Figure 6B). The triplicate protein standard wells were then averaged and used to create a standard concentration curve, with an equation and R^2 value generated (Figure 6C). The R^2, measuring how accurate the line of best fit is to the data points, was then evaluated. As the graph was generated using standard concentrations, there should be a linear relationship between the optical density and protein concentration. Therefore, if the R^2 value was lower than 0.98, results were deemed unreliable due to pipetting error.

If the R^2 value was 0.98 or greater, the accuracy of the results was sufficient to calculate sample protein concentrations (Y. T. Huang et al., 2019). To calculate protein concentration for the sample, the duplicate protein wells were averaged and then divided by the slope (Figure 6D). 100 was then divided by the calculated protein concentration to generate 20µg working solutions. 12.50µl of 4x B Mercaptoethanol and ddH20 were then added to each sample solution to make 50µl.

Samples were then heated at 70°C for 10 minutes to enable protein denaturation before being stored at -20°C until needed.

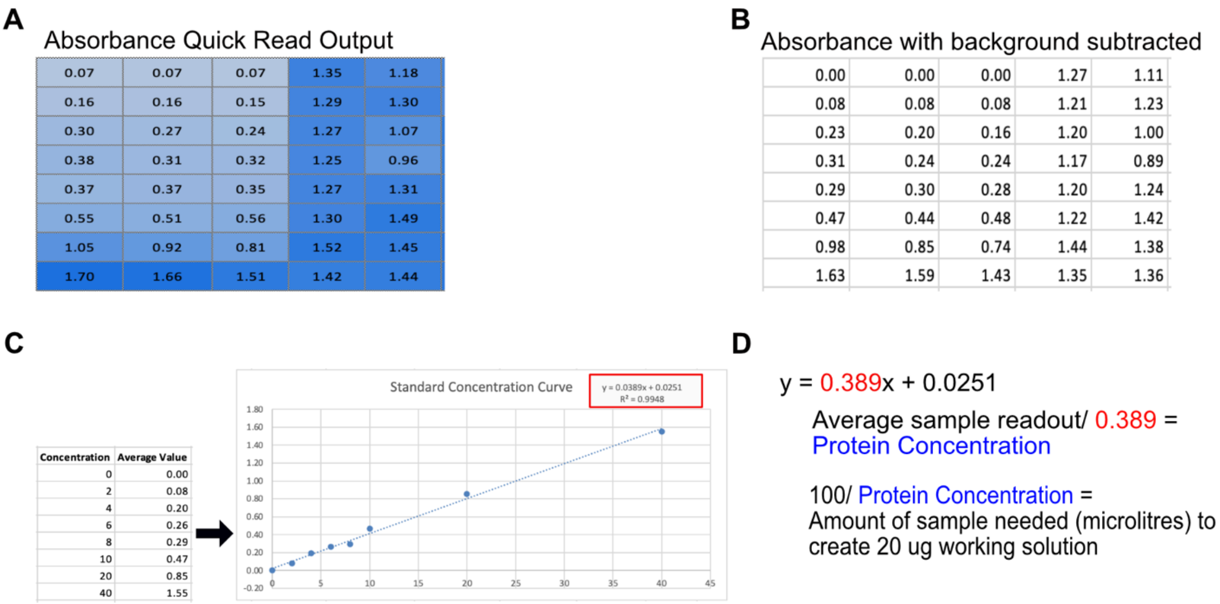

Absorbance Quick Read Output

0.07	0.07	0.07	1.35	1.18
0.16	0.16	0.15	1.29	1.30
0.30	0.27	0.24	1.27	1.07
0.38	0.31	0.32	1.25	0.96
0.37	0.37	0.35	1.27	1.31
0.55	0.51	0.56	1.30	1.49
1.05	0.92	0.81	1.52	1.45
1.70	1.66	1.51	1.42	1.44

Absorbance with background subtracted

0.00	0.00	0.00	1.27	1.11
0.08	0.08	0.08	1.21	1.23
0.23	0.20	0.16	1.20	1.00
0.31	0.24	0.24	1.17	0.89
0.29	0.30	0.28	1.20	1.24
0.47	0.44	0.48	1.22	1.42
0.98	0.85	0.74	1.44	1.38
1.63	1.59	1.43	1.35	1.36

Concentration	Average Value
0	0.00
2	0.08
4	0.20
6	0.26
8	0.29
10	0.47
20	0.85
40	1.55

y = 0.389x + 0.0251

Average sample readout/ 0.389 = Protein Concentration

100/ Protein Concentration = Amount of sample needed (microlitres) to create 20 ug working solution

Figure 6: Protocol used to quantify BCA assays. A. Representative Quick Read Output produced by the GloMax explorer plate reader B. Representative absorbance reading with background noise subtracted. C. Representative standard concentration curve generated using triplicate protein standard wells. D. Concentration of protein samples were determined. The duplicate sample wells were averaged. The average sample optical density was divided by the slope (red value) to get the protein concentration. 100 was then divided the protein concentration to generate 50µl 20µg sample solutions.

Western Blotting

To quantify changes in protein levels of select autophagy and SG genes, western blotting was performed on Tg/Tg and NTg littermates at different time points (Y. T. Huang et al., 2019). 20µg of each sample and 2.5µl of the chameleon ladder, used to determine the size of proteins detected, were loaded into a protein gel (Table 3). The gel was then run at 80V for 10 minutes, followed by 150V for 50 minutes. Afterward, the products on the gel were transferred to a membrane using the iBlot 2 transfer machine (Invitrogen) (Y. T. Huang et al., 2019). The membrane was then quickly washed with ddh20 before being placed on a rocker at speed 65. The ddh20 was then discarded, and 10ml of revert total stain 520 (TPS) was added to each membrane for 5 minutes. Membranes were then washed twice with 12 ml of total wash (Table 3) and then finally a ddh20 wash. Membranes were kept in ddh20 to avoid drying out. Membranes were then imaged using the Licor Odyssey M machine to visualise the total amount of protein in each well. This will serve as a reliable normalisation measure for quantification (Eaton et al., 2013; Y. T. Huang et al., 2019; Kirshner & Gibbs, 2018). The membrane was then blocked for 30 minutes using 5% milk with 0.2% TBST on a roller (Table 3). For TiaR antibody staining, blocking with 5% milk with 0.1% TBST was utilised. Primary antibodies were then applied with 5% milk with 0.2% TBST overnight at 4° C on a roller (Table 1, 3). TaiR antibody was applied with 5% milk with 0.1% TBST overnight at 4°C on a roller. (Table 1, 3).

The primary antibody solution was then poured off and kept at -20°C for reuse. The membrane was then washed three times with 0.2% TBST for 10 minutes at room temperature (RT). For TiaR membranes, membranes were washed three times with 0.1% TBST for 10 minutes at RT. Afterwards secondary antibody was applied with 5% milk and 0.2% TBST for 1 hour (Table 1. 3). TiaR secondary antibody was applied with 5% milk with 0.1% TBST for 2 and a half hours (Table 1, 3). The secondary antibody solution was poured off, and TBS was then added to the membrane and shaken vigorously for 5 seconds. The membrane was then washed with TBS three times for 30 minutes each. The membrane was dried and imaged using the Licor Odyssey M machine, selecting the 700 and 800 nm channels with an offset of 1.

Quantification

To quantify the signal of the protein of interest, images were imported into Image Studio Lite (Y. T. Huang et al., 2019). TPS images were quantified by drawing rectangles of the exact same size and shape around each lane, avoiding any dark or light spots (Y. T. Huang et al., 2019) (Figure 7A). Under analysis, median and top/bottom segmentation was selected, and the table generated under shapes was copied into excel (Figure 7C). To quantify the protein of interest, rectangles were drawn around the protein-specific band (Y. T. Huang et al., 2019) (Figure 7B), and results were copied into excel (Figure 7C). To normalise signal between different animals, the TPS channels were first normalised to the highest TPS signal present on the membrane (Y. T. Huang et al., 2019). The sample antigen-specific signal was normalised to its TPS signal and then to the average NTg signal for that membrane (Y. T. Huang et al., 2019) (Figure 7C). The normalised protein signal was then used to determine whether there were differences in protein expression levels between genotypes (Figure 7D).

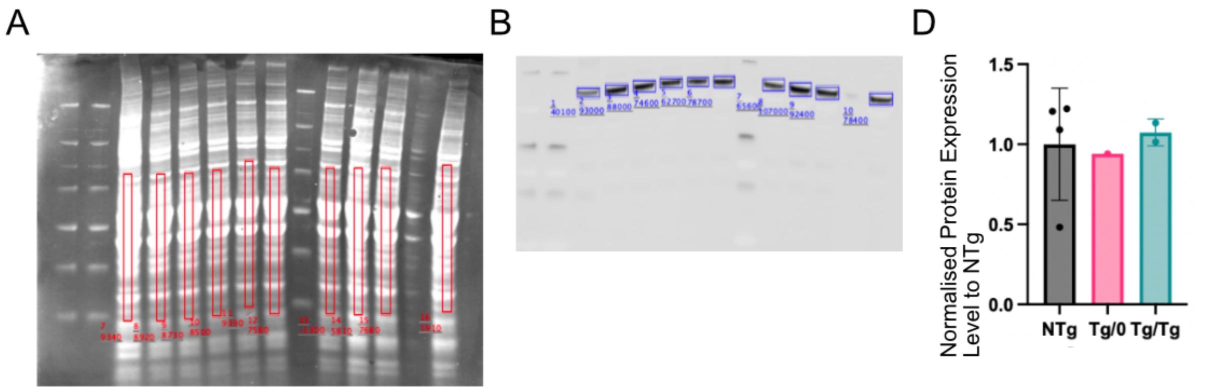

C

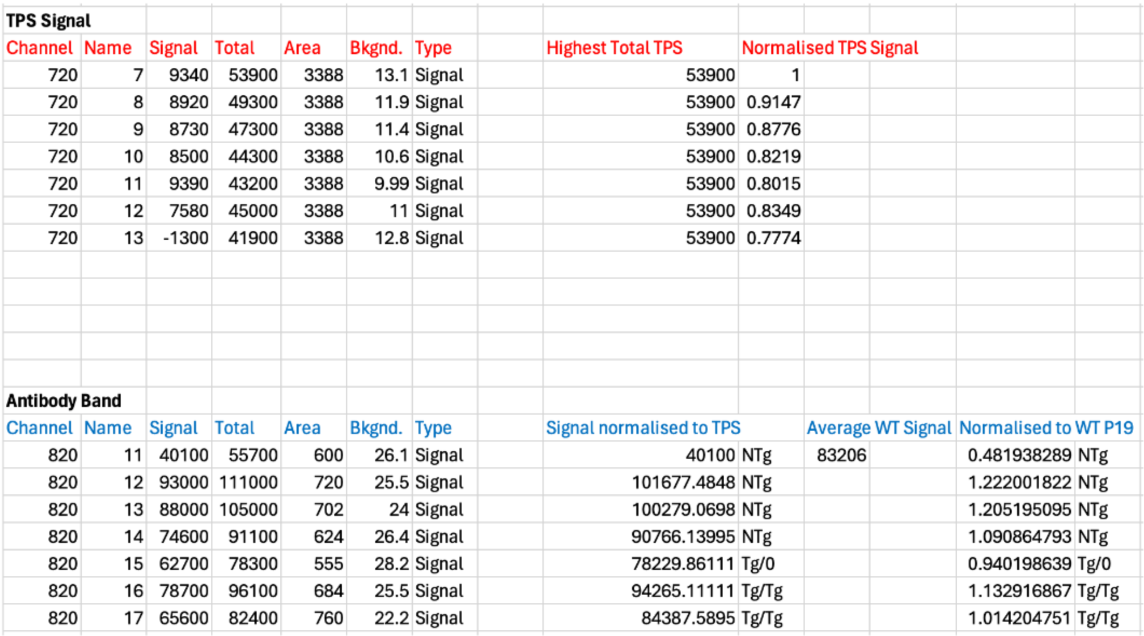

TPS Signal

Channel	Name	Signal	Total	Area	Bkgnd.	Type		Highest Total TPS	Normalised TPS Signal
720	7	9340	53900	3388	13.1	Signal		53900	1
720	8	8920	49300	3388	11.9	Signal		53900	0.9147
720	9	8730	47300	3388	11.4	Signal		53900	0.8776
720	10	8500	44300	3388	10.6	Signal		53900	0.8219
720	11	9390	43200	3388	9.99	Signal		53900	0.8015
720	12	7580	45000	3388	11	Signal		53900	0.8349
720	13	-1300	41900	3388	12.8	Signal		53900	0.7774

Antibody Band

Channel	Name	Signal	Total	Area	Bkgnd.	Type		Signal normalised to TPS		Average WT Signal	Normalised to WT P19	
820	11	40100	55700	600	26.1	Signal		40100	NTg	83206	0.481938289	NTg
820	12	93000	111000	720	25.5	Signal		101677.4848	NTg		1.222001822	NTg
820	13	88000	105000	702	24	Signal		100279.0698	NTg		1.205195095	NTg
820	14	74600	91100	624	26.4	Signal		90766.13995	NTg		1.090864793	NTg
820	15	62700	78300	555	28.2	Signal		78229.86111	Tg/0		0.940198639	Tg/0
820	16	78700	96100	684	25.5	Signal		94265.11111	Tg/Tg		1.132916867	Tg/Tg
820	17	65600	82400	760	22.2	Signal		84387.5895	Tg/Tg		1.014204751	Tg/Tg

Figure 7: Quantification of Antibody-Specific Bands. The above-mentioned protocol was used to quantify results. A. Representative western blot showing TPS quantification, quantified using rectangles of the exact same shape and size (red) in each lane. B. Representative western blot showing quantification of antigen-specific band. C. Results from A and B were then pasted into an Excel, and data was normalized to TPS signal and to NTg signal. D. Representative bar chart showing the difference in protein expression between genotypes.

Antibodies

Primary and secondary antibodies were utilised for western blotting and/or immunohistochemistry (Table 1).

Table 1

Antibody	Supplier	Catalog	Species	Concentration
Beclin	Cell Signalling Technology	3495S	Rabbit	1:1000 (WB)
ChAT	Millipore	AB144P	Goat	1:200 (IHC)
DAPI stain	Invitrogen	D1306	NA	1:1000 (IHC)
Donkey anti Goat 594	AlexaFluor	A11058	Donkey	1:500 (IHC)
Donkey anti goat 647	Life Technologies	A21447	Donkey	1:500 (IHC)
Donkey anti Rabbit 488	AlexaFluor	A21206	Donkey	1:500 (IHC)
Donley anti Mouse 488	AlexaFluor	A21202	Donkey	1:500 (IHC)
G3BP1	DSHB	PCRP-G3BP1-2HB	Mouse	1:50 (IHC) 1:100(WB)
G3BP2	DSHB	PCRP-G3BP2-1C7	Mouse	1:50 (IHC) 1:100 (WB)
LC3B	Abcam	Ab192890	Rabbit	1:2000 (WB)
Neurotrace 500/525	Life Technologies LTD (Invitrogen Division)	N21480	-	1:50 (WB)
P62	Abcam	Ab56416	Mouse	1:1000 (WB)
TDP43	Proteintech	10782-2-AP	Rabbit	1:100 (IHC)

TiaR	BD Transduction labs	610352	Mouse	1:100 (WB)
ULK1	Cell Signalling Technology	8054S	Rabbit	1:500 (WB)

Table 1: Primary and secondary antibodies utilised for Immunohistochemistry and Western Blotting. Table lists the antibody target, supplier, catalog number, species the antibody was raised in, and the concentration antibody was used for either immunohistochemistry (IHC) and Western Blotting (WB).

Histology

After dissection, SPCs were pinned straight and were fixed along with brain tissue using 4% PFA for 24 hours and then emersed in 30% sucrose for 24 hours at 4°C (Table 3). Samples were then immersed in a 1:1 OCT/Sucrose mixture on a roller for 1 hour at 4°C. The cervical and thoracic regions of the SPC were then removed before the SPCs were embedded into blocks using 1:1 OCT/Sucrose mixture at 4°C (Chaytow et al., 2022; Dong et al., 2021). SPC were embedded with the lumbar region facing down and the SPC lying vertically in the block. Brain samples were embedded sagittally. Blocks were then stored at -80°C.

SPC blocks were then cryosectioned using the cryostat CM3050 S (Leica), generating 20 μm thick sections. As MN have an average size of 50 μm (Bukreeva et al., 2017), SPC were mounted in sequential order over 6 slides, with sections being mounted in the same position on each slide before moving onto the next position (i.e., the first 6 SPCs collected were mounted in the top left of each slide). This means that the distance between each SPC section on each slide was 120 μm, mitigating any potential issues of double counting the same MN population within one slide. This process was repeated until 10 sections were mounted on all slides. Slides were left at room temperature overnight to dry before being stored at -20°C until required.

Immunohistochemistry

Immunohistochemistry was performed on cryosectioned SPC slides to determine the distribution of proteins within the SPC of NTg and Tg/Tg mice.

To evaluate SG formation, SG formation with terazosin treatment and inflammation, slides were washed with ddH20 on a shaker for 5 minutes at speed 45. Slides then underwent antigen retrieval consisting of mixing citric acid, HCl, and ddh20 and heated on medium heat for 15 minutes (Table 3). Slides were then left to cool in the antigen retrieval solution at RT for 45 minutes.

The slides were then washed using PBS twice for 5 minutes. Permeabilization was then performed to allow intracellular access for primary antibody access using PBS with 0.3% triton (Table 3). Slides were permeabilised with this solution thrice for 10 minutes. A hydrophobic pen was then used to outline samples to prevent agent loss. Slides were then blocked with 10% or 5% donkey serum with 0.3% triton for an hour and 30 minutes at RT to block non-specific primary antibody binding (Table 3). Afterward, primary antibodies and PBS with 0.1% triton were applied at relevant concentrations (Table 1, 3) and left on overnight at 4°C.

Slides were then washed three times for 10 minutes. The slides were then washed for 5 minutes with PBS with 0.1% triton on a shaker at RT (Table 3). Secondary antibodies diluted in PBS were then applied to slides for 1 hour (Table 1). Slides were then washed using PBS four times for 10 minutes each.

For evaluating inflammation, slides underwent an additional step. Neurotrace stain was applied for 45 minutes, followed by three 10 minute PBS washes.

To evaluate SG and TDP43 co-localisation, slides underwent antigen retrieval as described previously. They were then washed with PBS twice for five minutes. A hydrophobic pen was then used, and slides underwent blocking using 3% BSA with 0.2% triton for 1 hour. Afterward, primary antibodies and BSA with 0.2% triton were applied at the relevant concentrations and left overnight at 4C (Table 1, 3).

Slides were then washed three times for 10 minutes. Secondary antibodies diluted in PBS were then applied to slides for 1 hour (Table 1). Slides were then washed using PBS four times for 10 minutes each. Neurotrace stain was applied for 45 minutes, followed by three 10 minute PBS washes (Table 1).

For all slides, DAPI was then applied for 10 minutes. Slides were washed for 5 minutes followed by 10 minutes with PBS and mounted using mowiol.

Microscopy

Slides were imaged using the Lecia Thunder Epifluorescent Microscope at the ventral horn of the SPC (area in which MN populations are) at 20x magnification. The ventral horn was identified using ChAT or Neurotrace channels (Figure 8). Each SPC was only imaged once. A minimum of 8 SPC were imaged per slide to analyse SG formation. A minimum of 6 SPC per slide were imaged to analyse inflammation. Per SPC, three images were taken on the DAPI channel (blue, 405 nm excitation), G3BP2 or Neurotrace channel (green, 488nm excitation), and ChAT or Iba1 channel (red, 594 nm excitation). Microscope settings were consistent across all images with a consistent area taken (443023.36μm^2). Channels were taken in sequential order to avoid bleed-through of channels.

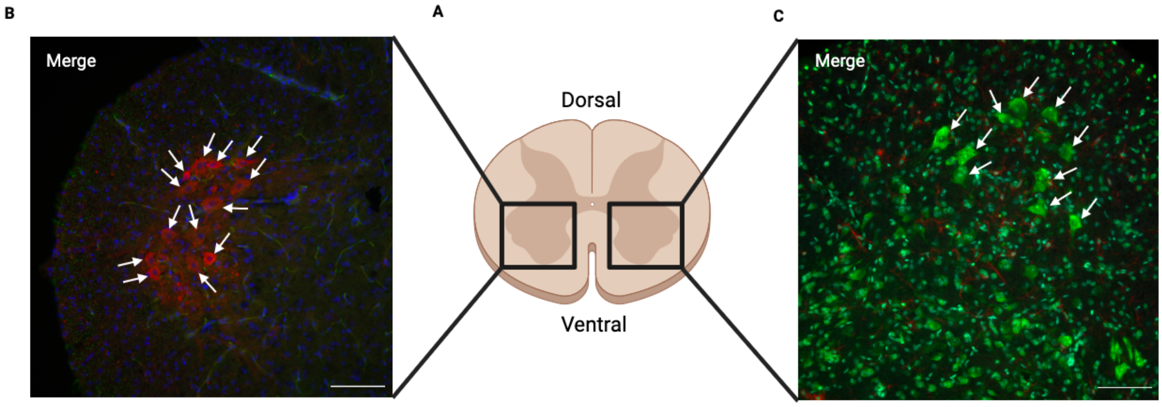

Figure 8: Identification of the ventral horn using Neurotrace stain or ChAT antibody. A. schematic of an unstained SPC section with the ventral horn circled. To identify the ventral horn after IHC, the ChAT (B) or neurotrace channels (C) were utilised. Both are established markers for motor neurons. Motor neurons are marked by white arrows and were used to establish that each image was taken in the ventral horn. Scale bar = 100μm

Representative images for SG formation, SG and TDP43 colocalisation, and SG formation following terazosin treatment were then taken using the Confocal Nikon A1R on 20x and 60x magnification using the DAPI channel (402 nm excitation), EGFP channel (488 nm excitation), mCherry (562 nm excitation), and far red (658nm excitation) using consistent intensity settings and a consistent area taken (67024 μm^2 for 20x images, 37535.19 μm^2 for 60x images). Channels were taken in sequential order to avoid bleed-through of channels.

Quantification

Analysis was conducted using Fiji Software. For each SPC image, the DAPI, Neurotrace/G3BP2, and ChAT/Iba1 channels were merged and then blinded using the 'Blind Analysis Tool' plugin in Fiji for quantification. The merged images were then split for analysis using Fiji analysis software.

For SG formation and SG formation following terazosin treatment analysis, motor neuron counts were first performed by counting ChAT-positive cells using the cell counter plugin (Alhindi et al., 2023; Du et al., 2015; McLeod et al., 2022). The ChAT-positive cells were then counted for positive G3BP2 staining (Figure 9) and recorded. A ratio was then taken of the positive G3BP2 cells to the total motor neuron count for each image. These values were then averaged to avoid pseudo-replication per mouse and plotted.

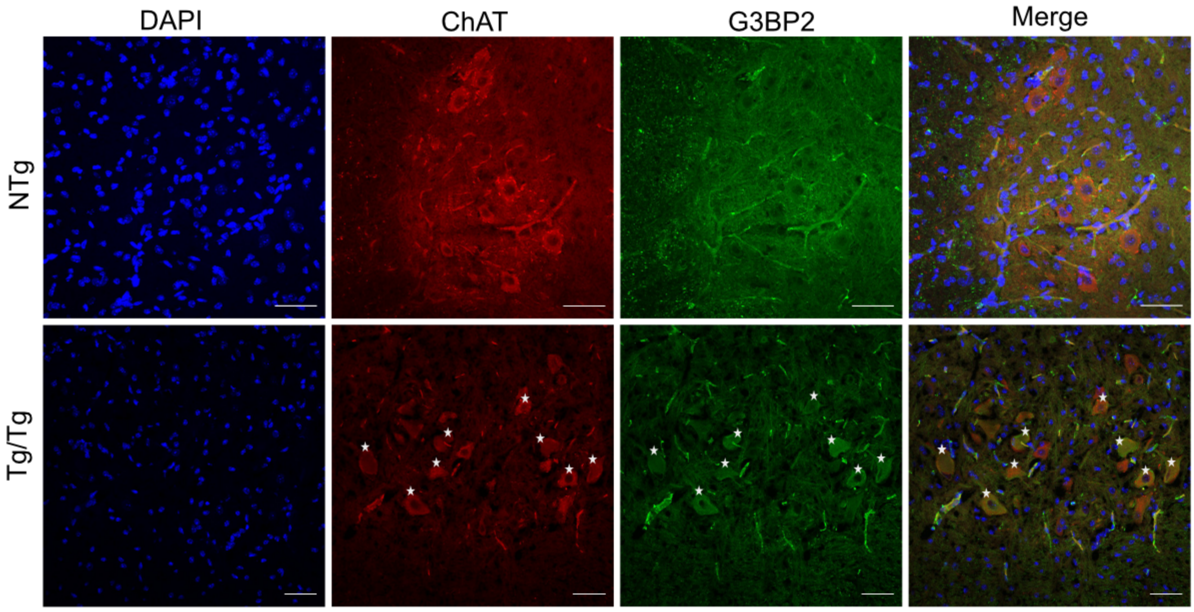

Figure 9: Representative Images showing G3BP2 Motor Neuron Positive Counting. White stars indicate G3BP2-positive ChAT cells. Scale bar = 50 µm.

Two methods were utilised to determine inflammation activation in late symptomatic SPCs. Using the Fiji analysis ‘Blind Analysis Tool’ plugin, images were first blinded. Microglia cell counts were then performed in NTg and Tg/Tg P19 SPCs. The neurotrace channel was false colored to ‘grays’ to better distinguish between the white and grey matter of the SPC (Figure 10B). A region of interest (ROI) was then drawn around the grey matter and stored in the ROI manager (Figure 10C). Manual thresholding was then performed on the Iba1 channel using a duplicate image false-colored with the Inferno Fiji color editor for morphological comparison (Figure 10 D, E). Auto-thresholding was attempted for the Iba1 channel to reduce bias; however options did not produce a consistent result over all SPC images (Figure 11).

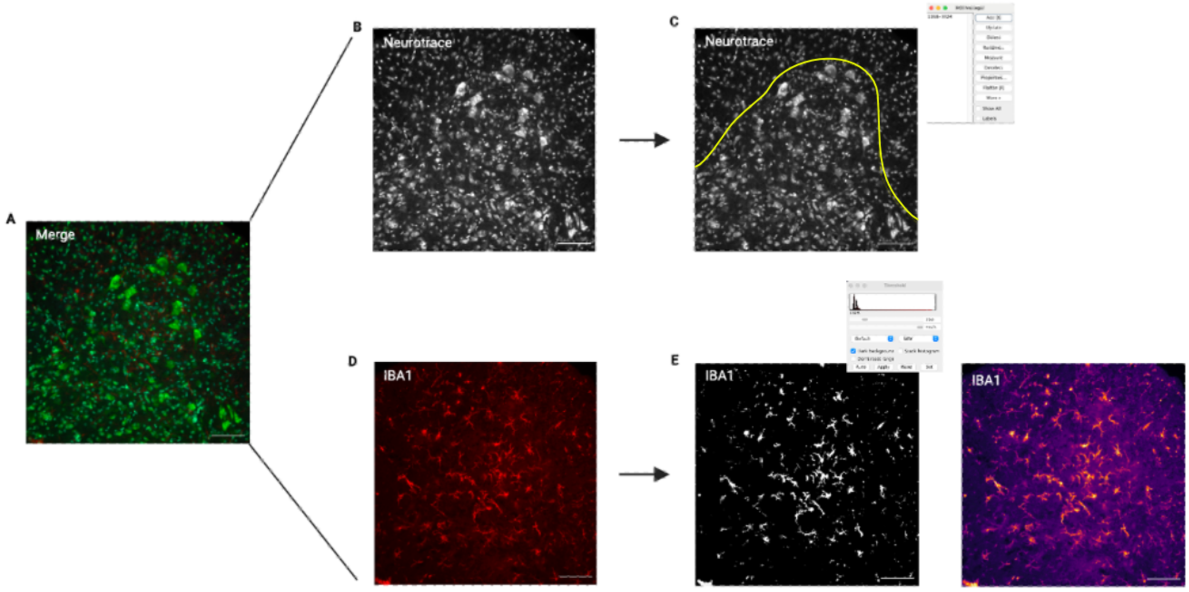

Figure 10: Workflow of inflammation analysis. First, the merged image (A) was split into individual channels. The neurotrace channel was then false-colored ‘grays’ (B), and a region of interest (ROI) was drawn around the grey matter of the SPC (yellow line) (C). The ROI was saved in the ROI manager. Then, the Iba1 channel was opened (D) and manually thresholded using a duplicate Iba1 channel false-colored with inferno (purple) for comparison (E). Scale bar = 100µm

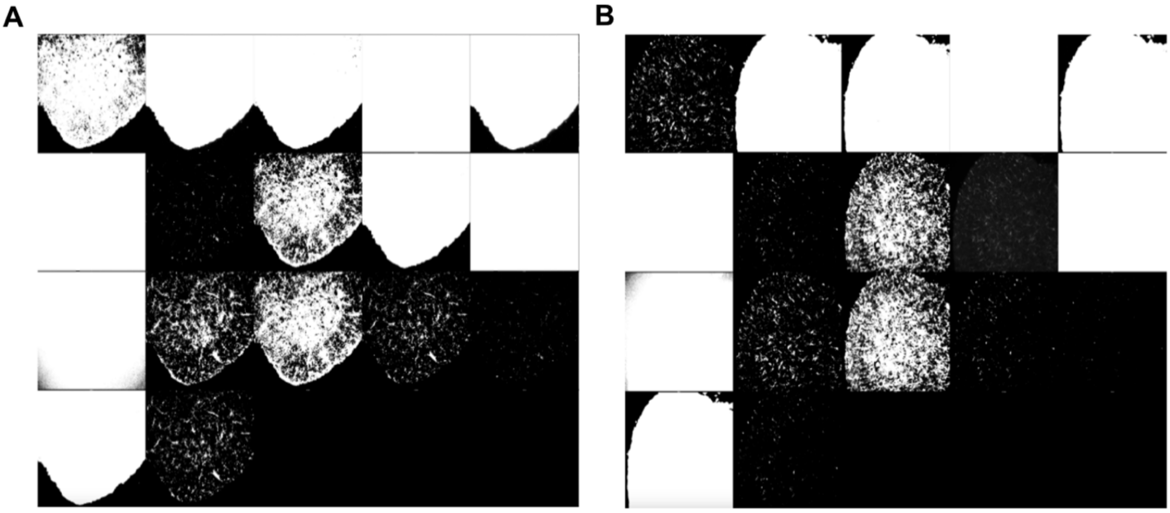

Figure 11: Representative Images of auto thresholding. To establish a method for thresholding, two NTg and Tg/Tg SPCs were blinded and thresholded using the auto-threshold function in Fiji. A and B represent two different SPCs from different mice. Across all mice, no single threshold produced a quantifiable result; therefore, manual thresholding was utilised.

The thresholded Iba1 channel (Figure 10E) was then merged with the DAPI channel. The Iba1 channel was then false-colored to magenta, with the DAPI channel false-colored to cyan (Figure 12A). The ROI outlining the grey matter of each SPC was overlayed. Microglia were defined as white overlaps between magenta (Iba1) and cyan (DAPI) (Figure 12A). Iba1 cells were counted using the 'Cell Counter' Plugin in the grey matter with an Iba1 channel duplicate image false-colored with inferno to act as a morphological reference. Next, the overall area of the grey matter of each SPC was taken to act as a normalisation measure for both microglia counts and particle area quantification (Figure 13C). Iba1+ cell counts were then normalised to the overall grey matter area. These values were then averaged per mouse to avoid pseudo-replication.

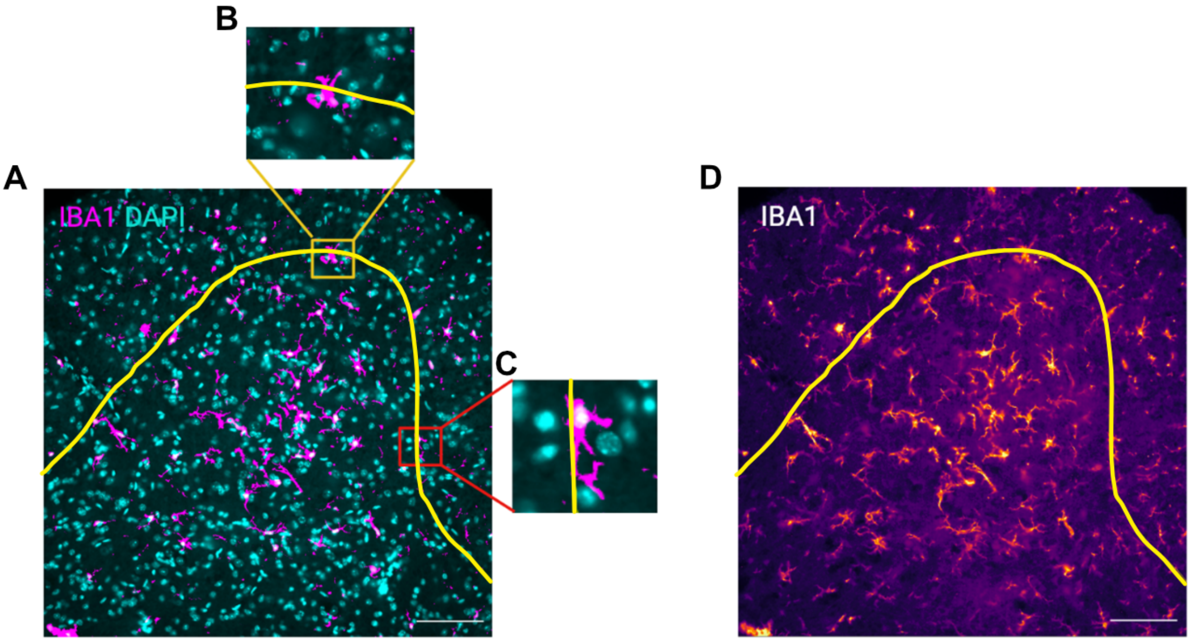

Figure 12: Quantification of inflammation in late symptomatic spinal cords. To quantify inflammation, microglia were labeled with Iba1, and cell nuclei were labeled with DAPI. Using the ROI manager, a line circling the grey matter of the spinal cord was inserted (yellow line). Microglia were defined as white overlaps between magenta (Iba1) and cyan (DAPI) (A). To confirm microglia morphology a duplicate Iba1 image false-colored inferno was used during counting (D). For microglia that were on the border of the ROI, if their cell bodies were within the ROI, they were counted (B), while if their cell bodies were outside, they were not counted (C). Scale bar = 100 µm.

Next, to calculate the area of Iba1+ staining in the grey matter of each spinal cord, the Fiji particle area quantification was performed. The ROI outlining the grey matter of each SPC was overlayed on the thresholded Iba1 channel for each SPC (Figure 13A). The particle area of Iba1 staining was then determined for the grey matter and copied into an Excel file (Figure 13B). To normalise the particle area for each SPC, the overall area of the grey matter was also measured for each SPC through using the Fiji measure function (Figure 13C). The Iba1+ particle area was then averaged to the overall area for each SPC. Values were then averaged per mouse to avoid pseudo-replication and plotted.

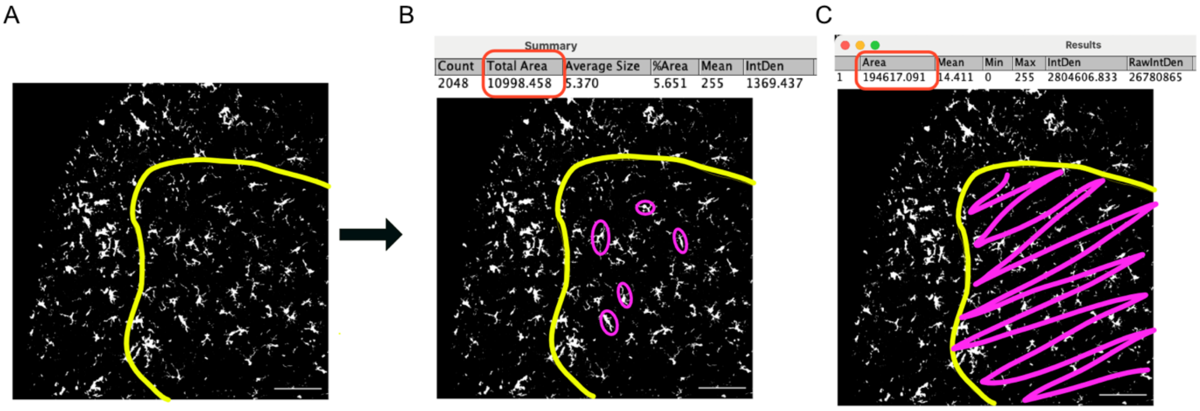

Summary

Count	Total Area	Average Size	%Area	Mean	IntDen
2048	10998.458	5.370	5.651	255	1369.437

Results

	Area	Mean	Min	Max	IntDen	RawIntDen
1	194617.091	14.411	0	255	2804606.833	26780865

Figure 13: Quantification for Iba1+ Particle Area in late symptomatic spinal cords. A. Representative thresholded Iba1 channel with line overlayed outlining the grey matter (yellow line). B. Representative thresholded Iba1 channel showing particle area quantification. The Fiji particle area quantification calculated the area that the particles take up in the grey matter. Representative particles are outlined with purple circles. The total area (red circle) was then recorded as the output. C. Representative thresholded Iba1 channel showing total area quantification. Using the FIJI measure function, the total area of the grey matter was determined (shown by the purple shaded area). The area (red circle) was then recorded as the output. Scale bar = 100 µm.

RNA Extraction

To evaluate changes in DNA expression levels of selected targets, quantitative PCR (qPCR) was utilized. To perform qPCR, RNA was first extracted from Tg/Tg and NTg late symptomatic SPC and then converted into cDNA. Next, primer pairs were optimised for their detection of select targets (Figure 14)

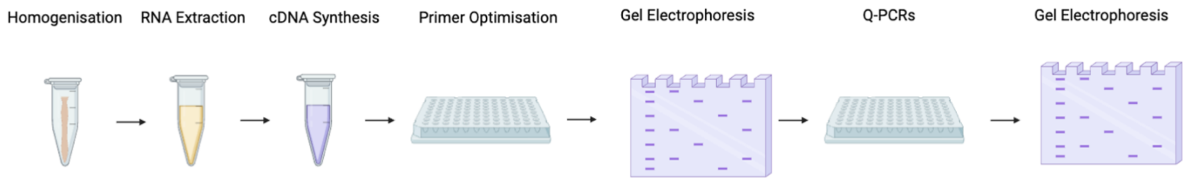

Figure 14: General Workflow for RNA work. SPC were first homogenised before RNA extraction was then performed. Afterward, cDNA synthesis was performed, followed by primer optimisation. Primer pairs were then selected based on their CQ time (amplification curve) and melt curve and checked for product specificity using gel electrophoresis. qPCRs were then performed to determine changes in transcription between Tg/Tg and NTg mice. Prior to analysis, the NTC and one sample well were then run on a gel to check for contamination. Afterward, analysis of results proceeded.

RNA extraction was extracted from spinal cords using the Quick-start Protocol from Qiagen using the RNeasy Plus Mini Kit (Qiagen) (Table 3). All reagents were kept at 4°C during extraction. First, 10µl of B-mercaptoethanol was added to 1 ml Buffer RLT Plus. 600µl of this solution was added to each SPC and homogenised using a plastic homogeniser. The homogenized tissue was then centrifuged for 3 minutes at maximum speed before being transferred to a gDNA eliminator spin column placed in a 2ml collection tube. The sample was then centrifuged for 30 seconds at 8000g. The column was then discarded while the flow-through was saved. 600µl of 70% ethanol was then added to each sample and mixed by pipetting. 700µl of the sample was then transferred to an RNeasy spin column, placed in a 2ml collection tube, and centrifuged for 15 seconds at 8000g. The flow-through was then discarded, and 700µl of RW1 was added to the RNeasy spin column. A new 2ml collection tube was added to the outside of the spin column, and the sample was centrifuged at 8000g for 15 seconds. The flow-through was again discarded, and 500µl of Buffer RPE was added to the RNeasy column. A new flow-through collection tube was added to the outside of the spin column, and then the sample was centrifuged at 8000g for 15 seconds. The flow-through was then discarded again, and 500µl of Buffer RPE was added to the RNeasy spin column. The flow-through was replaced, and then the sample was centrifuged at 8000g for 2 minutes. The flow-through was discarded, and 50µl of RNase-free water was added to the spin column. To elute the RNA, a new flow-through was added, and then the sample was centrifuged at 8000g for 1 minute. Centrifuge the sample again for 1 min at 8000g to further elute the RNA. The collection tube was then kept, and the RNeasy column was discarded.

Immediately after RNA extraction, the concentration of RNA in each sample was determined using the Nanodrop 2000 spectrophotometer (Thermo Scientific). RNA concentration for each sample was determined using 1.5µl of each sample. The concentration, A_{260}/A_{280} ratio, and A_{260}/A_{230} ratio were analysed. Expected ranges for the A260/A280 ratio are 1.8-2.0 and the A_{260}/A_{230} ratio 2.0-2.2 (Thermo Fischer Scientific T042 technical bulletin). Significant deviations from these ranges indicate the presence of contaminates; therefore, samples that significantly deviated were excluded. cDNA synthesis immediately proceeded with RNA extraction.

cDNA synthesis

qPCR measures the DNA generation over multiple cycles. Converting the extracted RNA into Complementary DNA (cDNA) is necessary, as we utilise DNA polymerase which recognises DNA instead of RNA. The generation of mRNA was necessary as when converting RNA to cDNA; the cDNA will therefore not contain any introns, which interrupts the sequence of the gene. Therefore, the extracted RNA was then used as a template to synthesise cDNA using the Maxima Strand Kit (Life Technologies) (Table 3). 450µg sample solutions were created by combining the RNA extracted sample, DEPC-H20, 1 µl of DNAse, and 1 µl of DNase buffer. A reaction mix was then created by combining 4 µl of reaction mix, 2 µl of maxime enzyme mix, and 4 µl of DECP-free H20 (Table 3). This was added to the sample solution, and the solution was vortexed. The samples were then placed in the T100 Thermal Cycler machine (BioRad) following the listed protocol:

1. 25°C 10 min
2. 50°C 15 minutes
3. 85°C 5 minutes

Afterward, samples were placed at -20°C for short-term storage.

Real-Time Quantitative PCR (qPCR) Optimisation

Primer pairs were sourced or designed to target aspects of the NRF2 pathway and components of SGs (Table 2). Using the same NTg sample for all genes, primer pairs were optimised for their effectiveness using 96-well plates. Stock Primer pair solutions and Sample solutions were created (Table 3). 10.8μl of the primer pair solution and 9.2μl of the sample solution were then added to each well. Primer pairs were then analysed on a temperature gradient spanning from 50-63°C using the CFX Opus Deepwell Real-Time PCR system (BioRad) following the listed protocol:

1. 50°C 2 min
2. 95°C 2 min
3. 95°C 15 sec
4. 58/63°C 30 sec

   Plate Read

5. Go to 3 39X
6. 65 – 95°C 5 sec

   +0.5°C /cycle

To determine the efficiency of each primer pair measures of fluorescent intensities were analysed. The amplification curve was analysed to determine if a consistent amplification was produced over the temperature gradient, evident by a tight curve (Figure 15A). Next, the melt curve was observed to determine if they displayed a single peak with no shouldering. Shouldering would indicate an aspecific product (Figure 15B).

For final determination of the specificity of the primer pair, the 60°C NTg sample for each primer pair was ran on a 1.5% agarose gel to confirm no aspecific products were targeted. The 60°C well was chosen as this temperature is used in the qPCR protocol during plate reading. The expected molecular weight was compared to the band elucidated to confirm primer specificity.

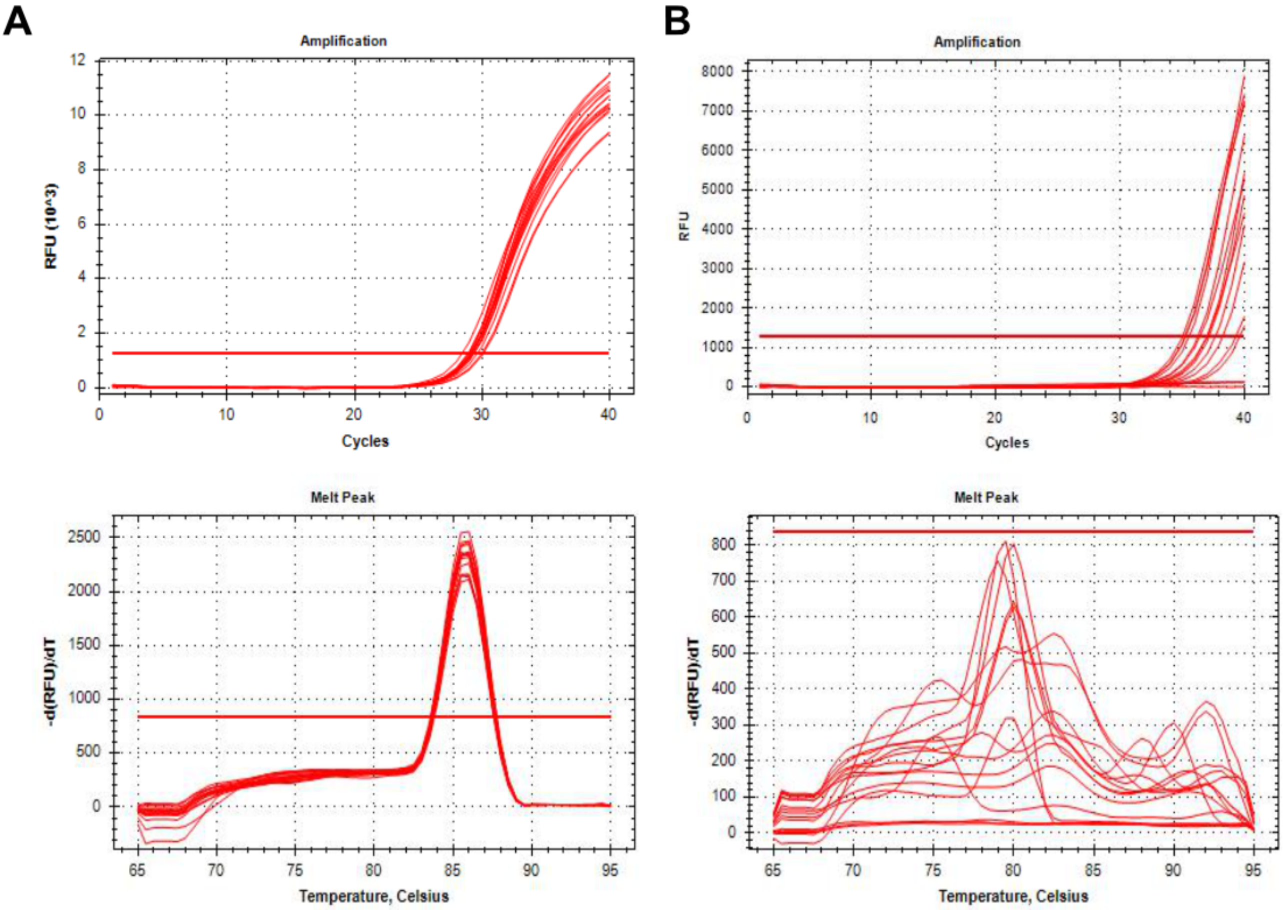

Figure 15: Amplification and Melt Peak Quantification. A. Representative amplification and melt peak of a specific primer. The amplification curve (top graph) is tight over the temperature gradient. The melt peak (bottom graph) displays a singular peak. B. Representative amplification and melt peak for non-specific primer. The amplification curve (top graph) shows variation between temperatures. The melt peak (bottom graph) does not show a consistent, singular peak.

Quantitative PCR (qPCR)

With the selected primer pairs, we analyzed the difference in SG formation and Oxidative stress-linked genes between Tg/Tg and NTg in P19 SPC. Samples were analysed using triplicates to confer greater reliability in the data. Stock primer pair solutions for each gene target were created by combining the forward and reverse primer with the master mix, and 10.8µl was pipetted into the appropriate wells (Table 1, 3). Next, stock sample solutions were created by combining cDNA with DEPC-free water, and 9.2µl was pipetted into the appropriate wells. Two controls were utilised per plate and primer pair: GAPDH (a household control gene) and a non-template control (NTC). The 96-well plate was then imaged using the CFX Opus Deepwell Real-Time PCR system (BioRad). The following protocol was used for qPCR testing:

1. 50°C 2:00 min
2. 95°C 2:00 min
3. 95°C 15 sec
4. 60°C 30 sec

   Plate Read

5. Go to 3 39X
6. 65 – 95°C 5 sec

   + 0.5°C /cycle

The NTC and a sample well for each gene was then run on a 1.5% agarose gel to confirm no contamination and that only a single product was produced during the qPCR.

Quantification

Results were analysed using BioRad Software. The CT values for triplicate wells were analysed. If the CT value differed in a triplicate well by ± 1 from the average, that well was excluded. The Delta CT value for all wells were then calculated by subtracting the control gene (GAPDH) by the target genes to normalise the samples. The average of all triplicates was then taken as the readout for each sample. The average of all NTg samples was then determined and used to normalise Tg/Tg samples to NTgs. Each value was then raised to the power of 2 to calculate fold change, and sample values were normalised to the average NTg fold change.

Table 2

Target	Name	Forward 3' to 5' Sequence	Reverse 5' to 3' Sequence	Band Size (bp)	Source
NrF2	NRF2 Primer 1	TTCTTTCAGCAGCATCCTCTCCAC	ACAGCCTTCAATAGTCCCGTCCAG	199	(Vargas et al., 2008)
	NRF2 Primer 2	AGCGACAGAAGGACTATGAGC	ATCCAGGGCAAGCGACTCA	297	Designed
HMOX1	HMOX1 Primer 1	CAAGCCGAGAATGCTGAGTTCATG	GCAAGGGATGATTTCCTGCCAG	243	(Vargas et al., 2008)
	HMOX1 Primer 2	TGCTAGCCTGGTGCAAGATAC	GGTGAGGGAACTGTGTCAGG	332	Designed
CytC	CytC Primer 1	CACGCTTTACCCTTCGTTCT	CTCATTTCCCTGCCATTCTCTA	105	(Safdar et al., 2009)
	CytC Primer 2	CACCGACACCGGTACATAGG	TCTCCCCAGGTGATGCCTTT	296	Designed
NQO1	NQO1 Primer 1	GCGAGAAGAGCCCTGATTGTACTG	TCTCAAACCAGCCTTTCAGAATGG	349	(Vargas et al., 2008)
	NQO1 Primer 2	TTCTCTGGCCGATTCAGAGTG	CCCACAGAGAGGCCAAACTT	268	Designed
GCLM	GCLM Primer 1	GCCACCAGATTTGACTGCCTTTG	TGCTCTTCACGATGACCGAGTACC	182	(Vargas et al., 2008)
	GCLM Primer 2	ACGAAGCACTTTCTCGGGTG	AACATCTGGAAACTCCCTGACT	569	Designed
GCLC	GCLC Primer 1	ACATCTACCACGCAGTCAAGGACC	CTCAAGAACATCGCCTCCATTCAG	134	(Vargas et al., 2008)
	GCLC Primer 2	CAGCTTTGGGTCGCAAGTA	GAGGGTCGGATGGTTGGG	519	Designed
MRP1	MRP1 Primer 1	ATGTGACTCTCAAGGGCTCC	ATGACATCCACTTGGGGCAG	412	(Vargas et al., 2008)
	MRP1 Primer 2	ATGTGACTCTCAAGGGCTCC	TGATGACATCCACTTGGGGC	414	Designed
NOX3	NOX3 Primer 1	CGACGAATTCAAGCAGATTGC	AAGAGTCTTTGACATGGCTTTGG	88	(Bánfi et al., 2004)
	NOX3 Primer 2	GAGGAACAAGTGTGTGCTGT	TGCCTGCCATTCAGCATAGT	512	Designed
	NOX3 Primer 3	CCTGGAGCGTTATCACCTGG	CCTCGAATGATGCGACCTCC	315	Designed
	NOX3 Primer 4	CGAGTTATTCTGGGTTCCGCA	CCCAGGTGATAACGCTCCAG	260	Designed

mXO	mXO Primer 1	AAAGGACCAGACGATTGCTCC	TCACACGTTCCCCTTCAAAAC	152	(Honorat et al., 2013)
	mXO Primer 2	CACGATGACGAGGACAACGG	TGAGGGAGCAATCGTCTGGT	586	Designed
mNOS	mNOS Primer 1	AAGGTCCGATTCAACAGCGT	GATGGTCGATCGGCTGGATT	516	(Honorat et al., 2013)
	mNOS Primer 2	ACTCATTGAACGGCTGGAGG	GGTCCTTCTCCATCTCGGGT	477	Designed
SOD1	SOD2 Primer 1	GATGTTACAACTCAGGTCGCTCTTC	CAGCAACTCTCCTTTGGGTTCTC	126	(Hüttemann et al., 2012)
	SOD2 Primer 2	CAGCGGTCGTGTAAACCTCA	CTCCAGCAACTCTCCTTTGG	380	Designed
G3BP1	G3BP1 Primer	CTCAGCCGCGCAGATTTTAT	AAGGTCTGCATGAACCTCCG	253	Designed
	G3BP1 Primer 2	TCAGATCCCACCACAAAGGC	TCGGAACATGATGGGTTTGGAA	230	Designed
G3BP2	G3BP2 Primer 1	TTGGTGCGGCGGAAACATT	TAGCATCAACCCTCGGCTGT	951	Designed
	G3BP2 Primer 2	GCTCTAGGCTCTCGGGAAGA	TTAGCATCAACCCTCGGCTTT	928	Designed
HuR	HuR Primer 1	TTCTCGGTTTGGGCGAATCA	ACCCATAGGGGAGAACCTGA	295	Designed
	HuR Primer 2	TCGGTTTGGGCGAATCATCA	ACCCATAGGGGAGAACCTGAA	292	Designed
Tia1	Tia1 Primer 1	CATAGCCCGCCTCAAGGATT	ACACATGGAAATGATTGCTCGTA	377	Designed
	Tia1 Primer 2	CATAGCCCGCCTCAAGGATT	GACAACGGTACTACTGCTCGTA	370	Designed
KEAP1	KEAP1 Primer 1	GGCGAGTAGAGGTAGGGGTC	TAGGGGCCCCGCCAT	133	Designed
	KEAP1 Primer 2	GCCCCGGGACTCTTATTGTG	CAAGAGAGGGTCTGCGTCTG	405	Designed
NLRP3	NLRP3	GGCGAGACCTCTGGGAAAAA	CTTCAAGGCTGTCCTCCTGG	99	Designed
GAPDH	GAPDH	GTGAAGGTCGGTGTCAACG	GTGAAGACGCCAGTAGACTC	299	Designed

Table 2: qPCR Primer Pairs used throughout experimentation. Primer pairs were either sourced from previous studies or designed. Primers were designed using the Thermo Fischer blast program. All designed primers span an exon-exon junction, have an annealing temperature of ~60°C, and a product size of 250-600.

Table 3

Solutions	Ingredients	Volume / Concentration	Supplier and Catalog Number
Hotshot Lysis Buffer (pH 12)	Sodium Hydroxide	25 mM	Fischer Scientific 15663580
	EDTA	0.2 mM	Sigma-AldrichE6758
Hotshot Neutralisation Buffer (pH 5)	Tris-hydrochloride	40 mM	Sigma-Aldrich T5941
PCR Master Mix	TDP-43 Forward Primer 5'-TGAAATCCGGGTGGTATTGG-3'	0.5 mM (0.75 µl)	Merck HI2955255-002
	Reverse TDP-43 Murine wildtype primer 5'-GGTGAGTTTAACCTTCAAGGGCT-3'	0.3 mM (0.5 µl)	Merck HI2955256-001
	Reverse TDP-43 Human wildtype transgene primer 5'-AGCTTGCTAGCGGATCCAGAC-3'	0.3 mM (0.5 µl)	Merck HI2955257-002
	GoTaq Flexi Green Buffer	3 µl	Promega M7805
	Magnesium Chloride	1.5 mM (3 µl)	
	GoTaq Flexi DNA Polymerase	0.2 µl	
	Deoxynucleotide triphosphates	0.1 mM (0.15 µl)	
	ddH20	8 µl	-
TAE (1x)	10x Tris-acetate-EDTA buffer	1:9	Invitrogen 15558-026
	ddH20	9:1	-
1.5% agarose gel	TAE Buffer (1x)	80 ml	-
	Lonza SeaKem LE Agarose	1.2g	Scientific Laboratory Supplies LTD LZ50004
	SYBR™ Safe DNA Gel Stain	4 µl	Invitrogen S33102
Ladder	Newtown Scientific 100bp Ladder	5 µl	NS Reagents MG17-10001
Superfrost Plus™ Adhesion slides	-	-	FISHER SCIENTIFIC UK LIMITED 15438060

30% Sucrose	Sucrose	60g	Sigma Aldrich 39378
	1 x PBS	200 ml	-
OCT	Optimal Cutting Temperature	-	CellPath KMA-0100-00A
4% PFA	16% Paraformaldehyde pH 7.4	10 ml	Electron Microscopy Sciences 15710
	1 x PBS	30 ml	-
Homogenisation Solution	Pierce™ RIPA Buffer radioimmunoprecipitation assay	1 ml	Life Technologies 89900
	Halt™ Protease inhibitor cocktail (100x)	1:100	Life Technologies 78420
	Halt™ Phosphatase inhibitor cocktail	1:100	VWR international 78420
BCA Assay (bicinchoninic acid)	Micro BCA Reagent A	0.5 ml	Protein Chemistry 23231
	Micro BCA Reagent B	0.48 ml	Protein Chemistry 23232
	Micro BCA Reagent C	0.02 ml	Life Technologies 23234
BSA Standard	Bovine Serum Albumin Standard 2mg/ml	-	Life Technologies 23210
Sample Buffer	NuPAGE™ LDS buffer (4x)	950µl	Life Technologies LTD (Invitrogen Division) 2201423
	Beta-mercaptoethanol	50µl	Sigma-Aldrich M6250-10ML
WB Running Buffer	NuPAGE MES Running buffer (20x)	1 :20	Life Technologies LTD (Invitrogen Division) NP000202
	ddH20	-	-
TPS	Revert™ 520 Total Protein Stain	10 ml	Li-cor Biosciences UK LTD 926-10011
5% Milk with 0.2% TBS-T	Milk Powder	2.5 g	-
	TBS 10x	100 ml	-

	Tween 20x	2 ml	Scientific Laboratory Supplies Ltd P1379-250ml
WB Gel	NuPAGE 4 to 12%, Bis-Tris 1.0 mm Mini Protein Gel	-	Life Technologies NP0323BOX
PVDF membrane	iBlot& trade; Transfer Stacks, PVDF	-	Life Technologies IB24001
Ladder	Chameleon Duo Pre-Stained Protein Ladder	2.5 µl	LI-COR 928-60000
Total Wash	Methanol, Optima LC/MS Grade	150 ml	Fisher Scientific UK Ltd A456-1 - (Fisher Chemical)
	Acetic Acid (glacial)	33.5 ml	VWR International 20104.312
	ddH20	316.5 ml	-
Antigen Retrieval Solution	Buffer A: Citric Acid 0.1 M pH 6	4.5 ml	Sigma-Aldrich C1909-500G
	Buffer B: Sodium Citrate 0.1 M pH 6	20.5 ml	Sigma W302600-1KG-K
	ddH20	225 ml	-
1 x PBS	PBS (10x)	100 ml	-
	ddH20	900 ml	-
Hydrophobic Pen	ImmEdge[R] Hydrophobic Barrier PAP Pen	-	Vector Laboratories H-4000
PBS 0.3% Triton	PBS (10x)	100 ml	-
	Triton 10%	30 ml	-
	ddH20	900 ml	-
3% BSA with 0.2% triton	Bovine Serum Albumin (BSA)	0.3g	Merck life science A4503-50G
	PBS (10x)	10 ml	-
	Triton 10%	20 µl	-
10% donkey serum with 0.3% triton	Donkey Serum	20 µl	Merck Life Science D9663-10ML
	PBS 0.3% triton	180 µl	-
PBS 0.1% Triton	PBS (10x)	100 ml	-
	Triton 10%	10 ml	-
	ddH20	900 ml	-

Mowiol	Mowiol 4-88 Reagent	-	Merck 475904
	Polyvinyl Alcohol with DABCO	-	Merck 10981
	Glycerol	-	Thermo Fischer Scientific BP229-1
10% Triton	Triton X-100	10 ml	Sigma-Aldrich A4503
	1xPBS	90 ml	-
Glass Coverslips	Microscope Glass Coverslips 22 x40 mm	-	VWR International 631-1370
RNA Synthesis Kit	RNeasy Plus Mini Kit	-	QIAGEN 74034
B-Mercaptoethanol	-	10 µl	Sigma-Aldrich M6250-10ML
70% Ethanol	-	-	-
cDNA Synthesis Kit	Maxima First Strand cDNA Synthesis kit for RT-qPCR	-	Fischer Scientific UK Limited 15279064
PCR + Primer Mix (per well)	PowerUp™ SYBR™ Green Master Mix – 5 ml	10 µl	Life Technologies LTD (Invitrogen Division) A25742
	Forward Primer	0.4 µl	-
	Reverse Primer	0.4 µl	-
Sample Mix (per well) qPCR	cDNA	0.5 µl	-
	DEPC-treated Water	8.7 µl	Sigma-Aldrich 95284-1L
Sample Mix (per well) Primer Optimisation	cDNA	0.1 µl	-
	DEPC-treated Water	9.1 µl	Sigma-Aldrich 95284-1L
1.5% agarose gel	TAE Buffer (1x)	80 ml	-
	Lonza SeaKem LE Agarose	1.2g	Scientific Laboratory Supplies LTD LZ50004
	SYBR™ Safe DNA Gel Stain	4 µl	Invitrogen S33102

Table 3: Solutions/items used throughout experimentation.

Statistics

As an indicator for number of animals needed per analysis, a power calculation was conducted to determine differences in the p62 protein concentration between NTg and Tg/Tg groups through western blotting. Using a two-sided test and power of 0.8 and 0.9, significance level of 0.05, effect size of 0.17, SD of 0.1024, the number of animals to fully power this experiment was determined to be 7-9 animals per group. Due to time limitations, this sample size was not achieved in all comparisons. Normality tests were performed on all experiments to determine whether results were normally distributed. For western blotting, immunohistochemistry, and qPCR data, two-sided unpaired T-tests were performed to determine significance. To determine differences in SG formation with terazosin treatment, a one-way ANOVA with Tukey post hoc test was utilised. Significance was analysed using GraphPad Prism 10.2.3. P values < 0.05 were determined to be significant, with the following annotation used: *P<0.05, **P<0.01, ***P<0.001, ****P<0.0001.

Results

During this study, we aimed to determine the role SG formation plays in ALS *in vivo*. Previous literature has indicated that SGs play a pathological role and could be a viable therapeutic target in ALS. However, investigating SG dynamics has primarily been conducted *in vitro* models with the use of an external stressor. No previous studies have evaluated the role of SGs in ALS *in vivo* without the use of an external stressor. Therefore, we aimed to address this gap in literature and enhance the understanding of the role of SGs in ALS.

As previous literature has reported both an increase and decrease in SG formation in ALS, we first sought to determine whether there are changes in SG formation in the hTDP43 mouse model. As previously discussed, multiple chronic cellular stress pathways are activated in ALS. The *in vitro* research focus of SGs in ALS has inhibited the investigation of pathways causing changes in SG dynamics. Therefore, we next sought to determine the chronic cellular pathways that could activate SG formation *in vivo*. As both a protective and pathological role has been attributed to SGs, we next sought to determine its role in ALS. Next, we sought to determine whether there were changes in the autophagy degradation pathway responsible for SG degradation that could be perpetuating SG pathology in ALS. Finally, as SGs have been suggested to be a viable target in ALS, we next sought to determine whether SG dynamics could be restored *in vivo* with terazosin treatment.

Part 1: Analysing changes in SG formation *in vivo*

SG markers are significantly upregulated at late symptomatic disease stage

Previous evidence suggests that there are changes in SG formation in ALS models. These studies, however, all made use of an external stressor, altering the physiological function of cells and therefore calling into question whether changes in SG dynamics directly result from ALS pathology. We, therefore, wanted to establish whether there were changes in SG dynamics in this specific ALS model. To do this, an *in vivo* ALS animal model, the hTDP43 mouse model, was selected due to its severe phenotype. The hTDP43 mouse model has a severe and fast-progressing phenotype with homozygous hTDP43 (Tg/Tg) mice showing TDP43 pathology, motor neuron cell death, body weight loss, and eventual hindlimb paralysis (Alhindi et al., 2023). It was hypothesized that the severe phenotype induced during pathology would be enough to stimulate changes in SG dynamics without the need for an external stressor, thus making results more translatable to humans.

In order to investigate changes in SG dynamics in vivo, several established SG markers were considered suitable for analyses, including TIA1, G3BP1, G3BP2, and HuR. G3BP1, G3BP2, and TIA1 have been attributed to play roles in SG formation, while HuR is a core SG protein (Campos-Melo et al., 2021; Matsuki et al., 2013) (Figure 3). To initially investigate whether changes in SG dynamics occur during ALS pathology, the late symptomatic time point was chosen as, at this stage, there is pronounced motor neuron loss and TDP43 cytoplasmic mislocalisation in the mouse model, a feature that is hypothesised to be influenced by SGs in ALS (Alhindi et al., 2023; Cui et al., 2024).

To visualise changes in SG dynamics in motor neurons immunohistochemistry staining was performed on homozygous (Tg/Tg) and non-transgenic (NTg) cryosectioned lumbar spinal cord sections using DAPI (a cell nuclear marker), ChAT (a marker for MNs), and G3BP2 (a marker for SG formation). Located in the lumbar region, sciatic motor neuron pools are of primary interest in ALS research, innervating the hindlimb muscles, which are predominantly affected during disease (Austin et al., 2022). Immunohistochemistry staining produced reliable labeling of SGs consistent with the literature (Figure 16A) (Yun et al., 2022) (Takayama et al., 2024) (H. Li et al., 2021).

Spinal cord sections were imaged at the ventral horn, the region in which motor neuron populations lie. Motor neuron counts were performed on each spinal cord section with identified motor neurons being counted for SG formation. A significant increase in SG formation was seen in spinal motor neurons of Tg/Tg mice compared to NTg littermates (Figure 16B) (Tg/Tg vs NTg: 0.1804 ± 0.0.04686 vs 0.02130 ± 0.0.04686. p = 0.0146). This indicates that an upregulation of SG formation is present in the hTDP43 mouse model during the late symptomatic disease stage, showing that an external stressor was not necessary to induce SG formation in this model.

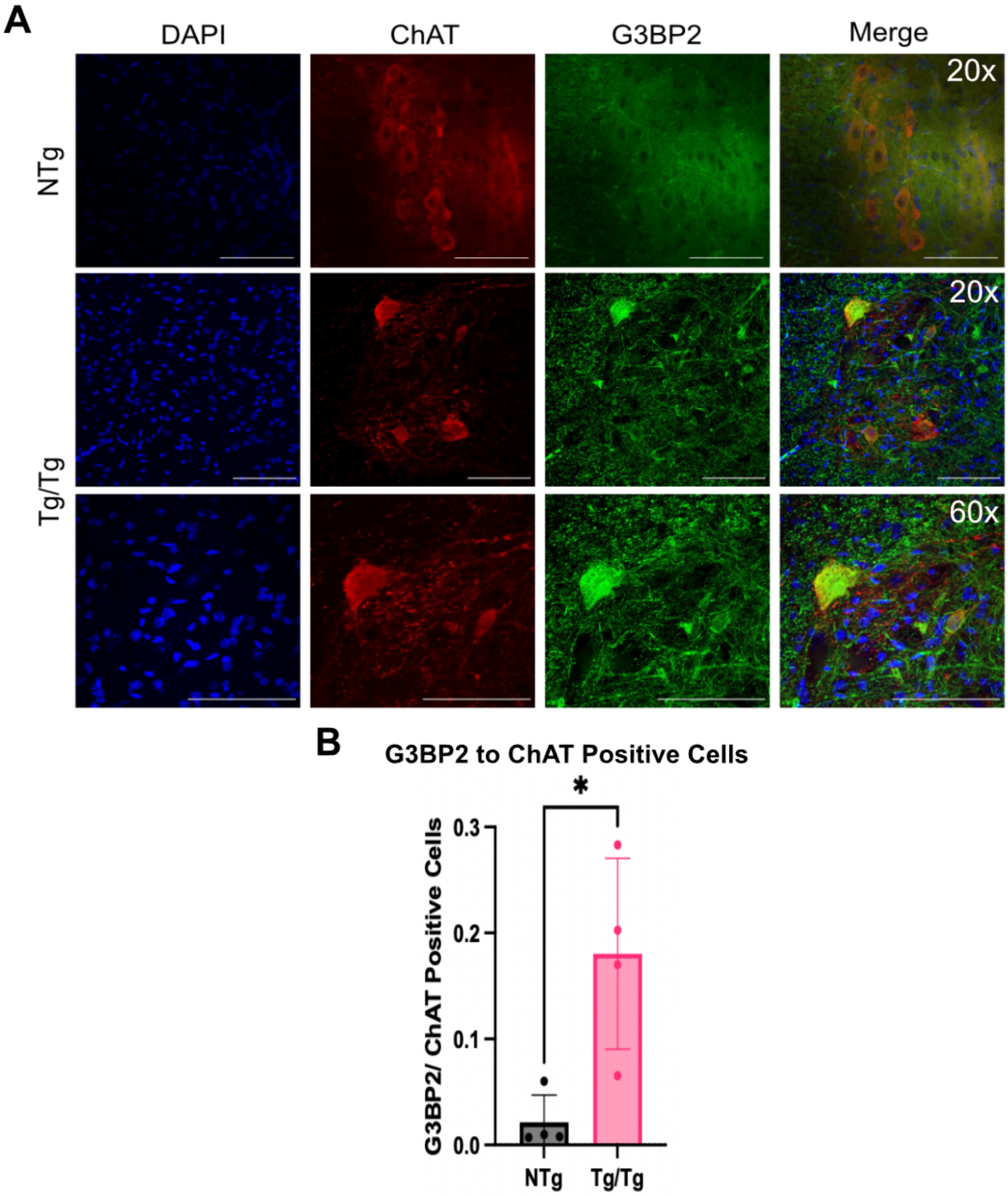

Figure 16: Significant upregulation of G3BP2 in motor neurons at a late symptomatic stage (P19) in hTDP43 mice (Tg/Tg) compared to littermate controls (NTg).

A) Representative confocal micrographs of spinal cord immunohistochemically labeled with DAPI (blue), ChAT (red), and G3BP2 (Green) for NTg and Tg/Tg mice at 20X and 60X (3rd row). Scale bar 100 µm.

B) Results are shown as mean ± SEM, with each data point representing the average G3BP2 to ChAT positive cells per mouse. An unpaired two-tailed t-test was performed to determine differences between NTg and Tg/Tg mice. n = 4 mice per genotype, n= 8-10 SPC sections per mouse. * = $p<0.05$

As a significant increase in SG formation was evident in spinal motor neurons of Tg/Tg mice with an G3BP2 antibody, we next sought to confirm this result with other established stress granule markers. TiaR, an RNA-binding protein involved in the formation of stress granules, was chosen to confirm the upregulation of stress granule formation seen in Tg/Tg SPC at the late symptomatic stage (P19).

Immunohistochemistry was performed on cryosectioned late symptomatic NTg and Tg/Tg lumbar spinal cord sections using DAPI, Neurotrace (staining Nissl bodies in neurons and glial cells), and TiaR antibody. Neurotrace stain is a widely used to stain for lumbar motor neurons (Alhindi et al., 2023; Chaytow et al., 2022; W. Lu et al., 2022). To optimise the TiaR antibody for use, two different conditions were utilised: blocking with 10% DS with 0.3% triton or blocking with 3% BSA with 0.2% triton (for full details, refer to the method section). However, neither of these conditions produced reliable staining in the ventral horn of either NTg or Tg/Tg mice (Figure 17).

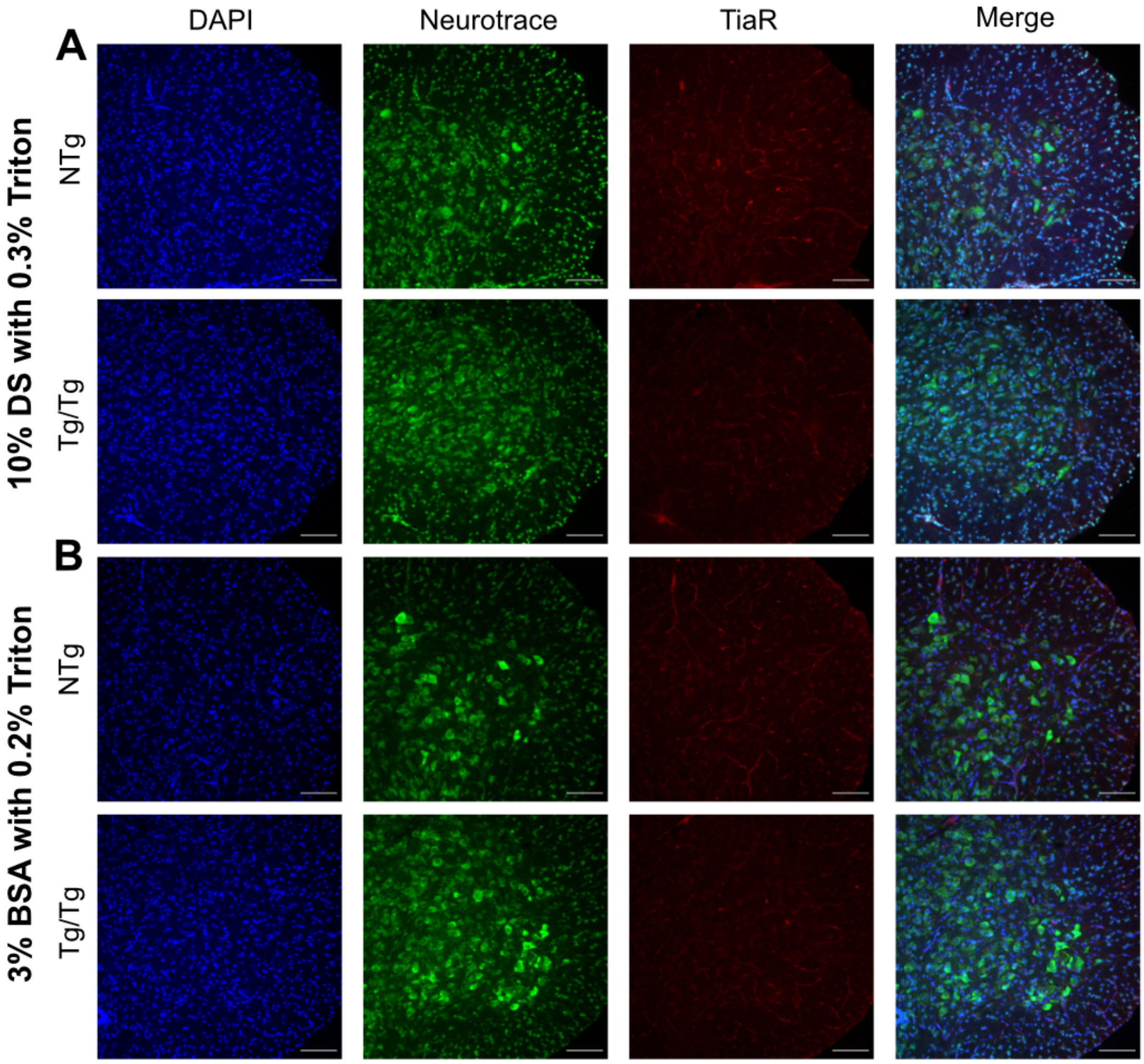

Figure 17: TiaR Immunohistochemistry optimisation on NTg and Tg/Tg SPC did not produce reliable staining. Late symptomatic NTg and Tg/Tg spinal cord sections were stained with DAPI (blue), Neurotrace, an MN marker (Green) and TiaR (red) using different blocking conditions to optimise TiaR antibody staining.

A) Representative confocal micrographs of SPC stained with DAPI (blue), neurotrace (Green), and Tiar (red) for NTg and Tg/Tg mice blocked with 10% DS with 0.3% triton (See methods section for further details). Scale bar 100 μm.

B) Representative confocal micrographs of SPC stained with DAPI (blue), neurotrace (Green), and Tiar (red) for NTg and Tg/Tg mice blocked with 3% BSA with 0.2% triton (See methods section for further details). Scale bar 100 μm.

As TiaR staining did not produce a reliable result, another established SG formation marker was utilised, G3BP1. To confirm our previous result, immunohistochemistry was performed on cryosectioned late symptomatic NTg and Tg/Tg lumbar spinal cord sections using DAPI, Neurotrace, and G3BP1 antibody. Multiple different conditions were again attempted to optimise G3BP1 staining for quantification, including blocking with 3% BSA with 0.2% triton, blocking with 10% DS with 0.3% triton, blocking with 5% DS with 0.3% triton, and blocking with 5% DS with 0.3% triton in addition to a 2-day primary incubation period. None of these conditions, however, produced reliable G3BP1 staining in either the NTg or Tg/Tg SPC; therefore, quantification was not performed (Figure 18).

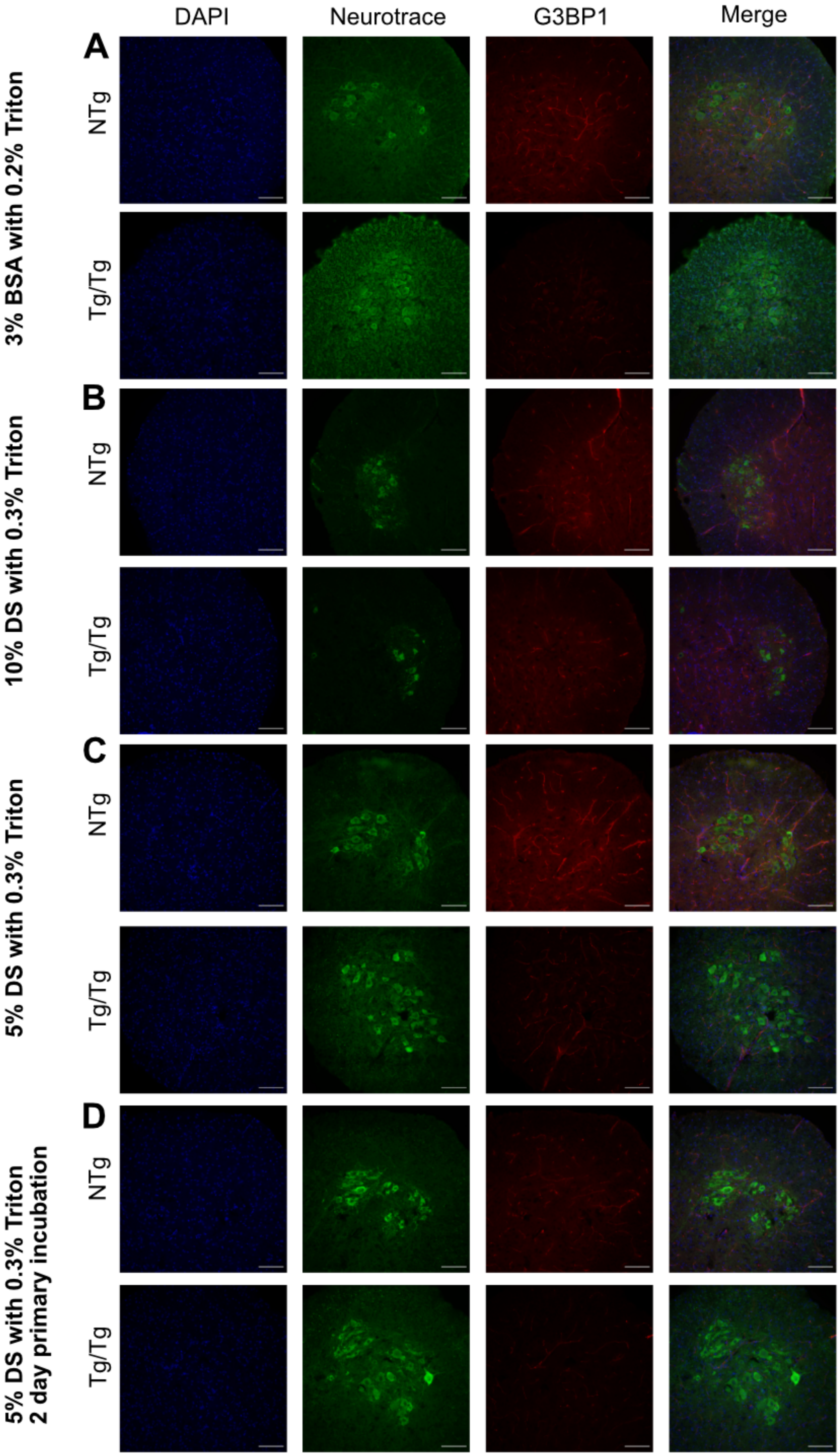
DAPI
Neurotrace
G3BP1
Merge
A
3% BSA with 0.2% Triton
NTg
Tg/Tg
B
10% DS with 0.3% Triton
NTg
Tg/Tg
C
5% DS with 0.3% Triton
NTg
Tg/Tg
D
5% DS with 0.3% Triton
2 day primary incubation
NTg
Tg/Tg

Figure 18: G3BP1 Immunohistochemistry optimisation on NTg and Tg/Tg SPC did not produce reliable staining. Late symptomatic NTg and Tg/Tg SPC were stained with DAPI (blue), Neurotrace (Green), and G3BP1 (red) with different blocking conditions applied to optimise G3BP1 antibody staining.

A) Representative confocal micrographs of late symptomatic NTg and Tg/Tg SPC stained with DAPI (blue), Neurotrace (Green), and G3BP1 (red) blocked with 3% BSA with 0.2% triton. Scale bar = 100um.

B) Representative confocal micrographs of late symptomatic NTg and Tg/Tg SPC stained with DAPI (blue), Neurotrace (Green), and G3BP1 (red) blocked with 10% donkey serum (DS) with 0.3% triton. Scale bar = 100um.

C) Representative confocal micrographs of late symptomatic NTg and Tg/Tg SPC stained with DAPI (blue), Neurotrace (Green), and G3BP1 (red) blocked with 5% donkey serum (DS) with 0.3% triton. Scale bar = 100um.

D) Representative confocal micrographs of late symptomatic NTg and Tg/Tg SPC stained with DAPI (blue), Neurotrace (Green), and G3BP1 (red) blocked with 5% donkey serum (DS) with 0.3% triton and a two-day primary antibody incubation period. Scale bar = 100um.

As confirmation of increased SG formation was not possible using TiaR or G3BP1 immunohistochemistry, we next sought to analyse whether there were changes in SG protein levels in Tg/Tg tissue at the late symptomatic stage. Quantitative western blotting was performed using the TiaR antibody in the brain and spinal cord of NTg and Tg/Tg mice (see methods for further details). This TiaR antibody has been extensively used for westerns and has been reported to produce two different antigen-specific bands at 42 and 50 kDa (Figure 19A, C) (Dubinski et al., 2023; X. Yang et al., 2018).

TiaR protein levels were significantly upregulated in the spinal cord tissue of Tg/Tg mice compared to NTg controls at the symptomatic stage (TiaR 50kDa SPC Tg/Tg vs NTg: 0.7654 ± 0.1775 vs 1.000 ± 0.1775, p = 0.2436) (TiaR 40kDa SPC Tg/Tg vs NTg: 1.455 ± 0.1412 vs 1.000 ± 0.1412, p = 0.0234) (Figure 19). This result, therefore, confirms and validates our previous result, showing that there are significant changes in SG expression in the spinal cord of Tg/Tg mice at the late symptomatic stage.

A significant upregulation of TiaR protein levels were also observed in brain tissue of Tg/Tg mice at the late symptomatic stage (Brain Tg/Tg vs NTg: 1.220 ± 0.7829 vs 1.000 ± 0.7829, p = 0.0260) (TiaR 42kDa Brain Tg/Tg vs NTg: 1.112 ± 0.1726 vs 1.000 ± 0.1726, p = 0.5384) (Figure 19). Therefore, combined, these results show that there is a significant upregulation of SG formation in Tg/Tg brain and spinal cord tissue at the late symptomatic stage of disease.

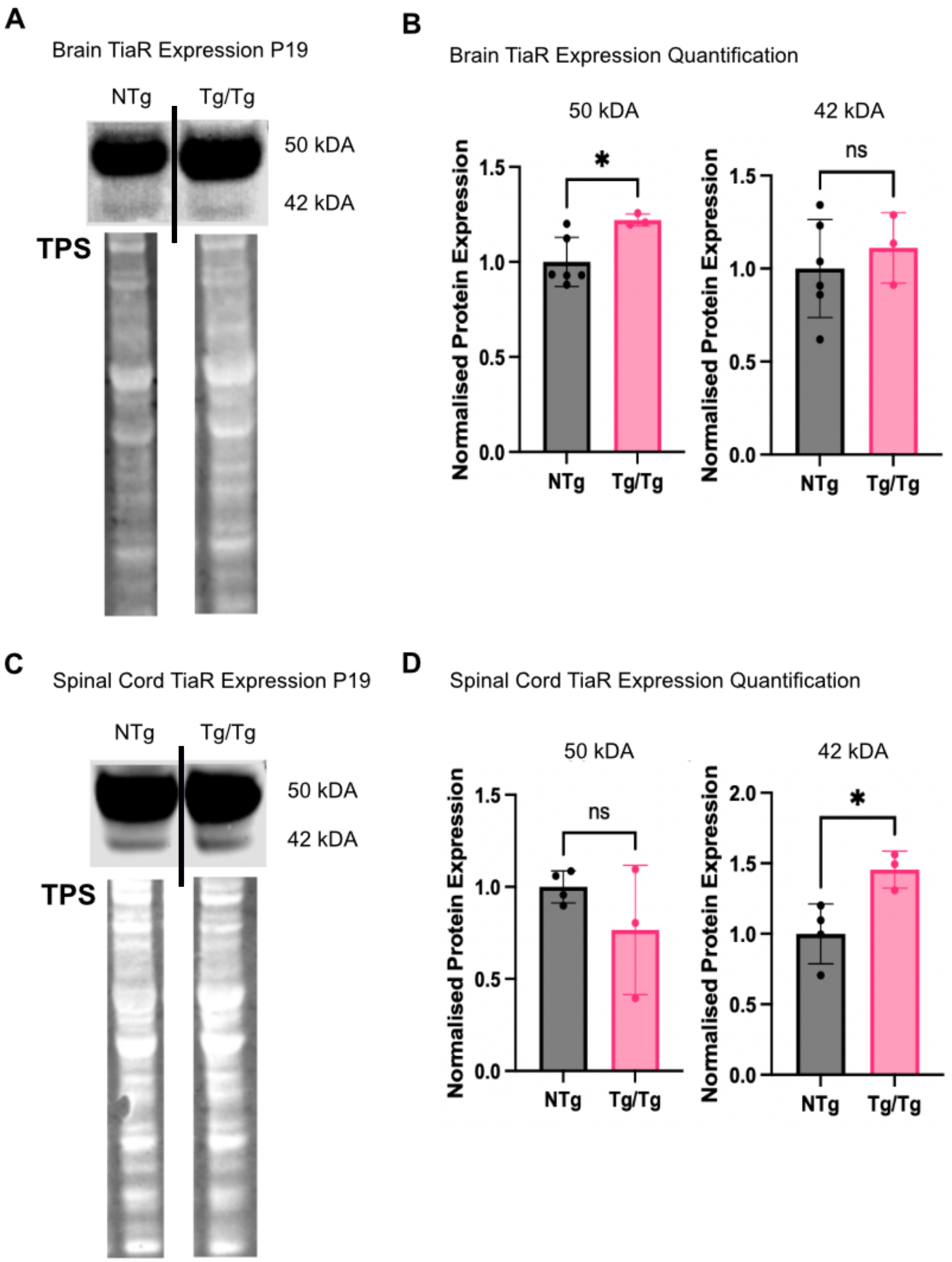

Figure 19: Significant protein upregulation of TiaR at the late symptomatic stage (P19) in hTDP43 Tg/Tg mice.

A, C) Western blot images showing representative bands for TiaR expression in NTg and Tg/Tg in the brain and spinal cord tissue at the late symptomatic stage (P19). Black lines indicate where the same membrane has been cut to create the example image.

B, D) Amount of TiaR expression at the late symptomatic stage (P19) in both the brain and the spinal cord. Results are shown as mean ± SEM, with each point representing TiaR expression from one mouse. Differences in TiaR expression for NTg and Tg/Tg mice were analysed with unpaired two-tailed t-tests. n = 3-6 mice per group. *p<0.05; ns = non-significant

To confirm these changes seen in SG protein expression using the TiaR antibody, antibodies targeting G3BP1 and G3BP2 were also tested for western blotting. Western blotting was performed on both early symptomatic stage (P15) and late symptomatic stage (P19) NTg and Tg/Tg spinal cord tissue with either G3BP1 or G3BP2 antibodies. Western blotting with either antibody did not produce reliable results, with multiple non-specific bands visible on each membrane (Figure 20A-D). The antigen-specific bands, indicated by the red arrow, were either absent or were weaker than the non-specific binding produced by the antibodies. Therefore, results were unable to be quantified.

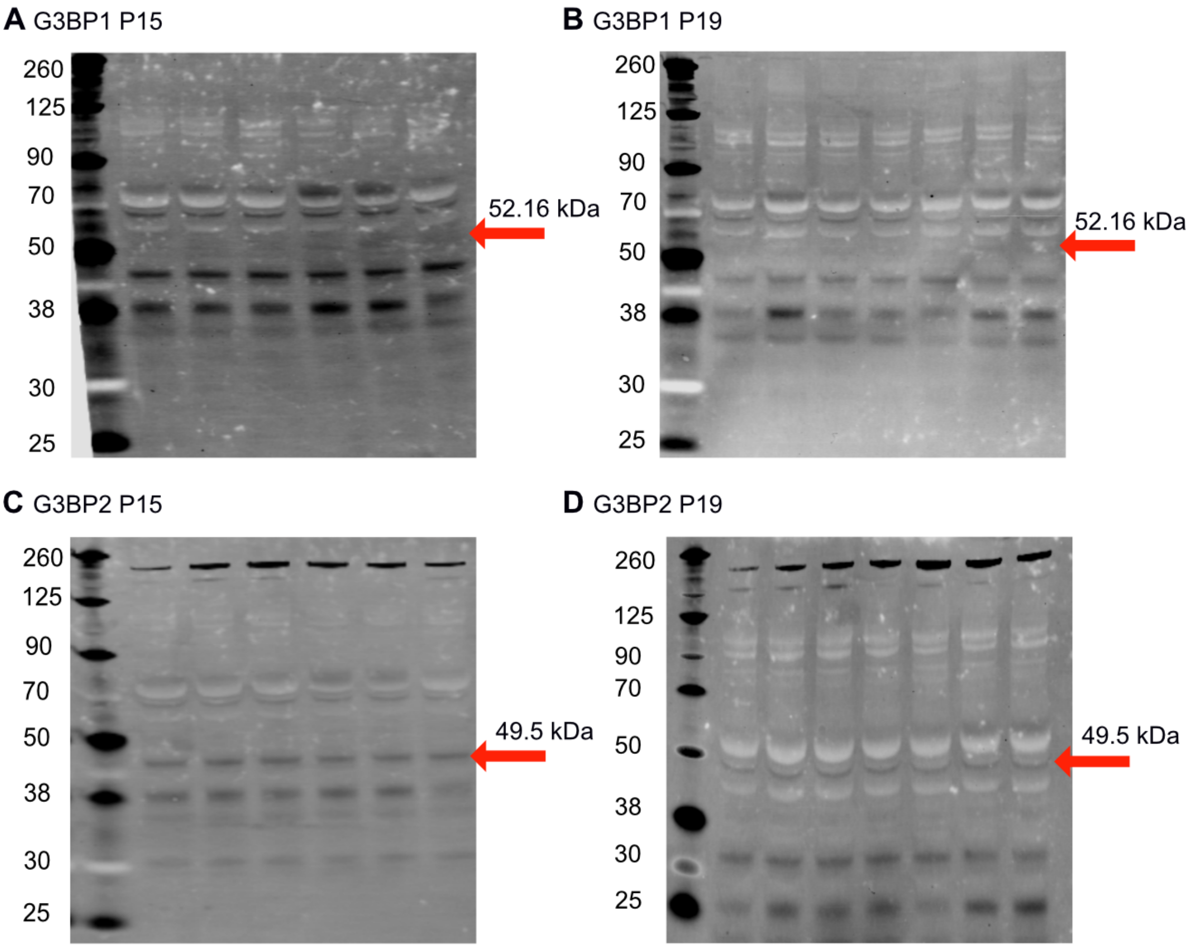

Figure 20: G3BP1 and G3BP2 western blotting optimisation on NTg and Tg/Tg spinal cords did not produce reliable product bands.

A-B) Western Blotting images showing bands for G3BP1 expression in NTg and Tg/Tg spinal cord tissue at the early symptomatic (P15)(A) and late symptomatic stage (P19)(B).

The recorded molecular weight for G3BP1 is 52.16 kDa (red arrow), indicating the correct height of the antigen-specific band.

C-D) Western Blotting images showing bands for G3BP2 expression in NTg and Tg/Tg spinal cord tissue at the early symptomatic (P15)(C) and late symptomatic stage (P19)(D). The recorded molecular weight for G3BP2 is 49.5 kDa (red arrow), indicating the correct height of the antigen-specific band.

SG markers are significantly altered at the transcriptome level in the late symptomatic disease stage

A significant upregulation in SG formation markers was seen in both brain and spinal cord tissue of Tg/Tg mice at the late symptomatic stage. As discussed previously, in the process of SG formation there is a global inhibition of protein synthesis. Translation of specific SG proteins are however able to be translated during this time (J. Wang et al., 2022). We, therefore, wanted to determine whether changes seen in SG formation proteins were a result of increased transcription.

To determine whether there were changes at the transcriptome level, primer pairs were designed to target established SG markers: G3BP1, G3BP2, HuR, and Tia1. Primers were optimised for their specificity by running each primer pair using an NTg sample on a qPCR optimisation protocol with a temperature gradient spanning 50-63°C. Amplification curves were examined for their consistency over the temperature gradient, with primer pairs performing consistently over the temperature gradient chosen preferentially over others. Next, the melt curves were analyzed for the presence of a singular peak (Figure 21A-H).

Primer pairs that had a tight amplification curve and a melt peak showing a singular peak were run on a 1.5% agarose gel to confirm product specificity (Figure 21I). Running products on a gel provides a more accurate confirmation of the production of a singular product than melt curves. Therefore, despite both TiaR primer pairs producing a double peak in their melt curves, they both produced a singular product on a gel, therefore are deemed specific.

Both HuR, G3BP1, and Tia1 primer pairs showed a single band, indicating that the primer pairs produced a singular product. HuR primer pair 2 was chosen as it showed more consistency in its amplification curve. Tia1 primer pairs both showed a singular band and similar amplification curves; therefore, Tia1 primer pair 1 was chosen. G3BP1 primer pair 1 was chosen as it produced a stronger band.

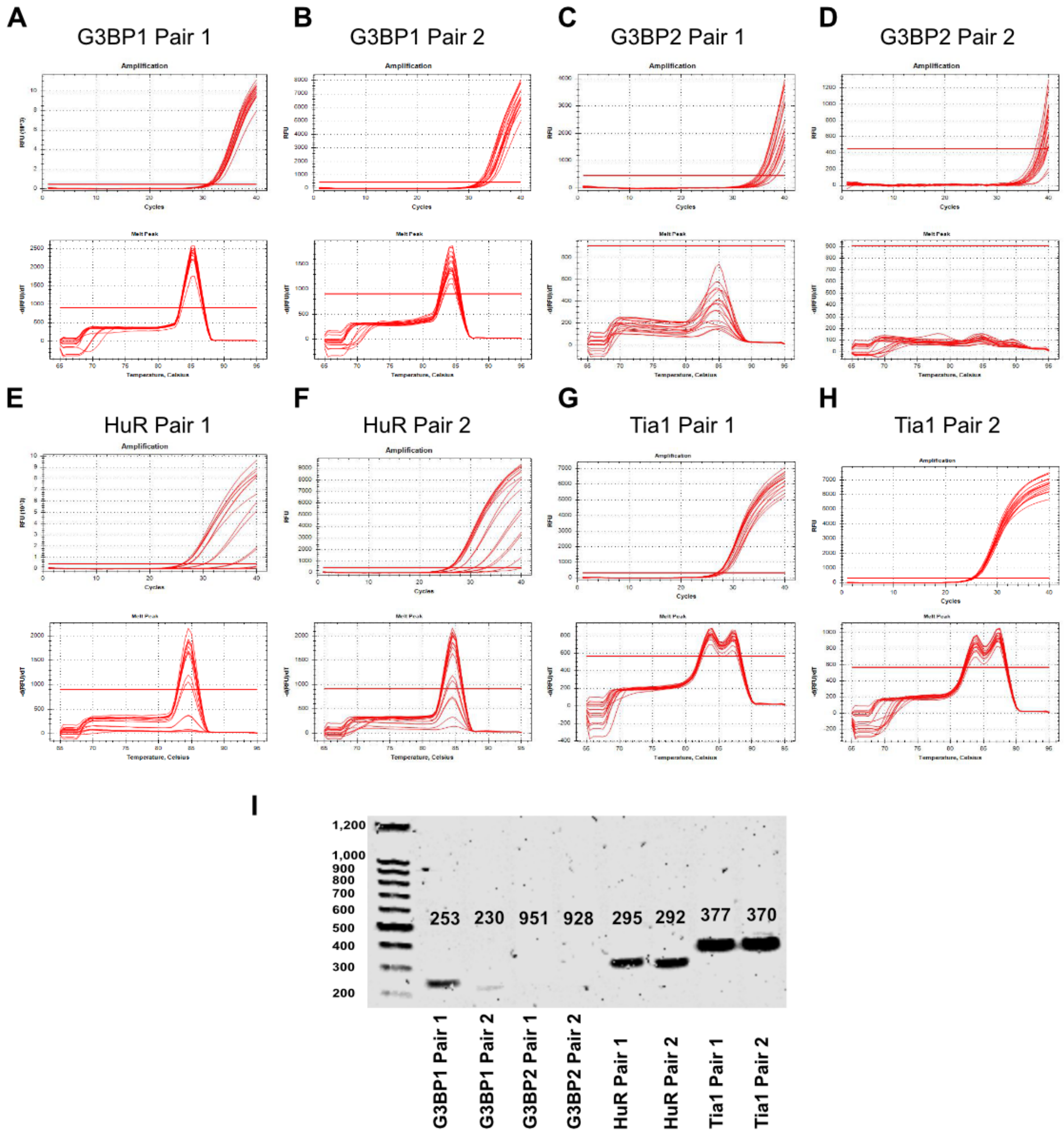

Figure 21: qPCR optimisation for SG marker primer pairs. Primer pairs designed to target G3BP1, G3BP2, HuR, and TiaR were optimised using a temperature gradient spanning 50-63°C and a singular NTg sample (for further details, refer to methods section).

A-H) Amplification and melt curves generated from the qPCR optimisation protocol for each pair. Amplification curves are the top graphs, with melt curves below. Refer to Figure 11 for further details regarding selection and for better visualisation of axes.

(I) Selected Primer pairs were then run on a 1.5% agarose gel to confirm product specificity. Numbers indicate the predicted height of each product. Black lines indicate where the same gel has been cut to create the example image.

With these optimised primers, we sought to determine whether there were differences in SG formation at the transcriptome level in late symptomatic spinal cord tissue using qPCRs. Samples were run along with a non-template control to test for possible contamination and a household control gene, GAPDH, for normalization. GAPDH is one of the most frequently used genes for normalisation of qPCRs (Kozera & Rapacz, 2013; R. Mori et al., 2008).

Prior to the analysis of results, the non-template control and a singular NTg sample were run for each primer pair to check for contamination (Figure 22A). No contamination was evident in either non-template control; therefore, quantification of qPCR results proceeded (see methods section for further details).

A significant upregulation in G3BP1 transcription was observed in Tg/Tg spinal cord tissue compared to NTg controls (G3BP1 SPC Tg/Tg vs NTg: 2.078 ± 0.417 vs 1.048 ± 0.417, p = 0.0484) (Figure 22D). Interestingly, there was a significant decrease and no change seen in HuR and Tia1 transcription in Tg/Tg spinal cord tissue, respectively (HuR SPC Tg/Tg vs NTg: 0.7085 ± 0.1226 vs 1.012 ± 0.1226, p = 0.0481) (Tia1 SPC Tg/Tg vs NTg: 0.8520 ± 0.08257 vs 1.007 ± 0.08257, p = 0.1100) (Figure 22B-C).

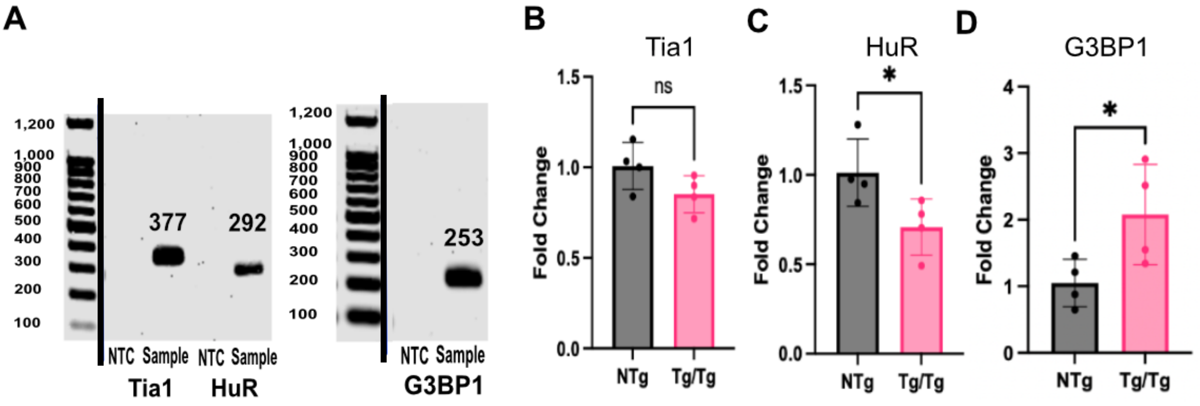

Figure 22: SG markers transcription is significantly altered at the late symptomatic stage in SPC Tg/Tg mice. Optimised primer pairs targeting Tia1 and HuR translation were used to detect changes in translation in SPC of NTg and Tg/Tg mice using qPCR protocol (found in methods).

A) 1.5% agarose gel showing bands Non-Template control (NTC) and NTg sample band for Tia1 and HuR translation in late symptomatic spinal cord tissue. Black lines indicate where the same membrane has been cut to create the example image.

B-D) Tia1, HuR, and G3BP1 expression in NTg and Tg/Tg spinal cords at the late symptomatic stage. Results are shown as mean ± SEM, with each point representing protein translation from one mouse. Differences in Tia1 and HuR translation for NTg and Tg/Tg mice were analysed with unpaired two-tailed t-tests. n = 4 mice per group. *$p<0.05$, ns = non-significant

TDP43 and SG markers colocalise in Tg/Tg spinal cords

Significant changes in SG markers at both the transcriptome and protein levels were observed in both the spinal cord and brain of Tg/Tg. As SG formation is hypothesized to act as a seeding mechanism for TDP43 aggregation, we next wanted to investigate whether TDP43 and stress granule markers colocalize in Tg/Tg tissue at the late symptomatic stage. This time point was selected as TDP43 cytoplasmic mislocalization has been previously observed at this timepoint in the hTDP43 mouse model (Alhindi et al., 2023).

NTg and Tg/Tg cryosectioned spinal cord sections were stained with DAPI, Neurotrace, TDP43, and G3BP2. Stained spinal cord sections were then observed to determine whether there was overlap between the neurotrace, G3BP2, and TDP43 channels to determine whether there is colocalisation of SGs and TDP43 protein in motor neurons. In Tg/Tg spinal cord motor neurons, colocalisation between TDP43 and G3BP2 was observed (Figure 23). No colocalization was observed in NTg spinal cord sections. This indicates that the significant changes seen in SG formation could be driving TDP43 mislocalisation in the spinal cord.

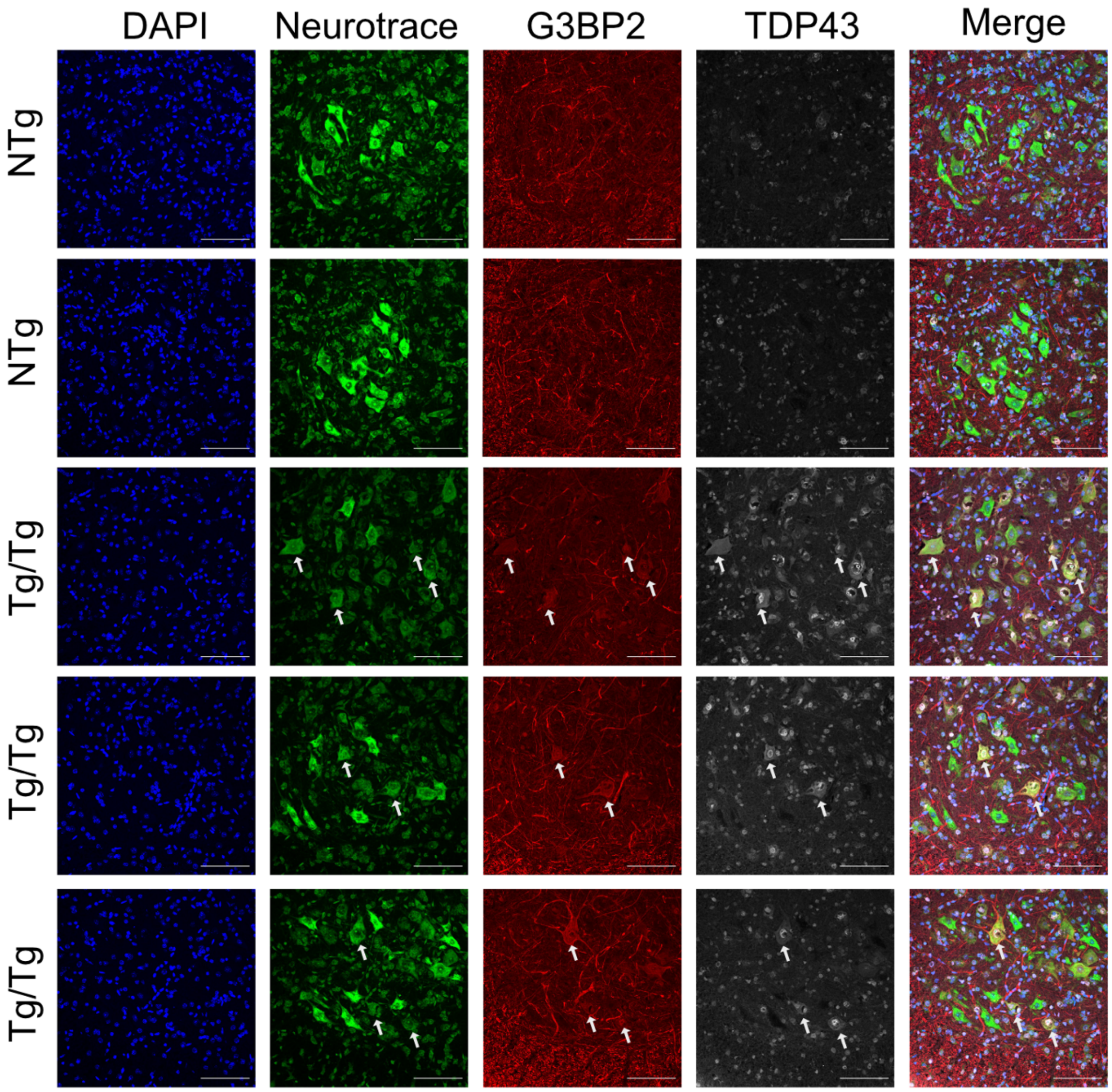

Figure 23: G3BP2 and TDP43 colocalize in motor neurons in Tg/Tg mice at the late symptomatic stage. Representative confocal micrographs of SPC stained with DAPI (blue), Neurotrace (green), G3BP2 (red), and TDP43 (grey) for NTg and Tg/Tg mice at 20X. Arrows indicate motor neurons positive for both TDP43 and G3BP2. Scale bar 100 µm.

SG markers are unaltered at an early symptomatic stage

Significant changes in SG dynamics have, therefore, been observed in Tg/Tg mice in both spinal cord and brain tissue at the late symptomatic stage. As the presence of SG has been found at early disease stages in patient spinal cord tissue (F. Mori et al., 2024), we next sought to determine whether changes in SG dynamics occurred earlier in disease pathology in the hTDP43 mouse model at both the protein and transcriptome level.

To determine changes at the protein level, western blotting was performed on NTg and Tg/Tg brain and spinal cord tissue using the TiaR antibody (see methods for further details). With the current available sample sizes, there was no difference in TiaR expression in either brain or spinal cord Tg/Tg tissue compared to NTg mice at the early symptomatic stage (Figure 24B, D) (TiaR 50kDa Brain Tg/Tg vs NTg: 1.154 ± 0.1305 vs 1.000 ± 0.1305, p = 0.3029) (TiaR 42 kDa Brain Tg/Tg vs NTg: 1.198 ± 0.2243 vs 1.000 ± 0.2243, p = 0.4265) (TiaR 50kDa SPC Tg/Tg vs NTg: 0.8365 ± 0.1229 vs 1.000 ± 0.1229, p = 0.2542) (TiaR 42kDa SPC Tg/Tg vs NTg: 0.7731 ± 0.1965 vs 1.000 ± 0.1965, p = 0.3124).

As differences in transcription occur prior to changes in protein levels, we next wanted to determine whether SG transcription was altered at the early symptomatic stage in spinal cord tissue. Previously optimised primer pairs targeting Tia1, HuR, and G3BP1 were used to detect changes in SG transcription using qPCRs. Samples were run along with a household control gene, GAPDH, and a non-template control. As no contamination was evident in the non-template controls and products produced a single band (Figure 25E), quantification of qPCR results proceeded.

No significant changes in transcription in any SG markers (Tia1, HuR, and G3BP1) was observed between Tg/Tg spinal cord tissue compared to NTg controls (Figure 24F-H) (Tia1 SPC Tg/Tg vs NTg: 0.9543 ± 0.2281 vs 1.032 ± 0.2281, p = 0.7516) (HuR SPC Tg/Tg vs NTg: 0.9073 ± 0.2218 vs 1.030 ± 0.2218, p = 0.6097 (G3BP1 SPC Tg/Tg vs NTg: 1.149 ± 0.1572 vs 1.008 ± 0.1572, p = 0.4042). These results together indicate that SG markers are not significantly changed at the early symptomatic stage in Tg/Tg mice and are instead only upregulated at the late symptomatic stage.

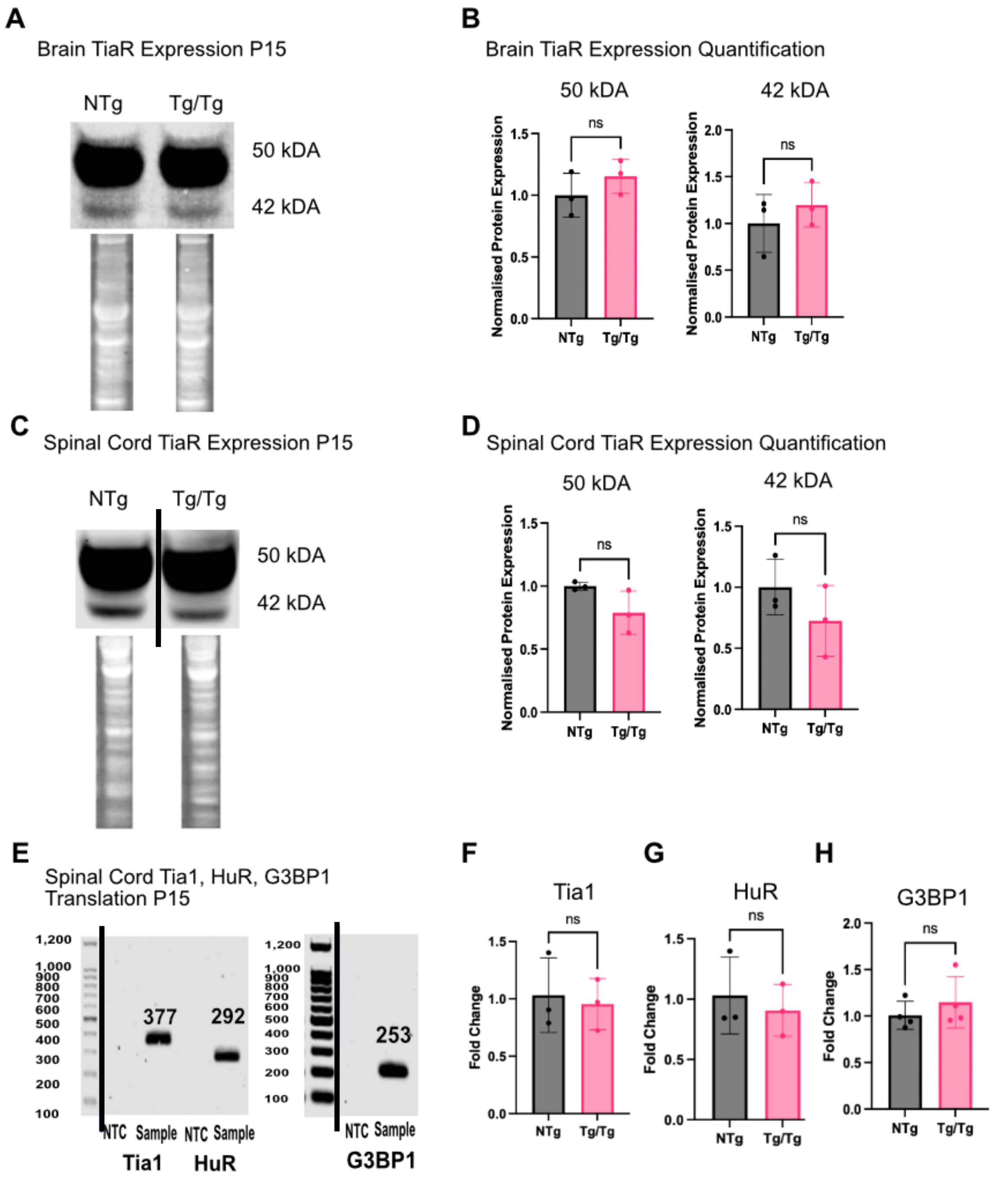

Figure 24: No changes in SG formation at either the protein or transcriptome level in Tg/Tg SPC at the early symptomatic stage. Western blotting (A-D) and qPCRs (E-G) were used to determine differences at the protein and translation level of SG markers between Tg/Tg and NTg mice.

A, C) Western blot images showing representative bands for TiaR expression in NTg and Tg/Tg in the brain and spinal cord at the early symptomatic stage. Black lines indicate where the same membrane has been cut to create the example image.

B, D) Amount of TiaR expression at the early symptomatic stage in both the brain and the spinal cord. Results are shown as mean ± SEM, with each point representing TiaR expression from one mouse. Differences in TiaR expression for NTg and Tg/Tg mice were analysed with unpaired two-tailed t-tests. n = 3 mice per group.

E) 1.5% agarose gel showing bands Non-Template control (NTC) and NTg sample band for Tia1, HuR, and G3BP1 translation in early symptomatic stage spinal cord tissue. Black lines indicate where the same membrane has been cut to create the example image.

F-G) Tia1, HuR, and G3BP1 expression in NTg and Tg/Tg spinal cords at the early symptomatic stage. Results are shown as mean ± SEM, with each point representing protein translation from one mouse. Differences in Tia1 and HuR translation for NTg and Tg/Tg mice were analysed with unpaired two-tailed t-tests. n = 3 mice per group. ns = non-significant.

Part 2: Analysing changes in chronic cellular stress pathways

Neuroinflammation is upregulated at the late symptomatic stage

As covered in the introduction, multiple chronic cellular pathways can induce SG formation. As we see a significant upregulation in SG formation at the late symptomatic stage in hTDP43 mice, we next wanted to explore what chronic cellular pathways could be causing this activation. Inflammation and oxidative stress both induce chronic cellular stress and were chosen for investigation.

To investigate the role of inflammation, immunohistochemistry was performed on cryosectioned late symptomatic NTg and Tg/Tg lumbar spinal cord sections using DAPI stain, Neurotrace stain, and Iba1 antibody, an established microglial marker (see methods section for further details) (Figure 25A).

A significant upregulation in Iba1-positive cells and area covered by Iba1 staining (Iba1 particle area) was observed in Tg/Tg spinal cords compared to NTg controls (Figure 25B, C) (Iba1+ cells SPC Tg/Tg vs NTg: 194.4 ± 11.15 vs 134.1 ± 11.15, $p = 0.0010$) (Iba1+ Particle Area SPC Tg/Tg vs NTg: 55192 ± 4640 vs 40182 ± 4640, $p = 0.0144$). This result shows that inflammation is significantly upregulated at the late symptomatic stage in Tg/Tg mice and could possibly be driving SG formation.

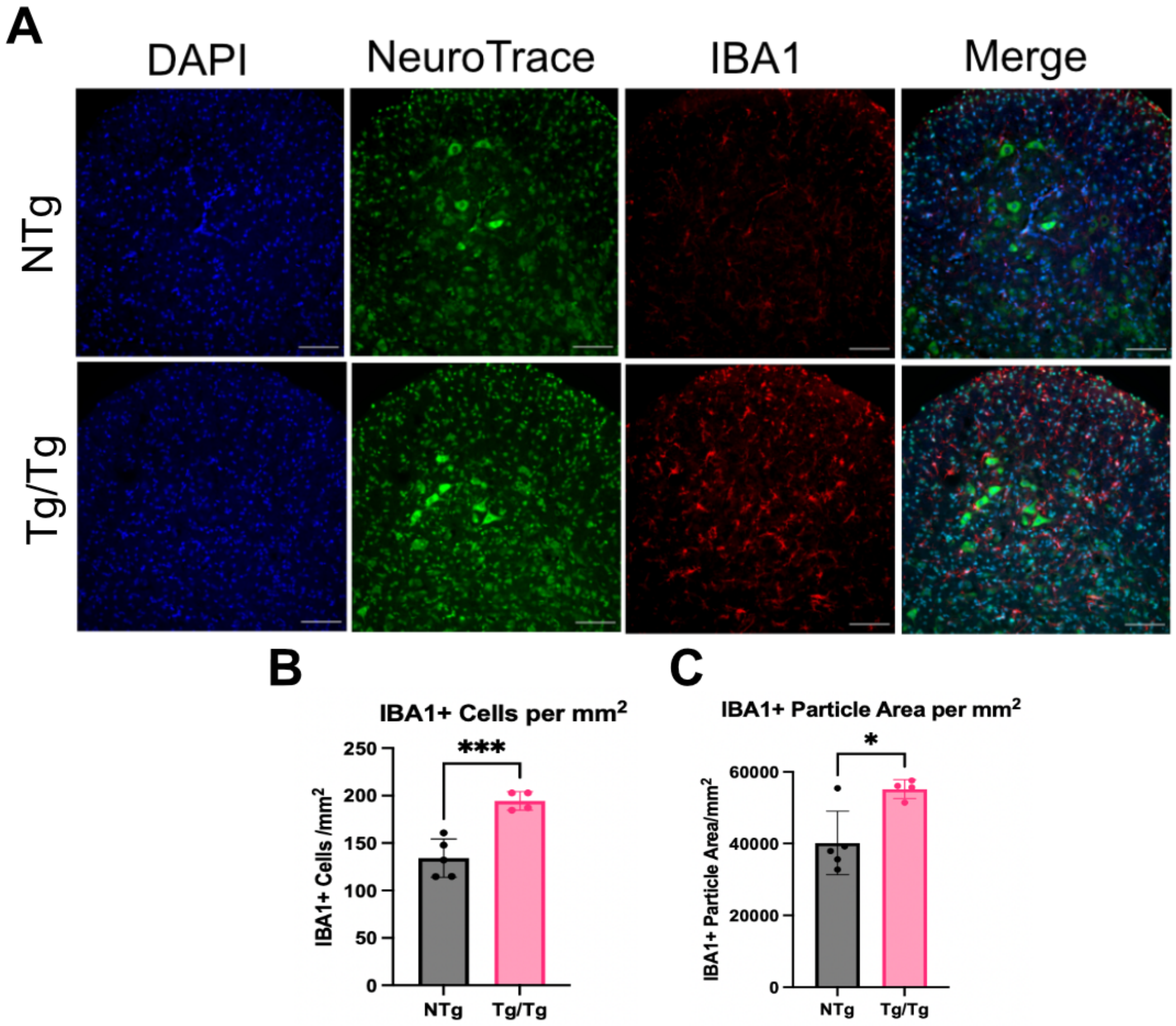

Figure 25: Significant upregulation of Iba1 in Tg/Tg SPC at the late symptomatic stage.

A) Representative fluorescent images of spinal cords stained with DAPI (blue), Neurotrace (green), and Iba1 (red) for NTg and Tg/Tg mice at 20X. Scale bar 100μm.

B) Results are shown as mean ± SEM, with each data point representing the average Iba1 positive cells per mouse. An unpaired two-tailed t-test was performed to determine differences between NTg and Tg/Tg mice. n = 4-5 mice per genotype, n= 6 spinal cord sections per mouse. *** = $p<0.0001$.

C) Results are shown as mean ± SEM, with each data point representing the average Iba1 positive particle area per mouse. An unpaired two-tailed t-test was performed to determine differences between NTg and Tg/Tg mice. n = 4-5 mice per genotype, n= 6 spinal cord sections per mouse. * = $p<0.05$.

Oxidative Stress is upregulated at the late symptomatic stage

Next, to investigate changes in oxidative stress, primer pairs were designed to target gene transcripts involved in the NrF2-ARE pathway: CytC, GCLC, GCLM, HMOX1, KEAP1, NQO1, NrF2, and MRP1 (Figure 2). The Nrf2-ARE pathway is activated in response to oxidative stress (Buendia et al., 2016).

Primer pairs were optimised by running an NTg sample on the qPCR optimisation protocol with a temperature gradient spanning 50-63°C. Amplification and melt curves generated by the qPCR protocol were analysed for consistency and singular peaks (Figure 26A-P). Selected primer pairs were then run on a 1.5% agarose gel to confirm product specificity (Figure 26Q).

After optimisation, KEAP1 primer pair 1, NrF2 primer pair 2, HMOX1 primer pair 2, CytC primer pair 2, NQO1 primer pair 1, GCLM primer pair 1, MRP1 primer pair 2, and GCLC primer pair 1 were deemed as specific and consistent across the temperature gradient and thus were used to detect changes in the transcriptome between NTg and Tg/Tg mice.

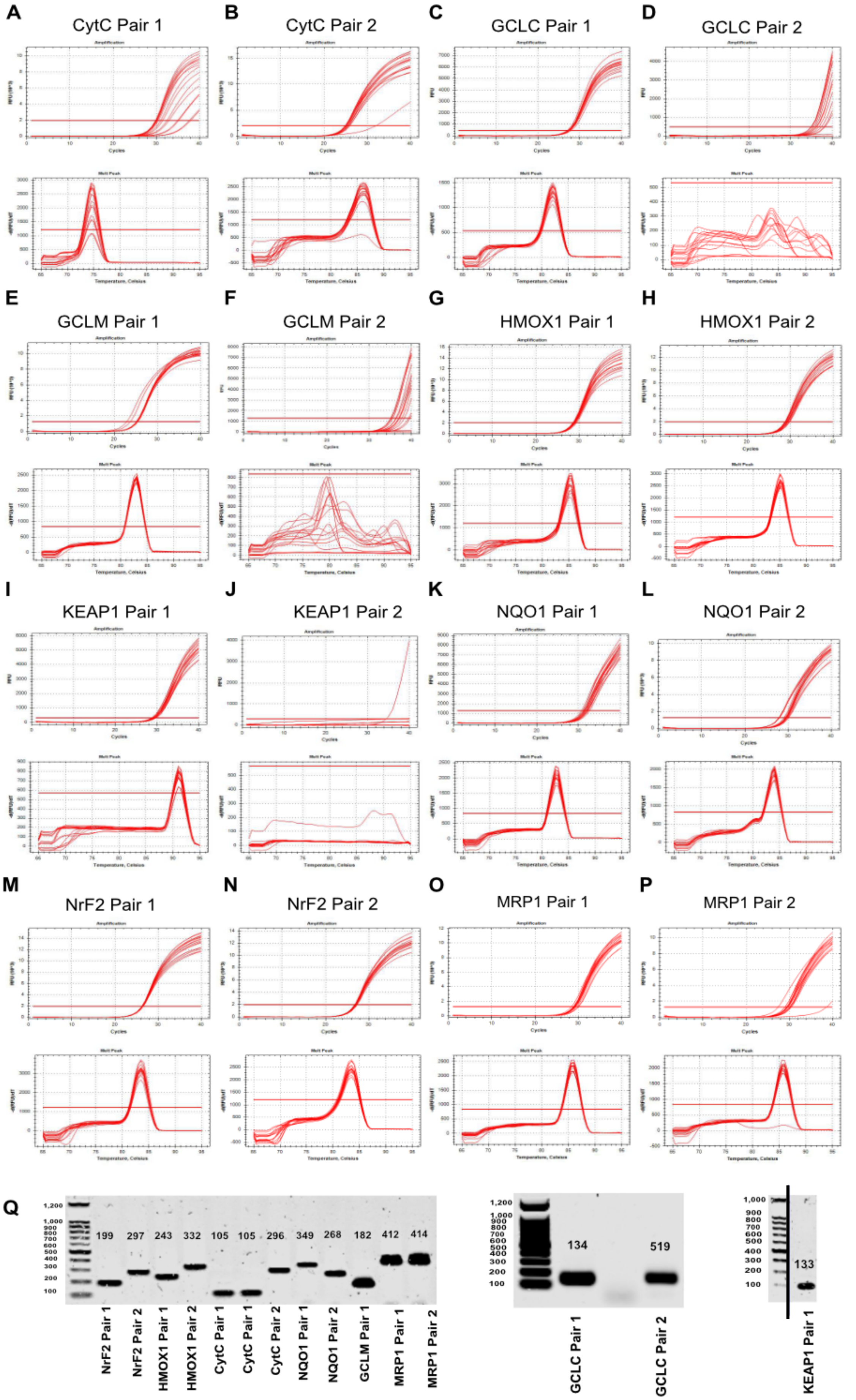
A
CytC Pair 1
B
CytC Pair 2
C
GCLC Pair 1
D
GCLC Pair 2
E
GCLM Pair 1
F
GCLM Pair 2
G
HMOX1 Pair 1
H
HMOX1 Pair 2
I
KEAP1 Pair 1
J
KEAP1 Pair 2
K
NQO1 Pair 1
L
NQO1 Pair 2
M
NrF2 Pair 1
N
NrF2 Pair 2
O
MRP1 Pair 1
P
MRP1 Pair 2
Amplification
Cycles
Melt Peak
Temperature, Celsius
Q
1,200
1,000
900
800
700
600
500
400
300
200
100
199
297
243
332
105
105
296
349
268
182
412
414
NrF2 Pair 1
NrF2 Pair 2
HMOX1 Pair 1
HMOX1 Pair 2
CytC Pair 1
CytC Pair 1
CytC Pair 2
NQO1 Pair 1
NQO1 Pair 2
GCLM Pair 1
MRP1 Pair 1
MRP1 Pair 2
134
519
GCLC Pair 1
GCLC Pair 2
133
KEAP1 Pair 1

Figure 26: qPCR optimisation for oxidative stress marker primer pairs. Oxidative Stress marker primer pairs were designed to target CytC, GCLC, GCLM, HMOX1, KEAP1, MRP1, NQO1, and NrF2 to determine whether there were changes in the transcriptome level of oxidative stress. Primer pairs were optimised using a temperature gradient spanning 50-63°C and a singular NTg sample (for further details, refer to methods section).

A-P) Amplification and melt curves generated from the qPCR optimisation protocol for each pair. Amplification curves are the top graphs, with melt curves below. Refer to Figure 11 for further details regarding selection and better visualisation of axes.

(Q) Selected Primer pairs were then run on a 1.5% agarose gel to confirm product specificity. Numbers indicate the predicted height of each product. Black lines indicate where the same gel has been cut to create the example image.

With these optimised primer pairs, we examined whether there were differences in oxidative stress at the transcriptome level between NTg and Tg/Tg spinal cord tissue at the late symptomatic stage. Samples were run on a 1.5% agarose gel along with a non-template control to test for possible contamination and a household control gene, GAPDH. As no contamination was evident in the non-template controls and products produced a single band (Figure 28A), quantification of qPCR results proceeded.

HMOX1, NQO1, and GCLM transcription were significantly upregulated in Tg/Tg spinal cord tissue compared to NTg controls (Figure 27C, F, G) (HMOX1 SPC Tg/Tg vs NTg: 3.026 ± 0.2290 vs 1.001 ± 0.2290, $p = 0.0001$) (NQO1 SPC Tg/Tg vs NTg: 1.914 ± 0.1644 vs 1.014 ± 0.1644, $p = 0.0016$) (GCLM SPC Tg/Tg vs NTg: 2.150 ± 0.1583 vs 1.003 ± 0.1583, $p = 0.0004$). Cytc, GCLC, KEAP1, NrF2 and MRP1 translation showed no change in translation between Tg/Tg spinal cord tissue compared to NTg controls (Figure 27B, D, E, H, I) (CytC SPC Tg/Tg vs NTg: 0.9303 ± 0.09414 vs 1.005 ± 0.09414, $p = 0.4603$) (GCLC SPC Tg/Tg vs NTg: 1.724 ± 0.4534 vs 1.073 ± 0.4534, $p = 0.2012$) (KEAP1 SPC Tg/Tg vs NTg: 1.303 ± 0.8879 vs 1.049 ± 0.8879, $p = 0.3641$) (MRP1 SPC Tg/Tg vs NTg: 1.193 ± 0.2110 vs 1.026 ± 0.2110, $p = 0.4581$) (Nrf2 SPC Tg/Tg vs NTg: 1.050 ± 0.1485 vs 1.007 ± 0.1485, $p = 0.7819$).

Results show a significant upregulation of multiple Nrf2-ARE components at the late symptomatic stage, implying that oxidative stress is upregulated. Therefore, oxidative stress could potentially be driving SG formation during this stage.

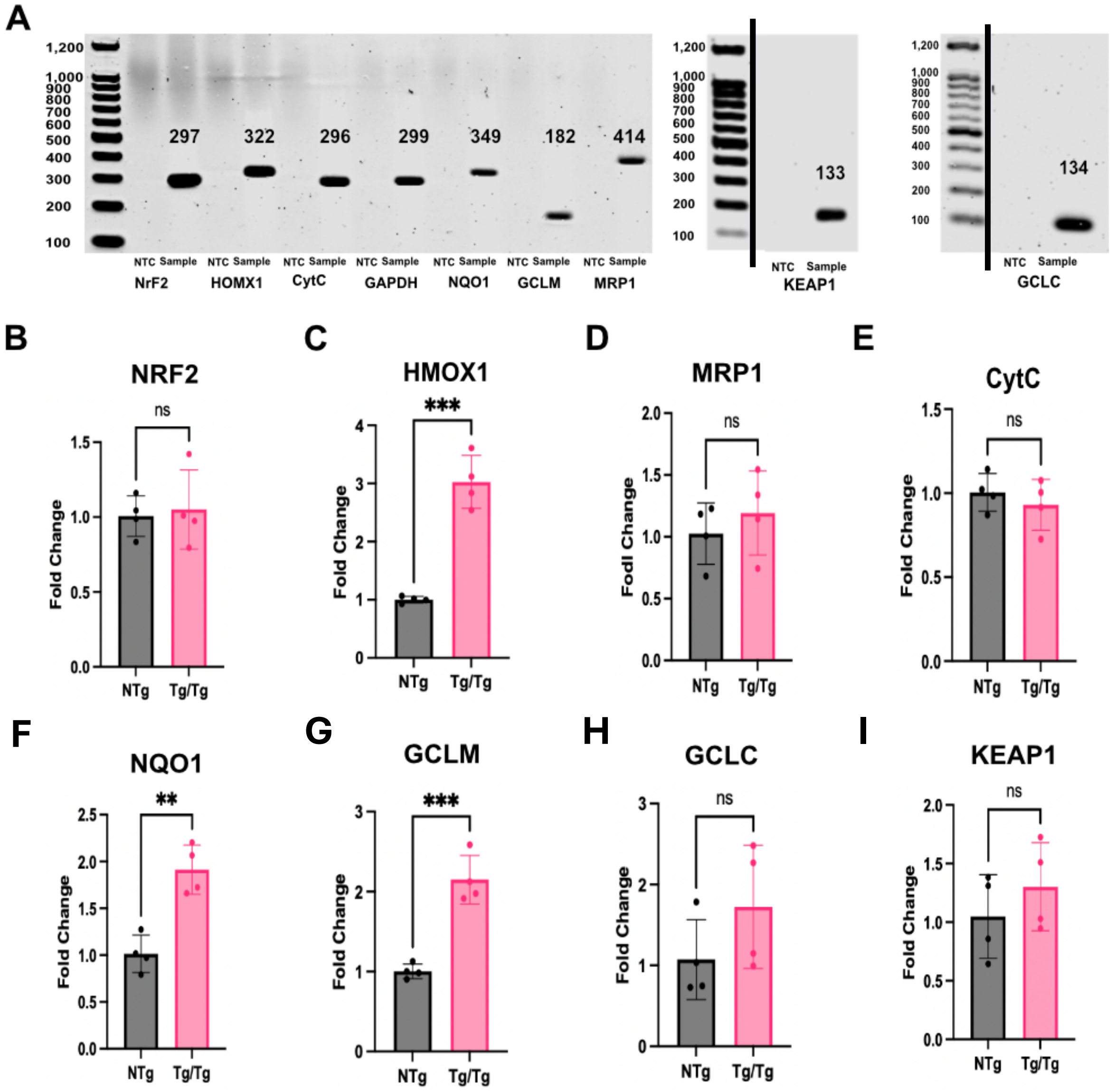

Figure 27: Oxidative stress markers are significantly upregulated at the late symptomatic stage in SPC Tg/Tg mice. Optimised primer pairs targeting CytC, GCLC, GCLM, HMOX1, KEAP1, NQO1, and NrF2 were used to detect changes in the translation in SPC of NTg and Tg/Tg mice using qPCRs.

A) 1.5% agarose gel showing bands Non-Template control (NTC) and NTg sample band for CytC, GCLC, GCLM, HMOX1, KEAP1, MRP1 NQO1, and NrF2 translation in late symptomatic spinal cord tissue. Numbers above bands indicate the correct molecular height for each band. Black lines indicate where the same membrane has been cut to create the example image.

B-I) NrF2, HMOX1, MRP1, CytC, NQO1, GCLM, GCLC, and KEAP1 expression in NTg and Tg/Tg spinal cords at the late symptomatic stage. Results are shown as mean ± SEM, with each point representing protein translation from one mouse. Differences in protein translation for NTg and Tg/Tg mice were analysed with unpaired two-tailed t-tests. n = 4 mice per group. ns = non-significant, **p <0.01, ***p <0.001.

Part 3: Pathological role of SGs in the hTDP43 mouse model

NLRP3 inflammasome activation is present at the late symptomatic stage

As SG formation can have both a protective and harmful role in disease progression, investigating the role SG formation plays in ALS is necessary. Under normal physiological conditions, SG formation plays key roles in inhibiting NLRP3 inflammasome activation and reducing stress in the system through reducing reactive oxygen species (Takahashi et al., 2013a; Yoshioka et al., 2024). Therefore, to attribute a pathological or protective role to the SG formation observed in the hTDP43 mouse model, these factors were analysed.

To investigate whether there were significant changes in NLRP3 inflammasome activation, a previously used primer pair targeting NLRP3 was used to investigate differences at the transcriptome level between NTg and Tg/Tg mice. Primer pair specificity was tested through analysing the amplification and melt curve (Figure 28A). The qPCR protocol was then run with the non-template control and NTg well run on a 1.5% agarose gel to check for contamination (Figure 28B).

Tg/Tg spinal cord showed a significant increase in NLRP3 translation compared to NTg samples (Figure 28C) (NLRP3 SPC Tg/Tg vs NTg: 2.035 ± 0.2095 vs 1.039 ± 0.2095, p = 0.0031). This indicates that despite SG forming in ALS, there is still NLRP3 inflammasome activation.

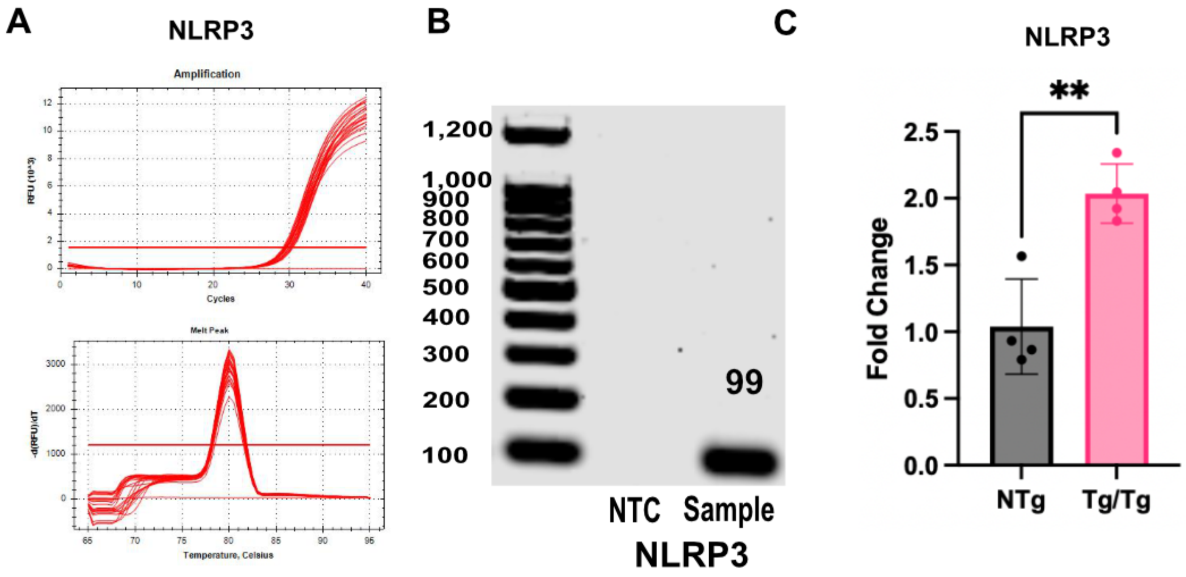

Figure 28: NLRP3 is significantly upregulated at the transcriptome level at the late symptomatic stage in SPC Tg/Tg mice.

A) Amplification and melt curves generated from the qPCR optimisation protocol for NLRP3 primer pair. Amplification curve is the top graphs, with melt curve below. Refer to Figure 11 for further details regarding selection.

B) 1.5% agarose gel showing bands Non-Template control (NTC) and NTg sample band for NRLP3 translation in late symptomatic spinal cord tissue. Numbers above bands indicate the correct molecular height for each band.

C) NLRP3 expression in NTg and Tg/Tg spinal cords at the late symptomatic stage. Results are shown as mean ± SEM, with each point representing NLRP3 translation from one mouse. Differences in NLRP3 translation for NTg and Tg/Tg mice were analysed with unpaired two-tailed t-tests. n = 4 mice per group. **p <0.01.

Reactive Oxygen Species markers are significantly upregulated at the late symptomatic stage

As SG formation also plays a key role in reducing reactive oxygen species, we analyzed whether these were significantly changed in Tg/Tg spinal cord tissue at the late symptomatic stage using qPCR. Primer pairs targeting reactive oxygen species markers: mNOS, mXO, SOD2, and NOX3 were optimised using the previously mentioned protocol (Figure 29A-K). NOX3 primer pairs did not produce reliable amplification curves or melt peaks; therefore, they were deemed unreliable (Figure 29G-K). Similarly, when running mNOS primer pair 2, a nonspecific band was observed, therefore, was not deemed specific (Figure 29K). mXO primer pair 1 and SOD2 primer pair 1 were deemed as specific and consistent across the temperature gradient and thus were used to detect changes in the transcriptome between NTg and Tg/Tg mice.

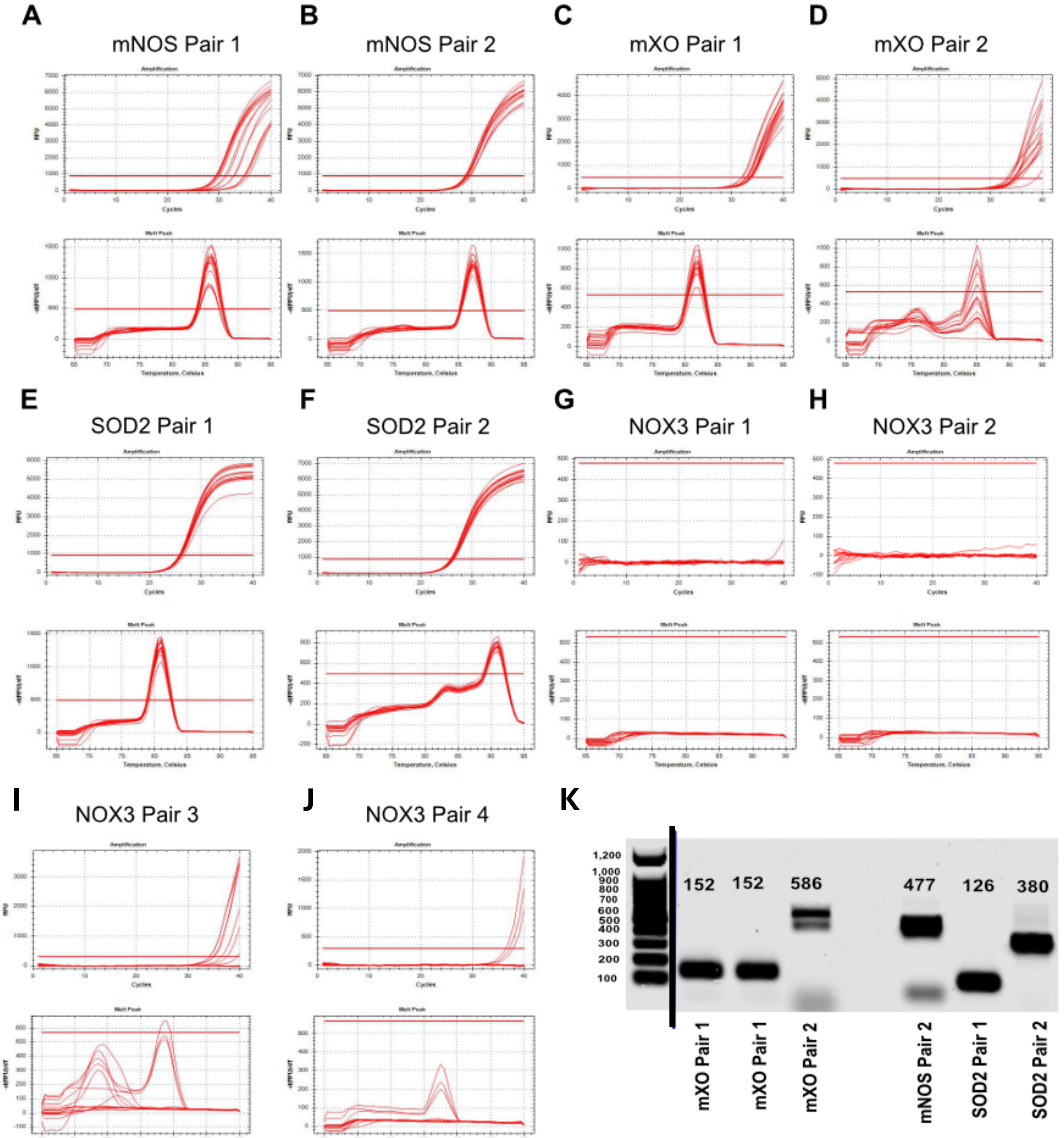

Figure 29: qPCR optimisation for reactive oxygen species marker primer pairs. Reactive oxygen species primer pairs were designed to target mNOS, mXO, SOD2, and NOX3 to determine whether there were changes in the transcriptome level of reactive oxygen species markers. Primer pairs were optimised using a temperature gradient spanning 50-63°C and a singular NTg sample (for further details, refer to methods section).

A-I) Amplification and melt curves generated from the qPCR optimisation protocol for each pair. Amplification curves are the top graphs, with melt curves below. Refer to Figure 11 for further details regarding selection.

K) Selected Primer pairs were then run on a 1.5% agarose gel to confirm product specificity. Numbers indicate the predicted height of each product. Black lines indicate where the same gel has been cut to create the example image.

]

Optimised primer pairs targeting ROS markers were then used to detect changes between Ntg and Tg/Tg spinal cord tissue at the late symptomatic disease stage at the transcriptome level. Samples were run as previously described. No contamination was evident in any non-template controls, and bands were seen to be specific for each primer pair (Figure 30A); therefore, quantification of results was able to proceed.

Tg/Tg spinal cords showed a significant upregulation in mXO translation compared to NTg controls (Figure 30B) (mXO SPC Tg/Tg vs NTg: 4.417 ± 0.5736 vs 1.021 ± 0.5736, p = 0.0010). Tg/Tg spinal cords showed no difference in SOD2 translation compared to NTg controls (Figure 30C) (SOD2 SPC Tg/Tg vs NTg: 1.308 ± 0.3287 vs 1.098 ± 0.3287, p = 0.5469). These results indicate that there is a significant upregulation of mXO, a reactive oxygen species, at the late symptomatic stage in Tg/Tg spinal cord tissue despite upregulation of SG formation being present.

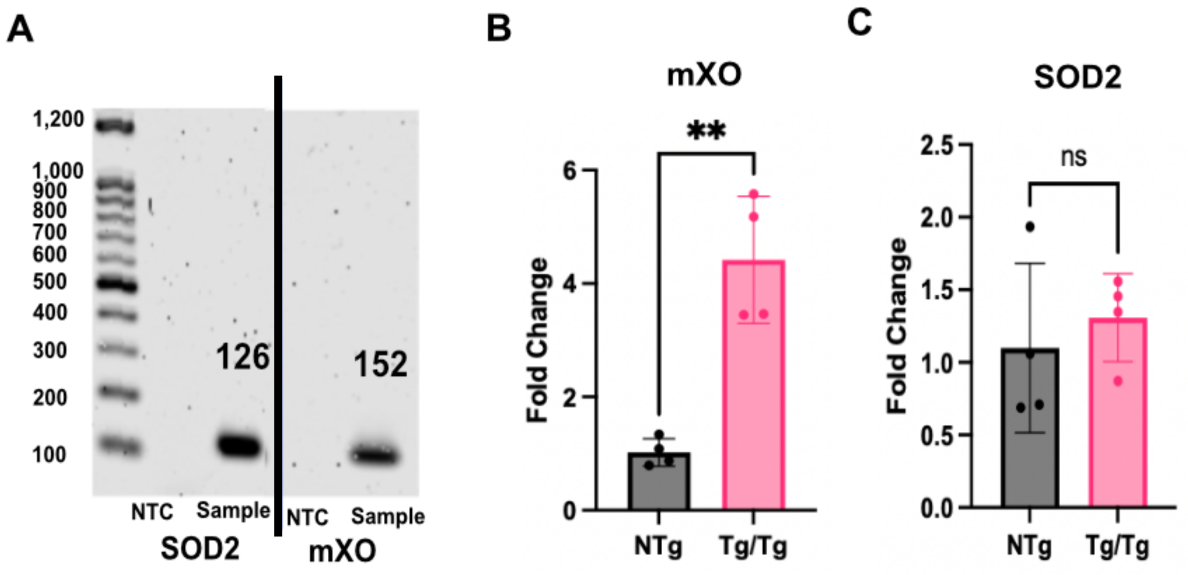

Figure 30: Reactive oxygen species markers are significantly upregulated at the late symptomatic stage in SPC Tg/Tg mice. Primer pairs targeting mXO and SOD2 were used to detect changes in the translation in SPC of NTg and Tg/Tg mice using qPCRs.

A) 1.5% agarose gel showing bands Non-Template control (NTC) and NTg sample band for mXO and SOD2 translation in late symptomatic spinal cord tissue. Numbers above bands indicate the correct molecular height for each band. Black lines indicate where the same membrane has been cut to create the example image.

B-D) mXO1 and SOD2 expression in NTg and Tg/Tg spinal cords at the late symptomatic stage. Results are shown as mean ± SEM, with each point representing protein translation from one mouse. Differences in translation for NTg and Tg/Tg mice were analysed with unpaired two-tailed t-tests. n = 4 mice per group. **p <0.01, ns = non-significant

Part 4: Changes in autophagy degradation in the hTDP43 mouse model

Autophagy markers are unaltered or decreased at the late symptomatic stage

As there is both a significant upregulation of NLRP3 and reactive oxygen species markers at the late symptomatic disease stage, this implies that despite SG forming, they are not performing their normal protective functions. Autophagy regulates SG homeostasis and is responsible for SG degradation (Buchan et al., 2013; Ryan & Rubinsztein, 2024b). Therefore, as SG formation appears to be dysfunctional at the late symptomatic stage, we wanted to examine whether there was evidence of autophagy degradation, the pathway responsible for SG degradation.

Quantitative western blotting was used to detect protein level changes in several autophagy markers in the brain and spinal cord NTg and Tg/Tg tissue: ULK1, P62, Beclin, LC3B at the late symptomatic stage. Bands for autophagy markers in both the brain and spinal cord appeared at the reported height for each antigen-specific band (Figure 31A, C).

In spinal cord tissue, autophagy marker levels were unchanged in Tg/Tg mice compared to NTg controls (Figure 31B) (ULK1 SPC Tg/Tg vs NTg: 0.4411 ± 0.2379 vs 1.000 ± 0.2379, p = 0.0656) (P62 SPC Tg/Tg vs NTg: 0.8559 ± 0.3005 vs 1.000 ± 0.3005, p = 0.6517) (Beclin SPC Tg/Tg vs NTg: 0.8288 ± 0.09235 vs 1.000 ± 0.09235, p = 0.1229) (LC3B II/I SPC Tg/Tg vs NTg: 0.9792 ± 0.1991 vs 1.035 ± 0.1991, p = 0.7887).

In brain tissue, a significant decrease in LC3B II/I protein level was observed in Tg/Tg mice compared to NTg controls (Figure 31D) (L3CB II/I BR Tg/Tg vs NTg: 0.6410 ± 0.1065 vs 1.001 ± 0.1065, p = 0.0096). However, no change was observed in ULK1, P62, and Beclin protein level in Tg/Tg brain tissue compared to NTg controls (ULK1 BR Tg/Tg vs NTg: 1.313 ± 0.2741 vs 1.000 ± 0.2741, p = 0.2864) (P62 BR Tg/Tg vs NTg: 0.8034 ± 0.1944 vs 1.000 ± 0.1944, p = 0.3416) (Beclin BR Tg/Tg vs NTg: 0.9139 ± 0.1005 vs 1.000 ± 0.1005, p = 0.4169).

Therefore, with our current sample sizes, these results indicate that at the late symptomatic stage, autophagy markers are largely unchanged.

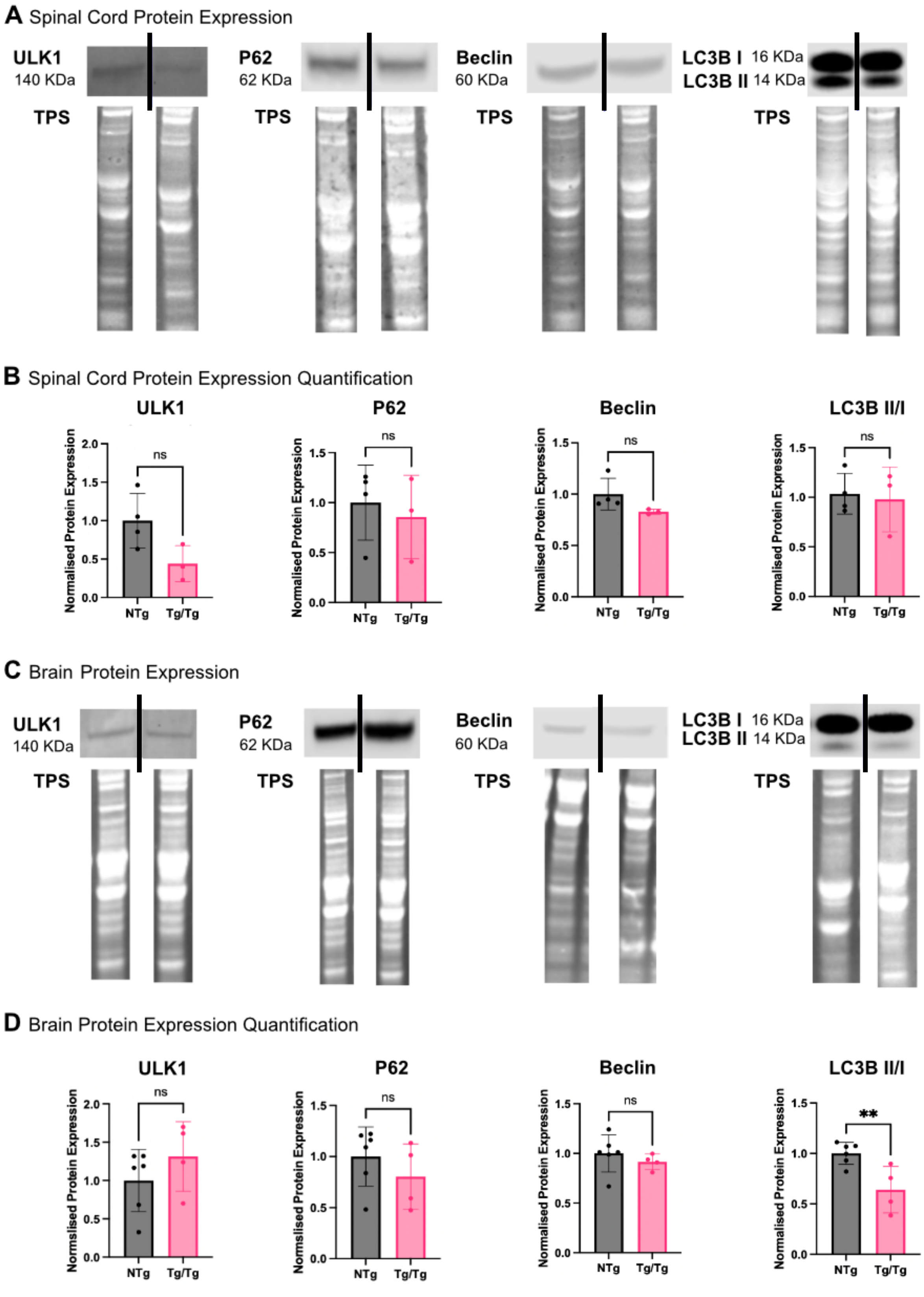

Figure 31: Autophagy markers are unaltered at the late symptomatic in Tg/Tg mice.

A, C) Western blot images showing representative bands for ULK1, P62, Beclin, and LC3B expression in NTg and Tg/Tg in the brain and spinal cord at P19. Black lines indicate where the same membrane has been cut to create the example image.

B) Amount of ULK1, P62, Beclin, and LC3B expression at the late symptomatic stage in the spinal cord. Results are shown as mean ± SEM, with each point representing protein expression from one mouse. Differences in protein expression for NTg and Tg/Tg mice were analysed with unpaired two-tailed t-tests. n = 3-4 mice per group. ns= non-significant.

D) Amount of ULK1, P62, Beclin, and LC3B expression at the late symptomatic stage in brain tissue. Results are shown as mean ± SEM, with each point representing protein expression from one mouse. Differences in protein expression for NTg and Tg/Tg mice were analysed with unpaired two-tailed t-tests. n = 3-6 mice per group. ns= non-significant, p** <0.01.

Autophagy is significantly decreased at clinical end-stage

Autophagy degradation is a major mechanism of pathological SG disassembly. As SG formation is only significantly upregulated at the late symptomatic stage in the hTDP43 mouse model, it is likely that the autophagy response, therefore, occurs at later time points. Therefore, we sought to determine whether there was evidence of SG degradation by autophagy at the clinical endstage (P22-23).

Changes in autophagy levels were analysed in brain tissue of NTg and Tg/Tg mice using the previously mentioned autophagy markers (ULK1, p62, Beclin, and LC3B) through quantitative western blotting. ULK1 and Beclin protein levels were significantly decreased at endstage Tg/Tg brain tissue compared to NTg controls (Figure 32B) (ULK1 BR Tg/Tg vs NTg: 0.4685 ± 0.1690 vs 1.000 ± 0.1690, p = 0.0347) (Beclin BR Tg/Tg vs NTg: 0.7325 ± 0.03547 vs 1.000 ± 0.03547, p = 0.0017). p62 and LC3B II/I protein levels, however, were unchanged in the brain of Tg/Tg mice compared to NTg mice (Figure 32B) (P62 BR Tg/Tg vs NTg: 0.8319 ± 0.07502 vs 1.000 ± 0.07502, p = 0.0885) (LC3B II/I BR Tg/Tg vs NTg: 1.001 ± 0.2068 vs 1.000 ± 0.2068, p = 0.9951). Therefore, there are multiple autophagy markers showing a significant decrease in Tg/Tg endstage, indicating an impairment in autophagy degradation.

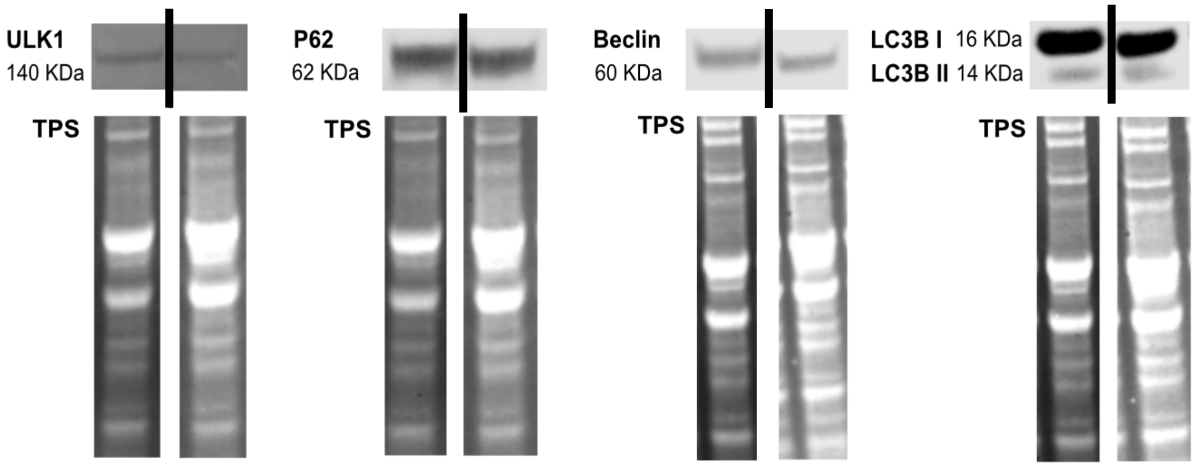

A Brain Protein Expression

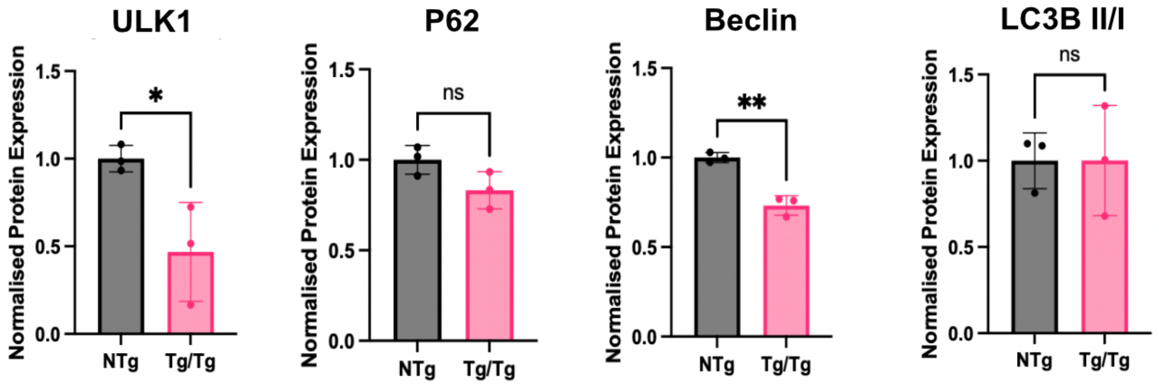

B Brain Protein Expression Quantification

Figure 32: Autophagy markers are significantly decreased at endstage (P22-23) in Tg/Tg mice.

A) Western blot images showing representative bands for ULK1, P62, Beclin, and LC3B expression in NTg and Tg/Tg in brain tissue at endstage. Black lines indicate where the same membrane has been cut to create the example image.

B) Amount of ULK1, P62, Beclin, and LC3B expression at endstage in brain tissue. Results are shown as mean ± SEM, with each point representing protein expression from one mouse. Differences in protein expression for NTg and Tg/Tg mice were analysed with unpaired two-tailed t-tests. n = 3 mice per group. ns= non-significant, $p^* < 0.05$, $p^{**} < 0.01$.

Part 5: Rescuing SG dynamics in the hTDP43 mouse model

Terazosin Treatment elicited a differential response to SG formation in late symptomatic Tg/Tg mice

As SG formation may play a pathological role in disease progression, we finally wanted to investigate whether treatments which have neuroprotective effects in ALS also elicit changes in SGs. Terazosin, a drug approved to treat hypertension, has recently shown beneficial effects in ALS. Targeting energy metabolism through activation of PGK1, terazosin has shown improvement in multiple ALS models, improving motor phenotypes, increasing survival, and improving MN number (Chaytow et al., 2022). Terazosin has also been shown to restore SG formation *in vitro* ALS models, including TDP43 M337V mouse embryonic stem cell-derived motor neurons (Chaytow et al., 2022). Therefore, we wanted to explore whether terazosin treatment could restore SG dynamics in an ALS in vivo model.

Prior to this study performed by other members of the lab, NTg and Tg/Tg mice were treated with 100 ug/kg of saline or terazosin, administered daily from day of birth via an intraperitoneal injection (Chaytow et al., 2022). I performed Immunohistochemistry on saline-treated and terazosin-treated late symptomatic Tg/Tg and NTg cryosectioned lumbar spinal cord sections using DAPI, ChAT, and G3BP2 (Figure 33A, Figure 34) to detect whether changes in SG dynamics were influenced by terazosin treatment.

A significant upregulation in SG formation was observed in saline-treated Tg/Tg spinal cords compared to saline-treated NTg spinal cords (Figure 33B), aligning with previous results found (Figure 16) (NTg Saline vs Tg/Tg Saline: 0.05870 ± 0.05569 vs 0.3024 ± 0.03082, P = 0.0305). Overall, terazosin-treated Tg/Tg spinal cords showed no significant difference in G3BP2/ChAT positive cells compared to NTg controls and Tg/Tg saline-treated spinal cords (Figure 33B) (NTg saline vs Tg /Tg terazosin: 0.05870 ± 0.05569 vs 0.2006 ± 0.06314, p = 0.1983) (Tg/Tg Saline vs Tg/Tg Terazosin: 0.3024 ± 0.03082 vs 0.2006 ± 0.06314, p = 0.4064). However, Tg/Tg terazosin-treated spinal cords appeared to have two different responses to treatment: either no difference in SG formation or a significant decrease in SG formation compared to saline-treated Tg/Tg spinal (Figure 33A, B), indicating a possible bimodal response to treatment.

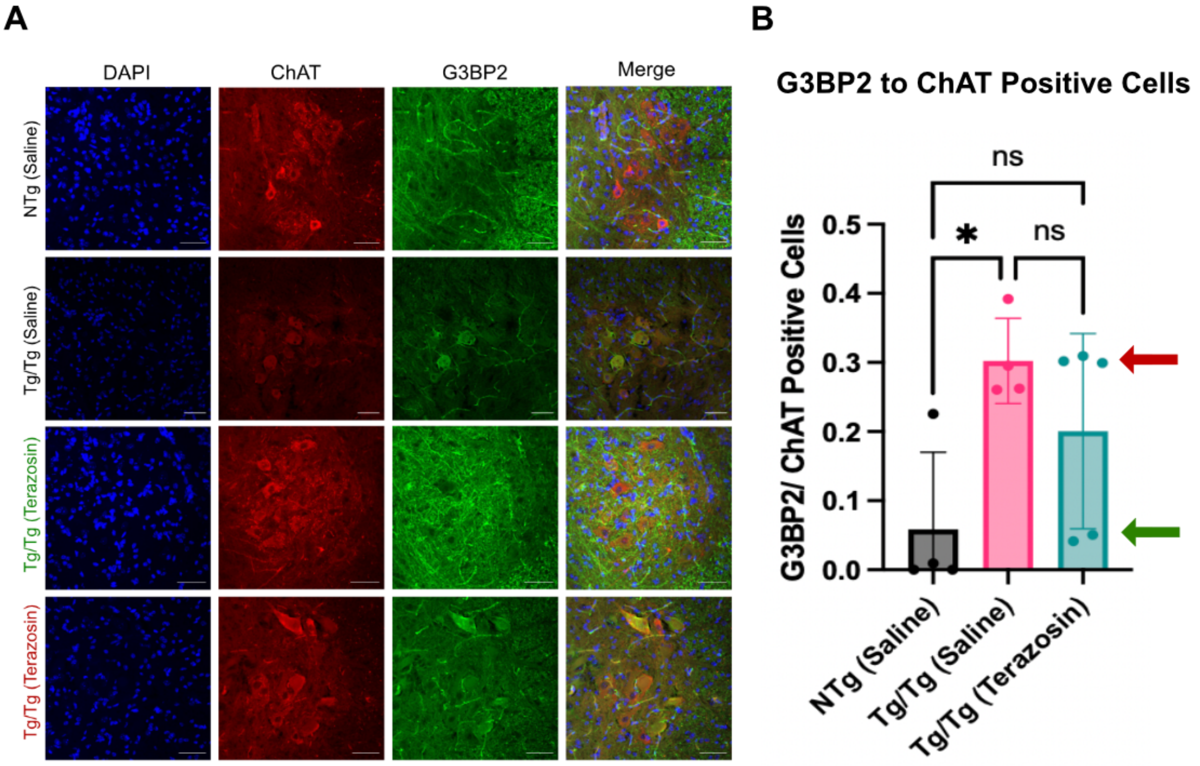

Figure 33: Terazosin treatment causes either a downregulation or no change in SG formation in Tg/Tg mice at the late symptomatic stage.

A) Representative confocal micrographs of spinal cord sections stained with DAPI (blue), ChAT (red), G3BP2 (Green) for NTg and Tg/Tg mice at 20X. Green text shows representative images of Tg/Tg stained spinal cords with significantly decreased SG formation compared to saline treated Tg/Tg spinal cords. Red text shows representative images of Tg/Tg stained spinal cords with unchanged SG formation compared to saline-treated Tg/Tg spinal cords. Scale bar 50 µm.

B) Results are shown as mean ± SEM, with each data point representing the average G3BP2 to ChAT positive cells per mouse. A bimodal response was observed in terazosin-treated Tg/Tg spinal cords. Terazosin treatment either showed no difference in SG dynamics (red arrow) or a significant change in SG dynamics compared to saline-treated Tg/Tg mice (green arrow). A one-way ANOVA with post-hoc Tukey's multiple comparisons was performed to determine differences between groups. n = 4-5 mice per genotype, n= 8-10 SPC per mouse. *$p<0.05$, ns = non-significant.

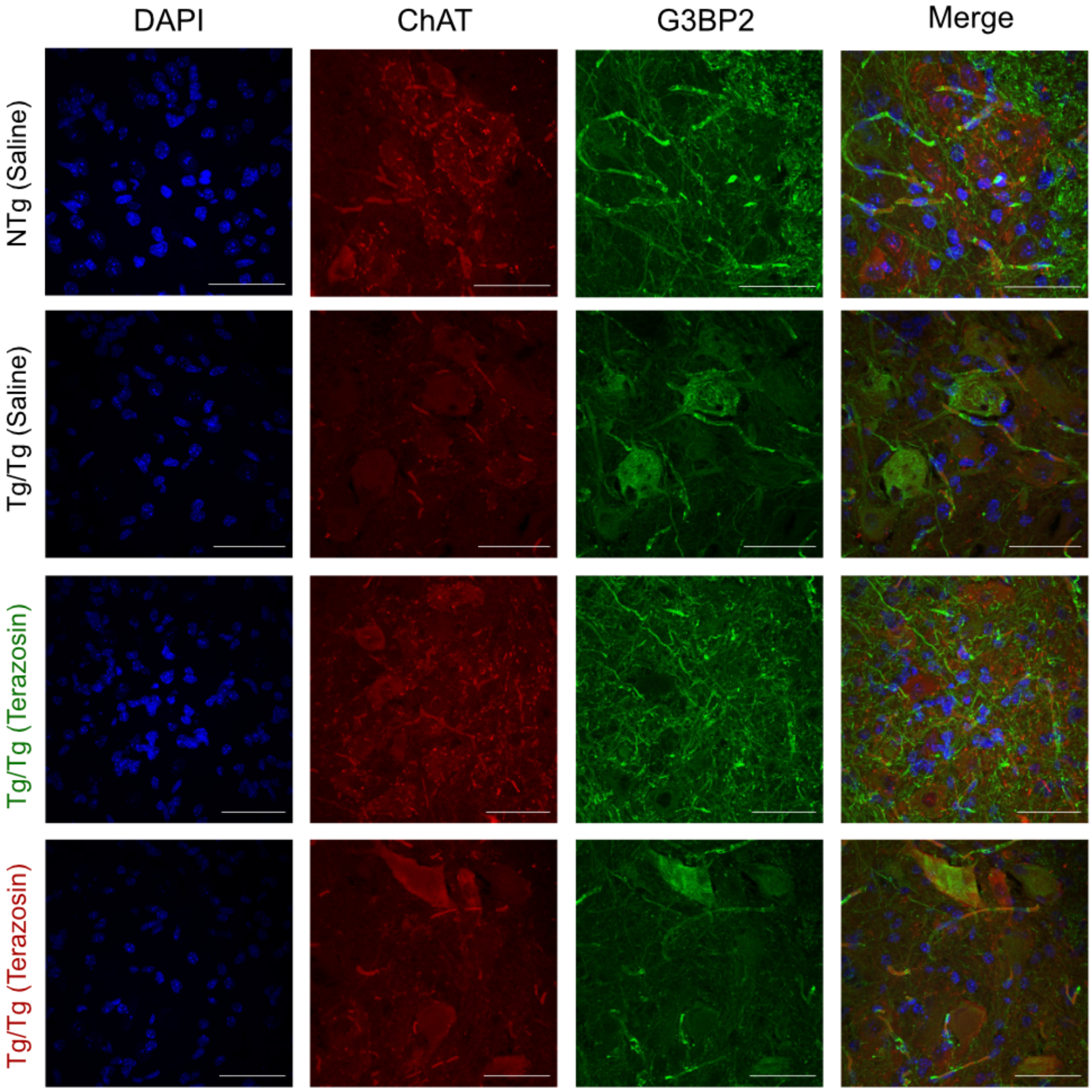

Figure 34: Representative confocal micrographs 60X images of late symptomatic NTg and Tg/Tg SPC following Terazosin treatment. Representative fluorescent images of spinal cord sections stained with DAPI (blue), ChAT (red), G3BP2 (Green) for NTg and Tg/Tg mice. Green text shows representative images of Tg/Tg stained spinal cords with significantly decreased SG formation compared to saline treated Tg/Tg spinal cords. Red text shows representative images of Tg/Tg stained spinal cords with unchanged SG formation compared to saline-treated Tg/Tg spinal cords. Scale bar 50 μm.

For quantification results, refer to Figure 33.

Discussion

Our study shows for the first time a significant endogenous increase in SG formation with increases in SG protein levels and SG transcription levels evident in the *in vivo* hTDP43 ALS mouse model without the use of an external stressor. SGs were also seen to colocalize with the ALS-associated protein, TDP43, at the late symptomatic disease stage, reflecting findings from previous studies. These changes in SG dynamics in the hTDP43 model were found to be specific to the late symptomatic timepoint, the time point at which TDP43 mislocalization occurs. Additionally, significant upregulation in markers for chronic cellular stress pathways, oxidative stress, and neuroinflammation were observed, implying that they could be involved in SG upregulation. Key factors that are regulated by protective SG, such as ROS production and NLRP3 inflammasome activation, were also upregulated in the hTDP43 mouse model, suggesting a pathological role for SG formation. Autophagy, the mechanism responsible for SG degradation, seemed to be unaffected in the hTDP43 mouse model. Targeting SGs using terazosin showed a bimodal response on SG dynamics: either showing a rescue of dynamics to levels observed in NTg spinal cords or no change in SG dynamics compared to saline-treated Tg/Tg spinal cords.

SG formation in ALS

Understanding the role stress granules play in ALS pathology is becoming an increasingly relevant topic, with mutations in SG proteins, TIA1 and HuR, linked to ALS pathology. The role that SGs play in ALS remains debated in the field, with both an increase and decrease noted in different ALS models (Besnard-Guérin, 2020; Fernandes et al., 2018). However, changes in SG composition and morphology in FUS and C9ORF72 mutant ALS models have been noted, indicating a shift towards a pathological role (An et al., 2022; Marmor-Kollet et al., 2020). Aligning with this, direct targeting of SG has elicited beneficial outcomes in ALS models (Becker et al., 2017; Elden et al., 2010; Liu-Yesucevitz et al., 2010a).

The study of SGs in ALS has, however, largely been limited to an *in vitro* setting with the use of external stressors. Little work has been conducted in an *in vivo* setting with only two studies performed. These two studies, however, also made use of an external stressor and observed significant decreases in SG formation in SOD1, FUS, and TDP43 mutant ALS mouse models (Dubinski et al., 2023; X. Zhang et al., 2020). SGs are highly dynamic and are seen to change in morphology and composition dependent on the external stressor utilised therefore the question still remains regarding whether changes seen previously using *in vitro* and *in vivo* models could in some part be due to the overstimulation of these cells by the stressor itself. In stress-preconditioned human neurons and mouse hippocampal neurons, they fail to maintain phosphorylated eIF2 alpha levels and have decreased SG formation upon a second induction of stress (Shelkovnikova et al., 2017). As cellular stress is a central feature of ALS, the additional stimulation of stress by an external stressor could, therefore, be the cause of changes in SG dynamics and not intrinsic pathology. Therefore to mitigate these issues, SG formation was visualised without the use of an external stressor.

The hTDP43 mouse model is an TDP43 overexpression model. Human TARDBP is overexpressed under the neuron-specific promoter Thy1, leading to motor neuron death, muscle wasting, TDP43 mislocalisation, and eventual paralysis (Alhindi et al., 2023; Wils et al., 2010). As the majority of ALS patients do not have mutations in TDP43 but still have TDP43 pathology, an overexpression model mirrors the clinical phenotype of patients more accurately. The onset of pathology in this model occurs at postnatal day 15 (early symptomatic), with motor neuron death and neuromuscular junction denervation in hindlimb muscles seen at this time point (Alhindi et al., 2023). The pathology then progresses rapidly, causing TDP43 mislocalisation and hindlimb muscle weakness at postnatal day 19 (late symptomatic), leading to eventual hindlimb paralysis.

TDP43 expression has been seen to modulate core SG proteins, TIA1 and G3BP1/2, affecting both the assembly and maintenance of SGs (McDonald et al., 2011). Our results show a significant upregulation in SG formation in spinal motor neurons in Tg/Tg mice at the late symptomatic stage (Figure 16). In conjunction with this, significant upregulation of SG formation markers was observed in both brain and spinal cord tissue at both the protein level and the transcription level (Figures 16, 19, 22). Taken together, these results reveal a significant upregulation of SG formation in the hTDP43 mouse model during pathogenesis (Figure 35). Our result do align with previous findings in human patient spinal cords and previous in vitro work in which HEK 293 cells were transfected with TDP43 mutations (A315T, G294A, Q331K, and Q343R) stimulated with chronic arsenite stress, showing a significant increase in SG formation (Liu-Yesucevitz et al., 2010a; F. Mori et al., 2024; Volkening et al., 2009).

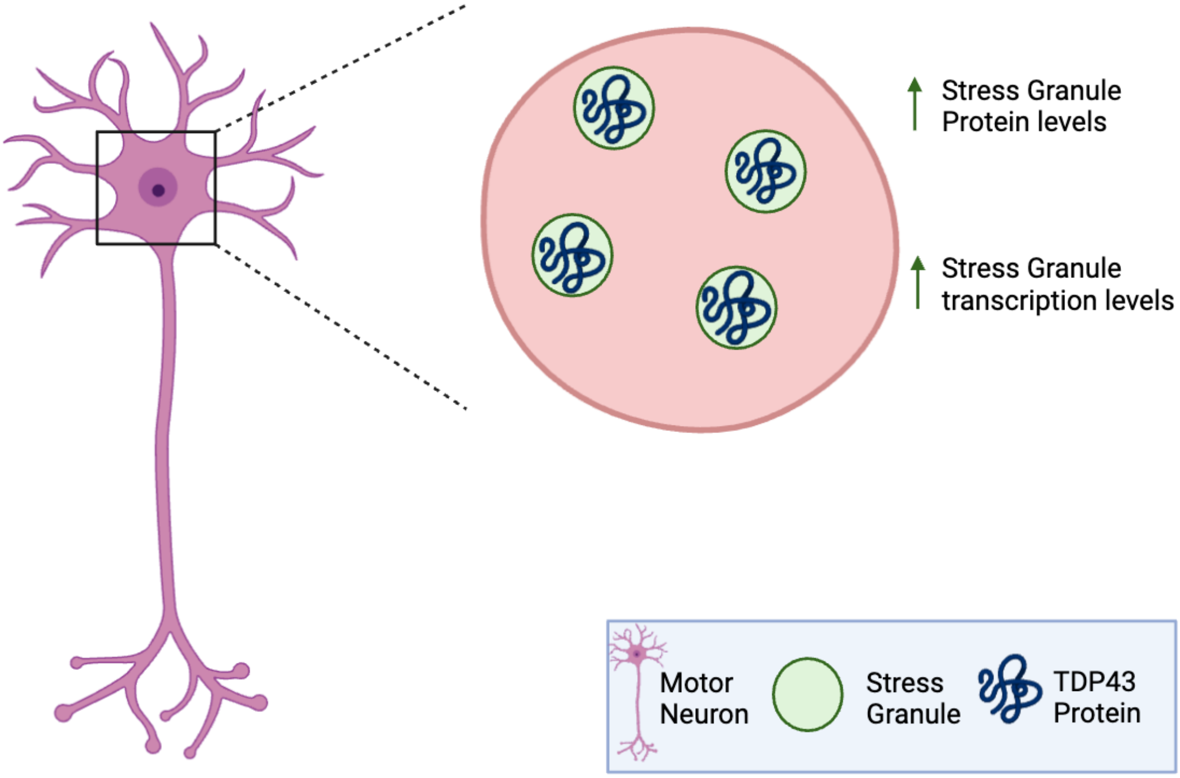

Figure 35: Stress Granule formation in the hTDP43 mouse model. Results show that SGs are upregulated in Tg/Tg spinal motor neurons, with upregulations in stress granule protein level and transcription being evident in spinal cord tissue. These SGs additionally colocalised with TDP43 in spinal motor neurons. Created using BioRender.

No previous investigation into SG dynamics has been conducted on ALS animal models in vivo without the use of an external stressor. Therefore, this represents a novel finding in the field. As an external stressor was not used, these results better represent the physiological conditions experienced during ALS more accurately than models in which an external stressor was applied.

Changes in SGs have been suggested to be present in the early stages of ALS pathology. In other ALS animal models, such as the TDP43^{M337V} mutant model, changes in SG dynamics were seen at the presymptomatic disease stage upon the induction of hyperthermia treatment (Dubinski et al., 2023). However, interestingly, in our model, no changes in SG formation were observed at either the transcriptome or protein level at the early symptomatic stage (Figure 24). In ALS, SGs have been hypothesised to play a role in seeding for protein aggregates and leading to the formation of protein aggregates (Cui et al., 2024). At the late symptomatic timepoint, when TDP43 mislocalisation occurs, we observed significant changes in SG formation at the protein and transcription level accompanied by colocalisation between SGs and TDP43 in Tg/Tg spinal cord motor neurons (Figure 16, 19, 22, 23). Colocalisation has been previously found in spinal cord sections of both ALS models and patient post-mortem tissue, supporting this result (F. Mori et al., 2024). As protein aggregation is not present at the early symptomatic stage, this, therefore, might attribute a specific role for SGs in TDP43 mislocalisation and with

SGs playing roles in late disease pathogenesis. This would imply that changes in SGs might not be a driving factor in pathogenesis in the hTDP43 mouse model but a secondary pathological mechanism. It is, therefore, probable that other pathological triggers might be causing SG dysregulation within ALS, for example, TDP43. Previous literature has hypothesised that changes in SGs could be inducing TDP43 pathology; however, the opposite process could instead be occurring. Changes in TDP43 during pathogenesis could instead be causing altered functioning in SGs, leading to further pathology. Under cellular stress, SGs uptake many factors to prevent cellular damage, including TDP43 (Liu-Yesucevitz et al., 2010). Therefore, during ALS, the induction of chronic cellular stress could be causing the upregulation of SGs as a protective mechanism, but upon the association of SGs with TDP43, their function and composition could be altered, leading to deleterious functioning and possibly further contributing to pathology. This would further explain why colocalisation between TDP43 and SGs was only observed in a proportion of spinal motor neurons in the hTDP43 mouse model (Figure 23), as instead of SGs being responsible for TDP43 aggregation, TDP43 could be responsible for SG dysfunction.

This theory has, however, not been previously investigated within the ALS field. Therefore, to understand the timeline of SG changes in ALS in relation to pathology and to determine whether SGs play a primary or secondary role in pathogenesis, further work would need to be conducted. A timelapse analysis on SG formation and TDP43 aggregate formation could be performed in ALS pathogenesis using *in vitro* models. A timelapse analysis is not possible in an in vivo model such as the hTDP43 model, as live cells could need to be continuously recorded and observed to determine their interactions. Therefore, to study this further, primary cells could be cultured from the hTDP43 mouse model and differentiated into motor neurons, and changes in SG dynamics in relation to TDP43 pathology could be evaluated (C. Zhao, 2023). An external stressor, however, would need to be used to stimulate SG formation in this model. As oxidative stress is seen to be upregulated in the hTDP43 mouse model and can stimulate SG formation in vitro models, this should be preferentially used (Figure 27) (L. Chen & Liu, 2017). As the use of this external stressor might alter the physiological response of the cells, confirmation of the result should then be conducted in an *in vivo* setting. SG formation could be inhibited in the hTDP43 mouse model using the viral nsP3 peptide or cisplatin compound, and changes in both TDP43 mislocalisaton could be analysed (X. Lu et al., 2021; Pietras et al., 2022). Based on this study, it is probable that SGs do not play a primary role in pathogenesis and are, instead, alerted by TDP43-inducing changes in SG dynamics. However, to better understand what role they could be playing in ALS pathology, disease progression could be analysed in the hTDP43 mouse model with SG inhibition. If these mice develop a more severe phenotype, then a pathological role could be attributed to SG formation. These experiments will, therefore, allow us to attribute a specific role to SG formation in regard to TDP43 and further elucidate the role of SG formation as a pathological feature in ALS.

Pathological Role of SG in ALS

Despite the debate regarding SGs playing a primary or secondary role in ALS pathogenesis, they have been attributed to play pathological roles (refer to introduction for further details). Similarly, our findings show that markers of ROS and NLRP3 inflammasome activation are upregulated on the transcription level in Tg/Tg spinal cord tissue at the late symptomatic disease stage (Figures 28, 30). Past experiments indicate that ROS and NLRP3 inflammasome activation are present in ALS, thus confirming the results seen in this study (Beal et al., 1997; Johann et al., 2015; Xiao et al., 2018). At the late symptomatic stage, we observed a significant increase in SG formation, as ROS and NLRP3 inflammasome activation are inhibited by the formation of protective SGs; this, therefore, may imply a pathological role for the formation of SGs in the hTDP43 mouse model. However, as ALS is a complex disease with the dysregulation of multiple pathways implicated, these factors may, therefore, be a result of other dysregulations not linked to SGs. To further investigate this, a more detailed analysis of SG factors should be conducted. SGs regulate ROS activity through regulating UPS10 activity, with G3BP1 inhibiting UPS10, leading to an increase in ROS (Takahashi et al., 2013). SGs additionally regulate NLRP3 inflammasome activation by sequestering DDX3X, inhibiting inflammasome activation (Yoshioka et al., 2024). Therefore, analysis of both UPS10 and DDX3X activity should be conducted in the hTDP43 mouse model. If an increase in UPS10 and DDX3X activity is observed, this would implicate SGs as playing a direct pathological role in disease pathogenesis.

Chronic Cellular Stress

All previous studies investigating SG formation in ALS utilized an external stressor, such as oxidative stress, sorbitol, arsenite, hypothermia, and oxalate (Colombrita et al., 2009; Dewey et al., 2011; Dubinski et al., 2023; Ratti et al., 2020). It is therefore, unknown what chronic cellular pathways induce SG formation endogenously during ALS. Our results show that there are significant increases in neuroinflammation and oxidative stress in the late symptomatic stage of the hTDP43 mouse model (Figures 25, 27). At this stage, there are also significant increases in SG formation, therefore implying that neuroinflammation and oxidative stress could be causing SG formation in the hTDP43 mouse model. Previous *in vitro* work has confirmed that oxidative stress causes SG formation, and neuroinflammation activation contributes to SG formation (L. Chen & Liu, 2017; Herman et al., 2019). It is probable that the activation of both mechanisms is contributing to SG formation in the hTDP43 mouse model. However, direct links between neuroinflammation, oxidative stress, and SG formation have not been established in the hTDP43 mouse model. Additionally, multiple chronic cellular mechanisms are activated during ALS, with multiple mechanisms contributing to the induction of reactive oxygen species (for further details, refer to introduction); therefore, it is probable that more pathological mechanisms are also contributing to SG formation in the hTDP43 mouse model.

To therefore establish a direct link between the induction of chronic cellular stress mechanisms and SG formation further work would have to be conducted. To directly attribute neuroinflammation and oxidative stress in SG formation, these factors could be inhibited. Zonisamide, an anti-inflammatory agent, has been shown to act on neuroinflammatory glial cells, leading to neuroinflammation suppression in mouse models of Parkinson's disease (Yokoyama et al., 2010). Therefore, in the hTDP43, neuroinflammation could be inhibited using Zonisamide treatment, and SG formation could then be analysed. Similarly, Edaravone, a free reactive oxygen species scavenger, could be used to reduce oxidative stress in the hTDP43, and SG formation could, in turn, be analysed (Ashok et al., 2022). As these drugs, however, might affect more than their intended target, confirmation could then be performed using CRISPR-Cas knockout hTDP43 mouse models (Gurumurthy et al., 2019). In wildtype mice, CRISPR-Cas knockout of key oxidative stress and neuroinflammation factors such as NADPH oxidase 4 and colony-stimulating factor 1 receptor could be performed (B.-Y. Ding et al., 2022; Jackson et al., 2020). These mice could then be crossed with the hTDP43 mouse model, and SG formation could be analysed. These experiments would thus confirm a specific role for neuroinflammation and oxidative stress in SG formation. Due to evidence from previous *in vitro* studies, it is probable that both mechanisms do contribute to SG formation; however, the induction of SG formation in an *in vivo* setting is still unclear. Therefore, this will further clarify how SG formation is elicited in ALS pathology. Additionally, investigations into other chronic cellular stress mechanisms could further be conducted, such as endoplasmic reticulum stress. Analysis of pathological mechanisms and how they link to SG formation will enable a deeper understanding regarding the mechanisms that are crucial to cause SG formation in ALS, which is currently unknown. This, in turn, will aid further research where only stressors that directly cause SG formation could then be used for further research, as they would present the morphological conditions more appropriately. Additionally, this analysis might also point towards SG formation being a key feature in multiple pathological mechanisms in ALS and thus highlight it as a potential therapeutic target for further investigation.

Autophagy

In conjunction with the theory that SGs play a pathological role in ALS, decreases in SG clearance pathways have been noted in ALS. In ALS, autophagy has been reported to be decreased with the activation of mTOR (an inhibitor of autophagy) and mutations in autophagy leading to ALS pathology (Amin et al., 2020; Granatiero et al., 2021; C. Huang et al., 2020). Autophagy is a common degradation in the pathway responsible for the clearance of protein aggregates and damaged cells (Ramesh & Pandey, 2017). This pathway has also been linked to the clearance of SGs, implying that alterations in this pathway may be contributing to the persistence of SGs in ALS. Our preliminary results show that the LC3B autophagy marker is significantly decreased at the late symptomatic stage (Figure 31). As this was the only marker to significantly change overall, our results indicate that there is no significant change in autophagy markers at the late symptomatic stage (Figure 31). These results do not align with previous results in the field, with multiple previous investigations showing a decrease in autophagy (Chua et al., 2021; Vicencio et al., 2020).

The reason for this misalignment could be due to the underpowered nature of our results; therefore, to make a definitive conclusion in regard to autophagy at the late symptomatic stage, sample size would need to be increased. If these results do, however, hold with an increased sample size, this would indicate that despite an increase in SG formation being observed, no autophagy clearance is occurring. As autophagy has been attributed to play roles in SG clearance, this indicates that clearance of SGs is not occurring in the hTDP43 mouse model at the late symptomatic stage. However, as SGs do only appear at the late symptomatic stage, it is likely that changes in the autophagy pathway may be instead seen at later disease stages in repones.

At the clinical endstage, we do see significant decreases in autophagy markers in Tg/Tg brain tissue compared to NTg controls (Figure 32). Therefore, we see a significant upregulation of SGs, which should be cleared by autophagy, but instead of autophagy being upregulated, we see a significant decrease, showing that there is a dysregulation of both SGs and autophagy clearance in ALS. This, therefore, could indicate that SG dynamics are being altered in ALS pathology, and instead of being targeted for clearance, they are instead allowed to persist and evade degradation. In human living cells with ALS-associated dipeptides expressed, SG dynamics were altered with the depletion of SG clearance factors seen (Marmor-Kollet et al., 2020), indicating that in ALS, SGs could become persistent by modulating their composition to avoid degradation. However, another possibility could be that these SGs are playing protective roles and, therefore, are not being targeted by autophagy. Therefore, to gain a better understanding of the role of autophagy degradation on SGs, further analysis should be conducted. To determine whether changes in SG morphology are influencing SG degradation, primary cells could be cultured from the hTDP43 mouse model, and SG morphology and composition could then be analysed under conditions of oxidative stress compared to wild-type cells. Previous literature indicates that ALS SGs do have altered autophagy factors. As autophagy degradation additionally acts on many pathways to support this result, further immunolabelling of SG and autophagy degradation factors could be conducted in the hTDP43 mouse model to determine whether there is binding. Lack of binding between these factors will, therefore, attribute a specific deficiency in autophagy degradation to SGs. This would, therefore, directly attribute alterations in SGs preventing autophagy clearance in ALS.

Therapeutic Potential of Targeting SGs in ALS

As recent evidence has pointed to SGs playing pathological roles in ALS, they could, therefore, present viable therapeutic targets (refer to introduction for more information). Previous work has shown that terazosin, a drug that had beneficial outcomes in multiple ALS models, also rescued SG dynamics *in vitro* (Chaytow et al., 2022). However, the impact of terazosin in rescuing SG dynamics *in vivo* has not been investigated. Results showed that there was a significant upregulation of SG formation in saline-treated Tg/Tg spinal cords compared to saline-treated NTg controls (Figures 33, 34). This confirms and validates our previous results (Figure 16). However, terazosin treatment seemed to have a differential effect in Tg/Tg spinal cords, with two distinct groups either showing no change in SG formation compared to saline-treated Tg/Tg or a significant decrease in SG formation comparable to the level seen in saline-treated NTg spinal cords (Figures 33, 34). This bimodal response could be due to a biological effect. To determine the impact of terazosin on SG formation, mice were treated with 100 ug/kg of saline or terazosin, administered daily from day of birth and sacrificed at the late symptomatic stage (P19). However, due to biological variation, these mice could have experienced different disease severity, which might be impacting the results. Therefore, to analyse the effect on terazosin modulating SG formation, this experiment could then be repeated with mice being sacrificed at a specific disease stage to determine whether variation in the results seen could be due to a difference in disease stage between the mice analysed.

Additionally, terazosin does not have a direct effect on SG formation. Therefore, different compounds could be utilised to determine whether SGs could be modulated in an ALS *in vivo* setting. Terazosin works by increasing PGK1 activity and upregulating glycolysis function (Chaytow et al., 2022). PGK1 activity itself does not have any direct impact on SGs. PGK1 mediates the AKT/mTOR pathway and autophagy initiation through phosphorylating beclin, therefore, could induce either SG formation or degradation (He et al., 2019; Lin et al., 2024; Qian et al., 2017; Sfakianos et al., 2018). Recently, two small molecules inhibiting G3BP1 and G3BP2 have been shown to inhibit stress granule formation and additionally dissolves pre-formed stress granules in vitro in multiple different cell types, including human iPSC-derived neurons (Freibaum et al., 2023). Therefore, these might present more specific options to understand whether SG formation could be modulated in vivo. Additionally, these compounds also have the capability of dissolving SG after formation, therefore allowing the further determination of whether SGs are causing or the consequence of ALS pathology. These compounds should, therefore, be applied in the hTDP43 to determine whether rescuing SG could reduce ALS pathology. This would further expand the understanding of the role SGs play in ALS pathology.

Conclusion

This study shows that there are significant changes in SGs at both the protein level and transcription level in the severe hTDP43 ALS mouse model. This is the first study showing changes in SG dynamics without the use of an external stressor in ALS models *in vivo*. Consistent with previous findings, we show that SG proteins colocalize with the ALS-associated proteins, TDP43, at the late symptomatic disease stage. Changes in SG dynamics were specific to the late symptomatic disease timepoint, the timepoint in which TDP43 mislocalization occurs, further supporting a specific role for SG formation in seeding TDP43 aggregates. Significant upregulation in markers for chronic cellular stress pathways, neuroinflammation, and oxidative stress was also detected at the late symptomatic disease stage, implying that they could be involved in SG upregulation. Key factors that are regulated by protective SG, ROS, and NLRP3 inflammasome activation were also upregulated in the hTDP43 mouse model, suggesting a possible pathological role for SG formation in this model. We further found that autophagy, the mechanism responsible for breaking down SGs, was unaffected in the hTDP43 mouse model. Our work shows that there are significant changes in SG formation in ALS, warranting further investigation to fully reveal the contribution of SG dynamics to ALS pathogenesis.

Bibliography

Alami, N. H., Smith, R. B., Carrasco, M. A., Williams, L. A., Winborn, C. S., Han, S. S. W., Kiskinis, E., Winborn, B., Freibaum, B. D., Kanagaraj, A., Clare, A. J., Badders, N. M., Bilican, B., Chaum, E., Chandran, S., Shaw, C. E., Eggan, K. C., Maniatis, T., & Taylor, J. P. (2014). Axonal Transport of TDP-43 mRNA Granules Is Impaired by ALS-Causing Mutations. *Neuron*, *81*(3), 536–543. https://doi.org/10.1016/j.neuron.2013.12.018

Al-Chalabi, A., Fang, F., Hanby, M. F., Leigh, P. N., Shaw, C. E., Ye, W., & Rijsdijk, F. (2010). An estimate of amyotrophic lateral sclerosis heritability using twin data. *Journal of Neurology, Neurosurgery and Psychiatry*, *81*(12), 1324–1326. https://doi.org/10.1136/jnnp.2010.207464

Alexianu, M. E., Ho, B. -K, Mohamed, A. H., La Bella, V., Smith, R. G., & Appel, S. H. (1994). The role of calcium-binding proteins in selective motoneuron vulnerability in amyotrophic lateral sclerosis. *Annals of Neurology*, *36*(6), 846–858. https://doi.org/10.1002/ana.410360608

Alhindi, A., Shand, M., Smith, H. L., Leite, A. S., Huang, Y. T., van der Hoorn, D., Ridgway, Z., Faller, K. M. E., Jones, R. A., Gillingwater, T. H., & Chaytow, H. (2023). Neuromuscular junction denervation and terminal Schwann cell loss in the hTDP-43 overexpression mouse model of amyotrophic lateral sclerosis. *Neuropathology and Applied Neurobiology*, *49*(4). https://doi.org/10.1111/nan.12925

Aly, A., Laszlo, Z. I., Rajkumar, S., Demir, T., Hindley, N., Lamont, D. J., Lehmann, J., Seidel, M., Sommer, D., Franz-Wachtel, M., Barletta, F., Heumos, S., Czemmel, S., Kabashi, E., Ludolph, A., Boeckers, T. M., Henstridge, C. M., & Catanese, A. (2023). Integrative proteomics highlight presynaptic alterations and c-Jun misactivation as convergent pathomechanisms in ALS. *Acta Neuropathologica*, *146*(3), 451–475. https://doi.org/10.1007/s00401-023-02611-y

Amen, T., & Kaganovich, D. (2021). Stress granules inhibit fatty acid oxidation by modulating mitochondrial permeability. *Cell Reports*, *35*(11). https://doi.org/10.1016/j.celrep.2021.109237

Amin, A., Perera, N. D., Beart, P. M., Turner, B. J., & Shabanpoor, F. (2020). Amyotrophic lateral sclerosis and autophagy: Dysfunction and therapeutic targeting. In *Cells* (Vol. 9, Issue 11, pp. 1–30). Multidisciplinary Digital Publishing Institute (MDPI). https://doi.org/10.3390/cells9112413

An, H., Litscher, G., Watanabe, N., Wei, W., Hashimoto, T., Iwatsubo, T., Buchman, V. L., & Shelkovnikova, T. A. (2022). ALS-linked cytoplasmic FUS assemblies are compositionally different from physiological stress granules and sequester hnRNPA3, a novel modifier of FUS toxicity. *Neurobiology of Disease*, *162*. https://doi.org/10.1016/j.nbd.2021.105585

Andrew, A. S., Bradley, W. G., Peipert, D., Butt, T., Amoako, K., Pioro, E. P., Tandan, R., Novak, J., Quick, A., Pugar, K. D., Sawlani, K., Katirji, B., Hayes, T. A., Cazzolli, P., Gui, J., Mehta, P., Horton, D. K., & Stommel, E. W. (2021). Risk factors for amyotrophic lateral sclerosis: A regional United States case-control study. *Muscle and Nerve*, *63*(1), 52–59. https://doi.org/10.1002/mus.27085

Andrews, J. A., Jackson, C. E., Heiman-Patterson, T. D., Bettica, P., Brooks, B. R., & Pioro, E. P. (2020). Real-world evidence of riluzole effectiveness in treating amyotrophic lateral sclerosis. In *Amyotrophic Lateral Sclerosis and Frontotemporal Degeneration* (Vol. 21, Issues 7–8, pp. 509–518). Taylor and Francis Ltd. https://doi.org/10.1080/21678421.2020.1771734

Annunziato, L., Pannaccione, A., Cataldi, M., Secondo, A., Castaldo, P., Renzo, G. Di, & Taglialatela, M. (2002). Modulation of ion channels by reactive oxygen and nitrogen species: a pathophysiological role in brain aging? In *Neurobiology of Aging* (Vol. 23).

Ashok, A., Andrabi, S. S., Mansoor, S., Kuang, Y., Kwon, B. K., & Labhasetwar, V. (2022). Antioxidant Therapy in Oxidative Stress-Induced Neurodegenerative Diseases: Role of Nanoparticle-Based Drug Delivery Systems in Clinical Translation. In *Antioxidants* (Vol. 11, Issue 2). MDPI. https://doi.org/10.3390/antiox11020408

Austin, A., Beresford, L., Price, G., Cunningham, T., Kalmar, B., & Yon, M. (2022). Sectioning and Counting of Motor Neurons in the L3 to L6 Region of the Adult Mouse Spinal Cord. *Current Protocols*, *2*(5). https://doi.org/10.1002/cpz1.428

Bagyinszky, E., Hulme, J., & An, S. S. A. (2023). Studies of Genetic and Proteomic Risk Factors of Amyotrophic Lateral Sclerosis Inspire Biomarker Development and Gene Therapy. In *Cells* (Vol. 12, Issue 15). Multidisciplinary Digital Publishing Institute (MDPI). https://doi.org/10.3390/cells12151948

Baldwin, K. R., Godena, V. K., Hewitt, V. L., & Whitworth, A. J. (2016). Axonal transport defects are a common phenotype in Drosophila models of ALS. *Human Molecular Genetics*, *25*(12), 2378–2392. https://doi.org/10.1093/hmg/ddw105

Bánfi, B., Malgrange, B., Knisz, J., Steger, K., Dubois-Dauphin, M., & Krause, K. H. (2004). NOX3, a superoxide-generating NADPH oxidase of the inner ear. *Journal of Biological Chemistry*, *279*(44), 46065–46072. https://doi.org/10.1074/jbc.M403046200

Beal, M. F., Ferrante, R. J., Browne, S. E., Matthews, R. T., Kowall, N. W., & Brown, R. H. (1997). Increased 3-nitrotyrosine in both sporadic and familial amyotrophic lateral sclerosis. *Annals of Neurology*, *42*(4), 644–654. https://doi.org/10.1002/ana.410420416

Becker, L. A., Huang, B., Bieri, G., Ma, R., Knowles, D. A., Jafar-Nejad, P., Messing, J., Kim, H. J., Soriano, A., Auburger, G., Pulst, S. M., Taylor, J. P., Rigo, F., & Gitler, A. D. (2017). Therapeutic reduction of ataxin-2 extends lifespan and reduces pathology in TDP-43 mice. *Nature*, *544*(7650), 367–371. https://doi.org/10.1038/nature22038

Beckers, J., Tharkeshwar, A. K., Fumagalli, L., Contardo, M., Van Schoor, E., Fazal, R., Thal, D. R., Chandran, S., Mancuso, R., Van Den Bosch, L., & Van Damme, P. (2023). A toxic gain-of-function mechanism in C9orf72 ALS impairs the autophagy-lysosome pathway in neurons. *Acta Neuropathologica Communications*, *11*(1). https://doi.org/10.1186/s40478-023-01648-0

Béland, L. C., Markovinovic, A., Jakovac, H., De Marchi, F., Bilic, E., Mazzini, L., Kriz, J., & Munitic, I. (2020). Immunity in amyotrophic lateral sclerosis: Blurred lines between excessive inflammation and inefficient immune responses. In *Brain Communications* (Vol. 2, Issue 2). Oxford University Press. https://doi.org/10.1093/braincomms/fcaa124

Bendotti, C., Bonetto, V., Pupillo, E., Logroscino, G., Al-Chalabi, A., Lunetta, C., Riva, N., Mora, G., Lauria, G., Weishaupt, J. H., Agosta, F., Malaspina, A., Basso, M., Greensmith, L., Van Den Bosch, L., Ratti, A., Corbo, M., Hardiman, O., Chiò, A., … Beghi, E. (2020). Focus on the heterogeneity of amyotrophic lateral sclerosis. In *Amyotrophic Lateral Sclerosis and Frontotemporal Degeneration* (Vol. 21, Issues 7–8, pp. 485–495). Taylor and Francis Ltd. https://doi.org/10.1080/21678421.2020.1779298

Bernardi, P., Gerle, C., Halestrap, A. P., Jonas, E. A., Karch, J., Mnatsakanyan, N., Pavlov, E., Sheu, S. S., & Soukas, A. A. (2023). Identity, structure, and function of the mitochondrial permeability transition pore: controversies, consensus, recent advances, and future directions. In *Cell Death and Differentiation* (Vol. 30, Issue 8, pp. 1869–1885). Springer Nature. https://doi.org/10.1038/s41418-023-01187-0

Besnard-Guérin, C. (2020). Cytoplasmic localization of amyotrophic lateral sclerosis-related TDP-43 proteins modulates stress granule formation. *European Journal of Neuroscience*, *52*(8), 3995–4008. https://doi.org/10.1111/ejn.14762

Blevins, H. M., Xu, Y., Biby, S., & Zhang, S. (2022). The NLRP3 Inflammasome Pathway: A Review of Mechanisms and Inhibitors for the Treatment of Inflammatory Diseases. In *Frontiers in Aging Neuroscience* (Vol. 14). Frontiers Media S.A. https://doi.org/10.3389/fnagi.2022.879021

Bonifacino, T., Zerbo, R. A., Balbi, M., Torazza, C., Frumento, G., Fedele, E., Bonanno, G., & Milanese, M. (2021). Nearly 30 years of animal models to study amyotrophic lateral sclerosis: A historical overview and future perspectives. In *International*

Journal of Molecular Sciences (Vol. 22, Issue 22). MDPI. https://doi.org/10.3390/ijms222212236

Bono, S., Feligioni, M., & Corbo, M. (2021). Impaired antioxidant KEAP1-NRF2 system in amyotrophic lateral sclerosis: NRF2 activation as a potential therapeutic strategy. In *Molecular Neurodegeneration* (Vol. 16, Issue 1). BioMed Central Ltd. https://doi.org/10.1186/s13024-021-00479-8

Brown, R. H., & Al-Chalabi, A. (2017). Amyotrophic Lateral Sclerosis. *New England Journal of Medicine*, *377*(2), 162–172. https://doi.org/10.1056/NEJMra1603471

Bryda, E. C. (2016). The Mighty Mouse: The Impact of Rodents on Advances in Biomedical Research. *Missouri Medicine* . www.who.int/cardiovascular_diseases

Buchan, J. R., Kolaitis, R.-M., Paul Taylor, J., & Parker, R. (2013). *Eukaryotic stress granules are cleared by granulophagy and Cdc48/VCP function*.

Buendia, I., Michalska, P., Navarro, E., Gameiro, I., Egea, J., & León, R. (2016). Nrf2-ARE pathway: An emerging target against oxidative stress and neuroinflammation in neurodegenerative diseases. In *Pharmacology and Therapeutics* (Vol. 157, pp. 84–104). Elsevier Inc. https://doi.org/10.1016/j.pharmthera.2015.11.003

Bukreeva, I., Campi, G., Fratini, M., Spanò, R., Bucci, D., Battaglia, G., Giove, F., Bravin, A., Uccelli, A., Venturi, C., Mastrogiacomo, M., & Cedola, A. (2017). Quantitative 3D investigation of Neuronal network in mouse spinal cord model. *Scientific Reports*, *7*. https://doi.org/10.1038/srep41054

Campos-Melo, D., Hawley, Z. C. E., Droppelmann, C. A., & Strong, M. J. (2021). The Integral Role of RNA in Stress Granule Formation and Function. In *Frontiers in Cell and Developmental Biology* (Vol. 9). Frontiers Media S.A. https://doi.org/10.3389/fcell.2021.621779

Castillo, K., Nassif, M., Valenzuela, V., Rojas, F., Matus, S., Mercado, G., Court, F. A., Van Zundert, B., & Hetz, C. (2013). Trehalose delays the progression of amyotrophic lateral sclerosis by enhancing autophagy in motoneurons. *Autophagy*, *9*(9), 1308–1320. https://doi.org/10.4161/auto.25188

Chai, A., Withers, J., Koh, Y. H., Parry, K., Bao, H., Zhang, B., Budnik, V., & Pennetta, G. (2008). hVAPB, the causative gene of a heterogeneous group of motor neuron diseases in humans, is functionally interchangeable with its Drosophila homologue DVAP-33A at the neuromuscular junction. *Human Molecular Genetics*, *17*(2), 266–280. https://doi.org/10.1093/hmg/ddm303

Chaytow, H., Carroll, E., Gordon, D., Huang, Y.-T., van der Hoorn, D., Louise Smith, H., Becker, T., Gwynne Becker, C., Maud Edwige Faller, K., Talbot, K., & Henry Gillingwater, T. (2022). Targeting phosphoglycerate kinase 1 with terazosin improves motor neuron phenotypes in multiple models of amyotrophic lateral sclerosis. *EBioMedicine*, *83*, 104202. https://doi.org/10.1016/j

Chen, D., Wang, Y., & Chin, E. R. (2015). Activation of the endoplasmic reticulum stress response in skeletal muscle of G93a*SOD1 amyotrophic lateral sclerosis mice. *Frontiers in Cellular Neuroscience*, *9*(MAY). https://doi.org/10.3389/fncel.2015.00170

Chen, H., Richard, M., Sandler, D. P., Umbach, D. M., & Kamel, F. (2007). Head Injury and Amyotrophic Lateral Sclerosis NIH Public Access. In *Am J Epidemiol* (Vol. 166, Issue 7).

Chen, L., & Liu, B. (2017). Relationships between Stress Granules, Oxidative Stress, and Neurodegenerative Diseases. In *Oxidative Medicine and Cellular Longevity* (Vol. 2017). Hindawi Limited. https://doi.org/10.1155/2017/1809592

Chen, X., Barclay, J. W., Burgoyne, R. D., & Morgan, A. (2015). Using C. elegans to discover therapeutic compounds for ageing-associated neurodegenerative diseases. *Chemistry Central Journal*, *9*(1). https://doi.org/10.1186/s13065-015-0143-y

Chiò, A., Mazzini, L., D'Alfonso, S., Corrado, L., Canosa, A., Moglia, C., Manera, U., Bersano, E., Brunetti, M., Barberis, M., Veldink, J. H., Van Den Berg, L. H., Pearce, N., Sproviero, W., McLaughlin, R., Vajda, A., Hardiman, O., Rooney, J., Mora, G., … Al-Chalabi, A. (2018). The multistep hypothesis of ALS revisited. *Neurology*, *91*(7), e635–e642. https://doi.org/10.1212/WNL.0000000000005996

Chitiprolu, M., Jagow, C., Tremblay, V., Bondy-Chorney, E., Paris, G., Savard, A., Palidwor, G., Barry, F. A., Zinman, L., Keith, J., Rogaeva, E., Robertson, J., Lavallée-Adam, M., Woulfe, J., Couture, J. F., Côté, J., & Gibbings, D. (2018). A complex of C9ORF72 and p62 uses arginine methylation to eliminate stress granules by autophagy. *Nature Communications*, *9*(1). https://doi.org/10.1038/s41467-018-05273-7

Cho, H., & Shukla, S. (2021). Role of edaravone as a treatment option for patients with amyotrophic lateral sclerosis. In *Pharmaceuticals* (Vol. 14, Issue 1, pp. 1–14). MDPI AG. https://doi.org/10.3390/ph14010029

Chong, W. C., Shastri, M. D., & Eri, R. (2017). Endoplasmic reticulum stress and oxidative stress: A vicious nexus implicated in bowel disease pathophysiology. In *International Journal of Molecular Sciences* (Vol. 18, Issue 4). MDPI AG. https://doi.org/10.3390/ijms18040771

Chua, J. P., De Calbiac, H., Kabashi, E., & Barmada, S. J. (2021). Autophagy and ALS: mechanistic insights and therapeutic implications. In *Autophagy*. Bellwether Publishing, Ltd. https://doi.org/10.1080/15548627.2021.1926656

Colombrita, C., Zennaro, E., Fallini, C., Weber, M., Sommacal, A., Buratti, E., Silani, V., & Ratti, A. (2009). TDP-43 is recruited to stress granules in conditions of oxidative insult. *Journal of Neurochemistry*, *111*(4), 1051–1061. https://doi.org/10.1111/j.1471-4159.2009.06383.x

Cotterill, S., & Yamaguchi, M. (2024). Role of Drosophila in Human Disease Research 3.0. In *International Journal of Molecular Sciences* (Vol. 25, Issue 1). Multidisciplinary Digital Publishing Institute (MDPI). https://doi.org/10.3390/ijms25010292

Cui, Q., Liu, Z., & Bai, G. (2024). Friend or foe: The role of stress granule in neurodegenerative disease. In *Neuron*. Cell Press. https://doi.org/10.1016/j.neuron.2024.04.025

Cunha-Oliveira, T., Montezinho, L., Mendes, C., Firuzi, O., Saso, L., Oliveira, P. J., & Silva, F. S. G. (2020). Oxidative Stress in Amyotrophic Lateral Sclerosis: Pathophysiology and Opportunities for Pharmacological Intervention. In *Oxidative Medicine and Cellular Longevity* (Vol. 2020). Hindawi Limited. https://doi.org/10.1155/2020/5021694

De Santis, R., Santini, L., Colantoni, A., Peruzzi, G., de Turris, V., Alfano, V., Bozzoni, I., & Rosa, A. (2017). FUS Mutant Human Motoneurons Display Altered Transcriptome and microRNA Pathways with Implications for ALS Pathogenesis. *Stem Cell Reports*, *9*(5), 1450–1462. https://doi.org/10.1016/j.stemcr.2017.09.004

Desai, P., & Bandopadhyay, R. (2020). Pathophysiological implications of RNP granules in frontotemporal dementia and ALS. In *Neurochemistry International* (Vol. 140). Elsevier Ltd. https://doi.org/10.1016/j.neuint.2020.104819

Dewey, C. M., Cenik, B., Sephton, C. F., Dries, D. R., Mayer, P., Good, S. K., Johnson, B. A., Herz, J., & Yu, G. (2011). TDP-43 Is Directed to Stress Granules by Sorbitol, a Novel Physiological Osmotic and Oxidative Stressor. *Molecular and Cellular Biology*, *31*(5), 1098–1108. https://doi.org/10.1128/mcb.01279-10

Dimasi, P., Quintiero, A., Shelkovnikova, T. A., & Buchman, V. L. (2017). Modulation of p-eIF2α cellular levels and stress granule assembly/disassembly by trehalose. *Scientific Reports*, *7*. https://doi.org/10.1038/srep44088

Ding, B.-Y., Xie, C.-N., Xie, J.-Y., Gao, Z.-W., Fei, X.-W., Hong, E.-H., Chen, W.-J., & Chen, Y.-Z. (2022). Knockdown of NADPH oxidase 4 reduces mitochondrial oxidative stress and neuronal pyroptosis following intracerebral hemorrhage. *Neural Regeneration Research*, *0*(0), 0. https://doi.org/10.4103/1673-5374.360249

Ding, Q., Chaplin, J., Morris, M. J., Hilliard, M. A., Wolvetang, E., Ng, D. C. H., & Noakes, P. G. (2021). TDP-43 Mutation Affects Stress Granule Dynamics in Differentiated

NSC-34 Motoneuron-Like Cells. *Frontiers in Cell and Developmental Biology*, *9*. https://doi.org/10.3389/fcell.2021.611601

Dong, Y., Lozinski, B. M., Silva, C., & Yong, V. W. (2021). Studying the microglia response to oxidized phosphatidylcholine in primary mouse neuron culture and mouse spinal cord. *STAR Protocols*, *2*(4). https://doi.org/10.1016/j.xpro.2021.100853

Douglas, A. G. L., & Baralle, D. (2023). Reduced penetrance of gene variants causing amyotrophic lateral sclerosis. *Journal of Medical Genetics*, *61*(3), 294–297. https://doi.org/10.1136/jmg-2023-109580

Du, Z. W., Chen, H., Liu, H., Lu, J., Qian, K., Huang, C. T. L., Zhong, X., Fan, F., & Zhang, S. C. (2015). Generation and expansion of highly pure motor neuron progenitors from human pluripotent stem cells. *Nature Communications*, *6*. https://doi.org/10.1038/ncomms7626

Dubinski, A., Gagne, M., Peyrard, S., Gordon, D., Talbot, K., & Vande Velde, C. (2023). Stress granule assembly in vivo is deficient in the CNS of mutant TDP-43 ALS mice. *Human Molecular Genetics*, *32*(2), 319–332. https://doi.org/10.1093/hmg/ddac206

Dudman, J., & Qi, X. (2020). Stress Granule Dysregulation in Amyotrophic Lateral Sclerosis. In *Frontiers in Cellular Neuroscience* (Vol. 14). Frontiers Media S.A. https://doi.org/10.3389/fncel.2020.598517

Eaton, S. L., Roche, S. L., Llavero Hurtado, M., Oldknow, K. J., Farquharson, C., Gillingwater, T. H., & Wishart, T. M. (2013). Total Protein Analysis as a Reliable Loading Control for Quantitative Fluorescent Western Blotting. *PLoS ONE*, *8*(8). https://doi.org/10.1371/journal.pone.0072457

Elden, A. C., Kim, H. J., Hart, M. P., Chen-Plotkin, A. S., Johnson, B. S., Fang, X., Armakola, M., Geser, F., Greene, R., Lu, M. M., Padmanabhan, A., Clay-Falcone, D., McCluskey, L., Elman, L., Juhr, D., Gruber, P. J., Rüb, U., Auburger, G., Trojanowski, J. Q., … Gitler, A. D. (2010). Ataxin-2 intermediate-length polyglutamine expansions are associated with increased risk for ALS. *Nature*, *466*(7310), 1069–1075. https://doi.org/10.1038/nature09320

Fang, T., Al Khleifat, A., Meurgey, J. H., Jones, A., Leigh, P. N., Bensimon, G., & Al-Chalabi, A. (2018). Stage at which riluzole treatment prolongs survival in patients with amyotrophic lateral sclerosis: a retrospective analysis of data from a dose-ranging study. *The Lancet Neurology*, *17*(5), 416–422. https://doi.org/10.1016/S1474-4422(18)30054-1

Fernandes, N., Eshleman, N., & Buchan, J. R. (2018). *Stress Granules and ALS: A Case of Causation or Correlation?* (R. Sattler & C. J. Donnelley, Eds.; Vol. 20). Springer. http://www.springer.com/series/8787

Fiesel, F. C., & Kahle, P. J. (2011). TDP-43 and FUS/TLS: Cellular functions and implications for neurodegeneration. In *FEBS Journal* (Vol. 278, Issue 19, pp. 3550–3568). https://doi.org/10.1111/j.1742-4658.2011.08258.x

Freibaum, B. D., Messing, J., Nakamura, H., Yurtsever, U., Wu, J., Kim, H. J., Hixon, J., Lemieux, R., Duffner, J., Huynh, W., Wong, K., White, M., Lee, C., Meyers, R., Parker, R., & Taylor, J. P. (2023). Identification of small molecule inhibitors of G3BP-driven stress granule formation. *BioRxiv*. https://doi.org/10.1101/2023.06.27.546770

Fujikawa, D., Nakamura, T., Yoshioka, D., Li, Z., Moriizumi, H., Taguchi, M., Tokai-Nishizumi, N., Kozuka-Hata, H., Oyama, M., & Takekawa, M. (2023). Stress granule formation inhibits stress-induced apoptosis by selectively sequestering executioner caspases. *Current Biology*, *33*(10), 1967-1981.e8. https://doi.org/10.1016/j.cub.2023.04.012

Fujimura, K., Sasaki, A. T., & Anderson, P. (2012). Selenite targets eIF4E-binding protein-1 to inhibit translation initiation and induce the assembly of non-canonical stress granules. *Nucleic Acids Research*, *40*(16), 8099–8110. https://doi.org/10.1093/nar/gks566

Gagliardi, D., Ripellino, P., Meneri, M., Del Bo, R., Antognozzi, S., Comi, G. Pietro, Gobbi, C., Ratti, A., Ticozzi, N., Silani, V., Ronchi, D., & Corti, S. (2023). Clinical and molecular features of patients with amyotrophic lateral sclerosis and SOD1 mutations: a monocentric study. *Frontiers in Neurology*, *14*. https://doi.org/10.3389/fneur.2023.1169689

Gautam, M., Gunay, A., Chandel, N. S., & Ozdinler, P. H. (2022). Mitochondrial dysregulation occurs early in ALS motor cortex with TDP-43 pathology and suggests maintaining NAD+ balance as a therapeutic strategy. *Scientific Reports*, *12*(1). https://doi.org/10.1038/s41598-022-08068-5

Granatiero, V., Sayles, N. M., Savino, A. M., Konrad, C., Kharas, M. G., Kawamata, H., & Manfredi, G. (2021). Modulation of the IGF1R-MTOR pathway attenuates motor neuron toxicity of human ALS SOD1G93A astrocytes. *Autophagy*, *17*(12), 4029–4042. https://doi.org/10.1080/15548627.2021.1899682

Gurumurthy, C. B., O'Brien, A. R., Quadros, R. M., Adams, J., Alcaide, P., Ayabe, S., Ballard, J., Batra, S. K., Beauchamp, M. C., Becker, K. A., Bernas, G., Brough, D., Carrillo-Salinas, F., Chan, W., Chen, H., Dawson, R., Demambro, V., D'Hont, J., Dibb, K. M., ... Burgio, G. (2019). Reproducibility of CRISPR-Cas9 methods for generation of conditional mouse alleles: A multi-center evaluation. *Genome Biology*, *20*(1). https://doi.org/10.1186/s13059-019-1776-2

Halliwell, B. (2006). Oxidative stress and neurodegeneration: Where are we now? In *Journal of Neurochemistry* (Vol. 97, Issue 6, pp. 1634–1658). https://doi.org/10.1111/j.1471-4159.2006.03907.x

He, Y., Luo, Y., Zhang, D., Wang, X., Zhang, P., Li, H., Ejaz, S., & Liang, S. (2019). PGK1-mediated cancer progression and drug resistance. In *Am J Cancer Res* (Vol. 9, Issue 11). www.ajcr.us/

Hemerková, P., & Vališ, M. (2021). Role of oxidative stress in the pathogenesis of amyotrophic lateral sclerosis: Antioxidant metalloenzymes and therapeutic strategies. In *Biomolecules* (Vol. 11, Issue 3, pp. 1–24). MDPI AG. https://doi.org/10.3390/biom11030437

Herman, A. B., Silva Afonso, M., Kelemen, S. E., Ray, M., Vrakas, C. N., Burke, A. C., Scalia, R. G., Moore, K., & Autieri, M. V. (2019). Regulation of stress granule formation by inflammation, vascular injury, and atherosclerosis. *Arteriosclerosis, Thrombosis, and Vascular Biology*, *39*(10), 2014–2027. https://doi.org/10.1161/ATVBAHA.119.313034

Hill, S. M., Wrobel, L., Ashkenazi, A., Fernandez-Estevez, M., Tan, K., Bürli, R. W., & Rubinsztein, D. C. (2021). VCP/p97 regulates Beclin-1-dependent autophagy initiation. *Nature Chemical Biology*, *17*(4), 448–455. https://doi.org/10.1038/s41589-020-00726-x

Hofmann, S., Kedersha, N., Anderson, P., & Ivanov, P. (2021). Molecular mechanisms of stress granule assembly and disassembly. In *Biochimica et Biophysica Acta - Molecular Cell Research* (Vol. 1868, Issue 1). Elsevier B.V. https://doi.org/10.1016/j.bbamcr.2020.118876

Honorat, J. A., Kinoshita, M., Okuno, T., Takata, K., Koda, T., Tada, S., Shirakura, T., Fujimura, H., Mochizuki, H., Sakoda, S., & Nakatsuji, Y. (2013). Xanthine Oxidase Mediates Axonal and Myelin Loss in a Murine Model of Multiple Sclerosis. *PLoS ONE*, *8*(8). https://doi.org/10.1371/journal.pone.0071329

Hu, L. D., Mao, S., Lin, L., Bai, G., Liu, B., & Mao, J. (2022). Stress granules in the spinal muscular atrophy and amyotrophic lateral sclerosis: The correlation and promising therapy. In *Neurobiology of Disease* (Vol. 170). Academic Press Inc. https://doi.org/10.1016/j.nbd.2022.105749

Hu, S., Claud, E. C., Musch, M. W., & Chang, E. B. (2010). Stress granule formation mediates the inhibition of colonic Hsp70 translation by interferon-γ and tumor necrosis factor-α. *American Journal of Physiology - Gastrointestinal and Liver Physiology*, *298*(4). https://doi.org/10.1152/ajpgi.00234.2009

Huang, C., Yan, S., & Zhang, Z. (2020). Maintaining the balance of TDP-43, mitochondria, and autophagy: a promising therapeutic strategy for neurodegenerative diseases.

In *Translational Neurodegeneration* (Vol. 9, Issue 1). BioMed Central Ltd. https://doi.org/10.1186/s40035-020-00219-w

Huang, Y. T., van der Hoorn, D., Ledahawsky, L. M., Motyl, A. A. L., Jordan, C. Y., Gillingwater, T. H., & Groen, E. J. N. (2019). Robust comparison of protein levels across tissues and throughout development using standardized quantitative western blotting. *Journal of Visualized Experiments*, *2019*(146). https://doi.org/10.3791/59438

Hüttemann, M., Klewer, S., Lee, I., Pecinova, A., Pecina, P., Liu, J., Lee, M., Doan, J. W., Larson, D., Slack, E., Maghsoodi, B., Erickson, R. P., & Grossman, L. I. (2012). Mice deleted for heart-type cytochrome c oxidase subunit 7a1 develop dilated cardiomyopathy. *Mitochondrion*, *12*(2), 294–304. https://doi.org/10.1016/j.mito.2011.11.002

Ikawa, M., Okazawa, H., Nakamoto, Y., & Yoneda, M. (2020). Pet imaging for oxidative stress in neurodegenerative disorders associated with mitochondrial dysfunction. In *Antioxidants* (Vol. 9, Issue 9, pp. 1–22). MDPI. https://doi.org/10.3390/antiox9090861

Ingre, C., Roos, P. M., Piehl, F., Kamel, F., & Fang, F. (2015). Risk factors for amyotrophic lateral sclerosis. In *Clinical Epidemiology* (Vol. 7, pp. 181–193). Dove Medical Press Ltd. https://doi.org/10.2147/CLEP.S37505

Jackson, L., Dumanli, S., Johnson, M. H., Fagan, S. C., & Ergul, A. (2020). Microglia knockdown reduces inflammation and preserves cognition in diabetic animals after experimental stroke. *Journal of Neuroinflammation*, *17*(1). https://doi.org/10.1186/s12974-020-01815-3

Jentsch, S., & Rumpf, S. (2007). Cdc48 (p97): a “molecular gearbox” in the ubiquitin pathway? *Trends in Biochemical Sciences*, *32*(1), 6–11. https://doi.org/10.1016/j.tibs.2006.11.005

Johann, S., Heitzer, M., Kanagaratnam, M., Goswami, A., Rizo, T., Weis, J., Troost, D., & Beyer, C. (2015). NLRP3 inflammasome is expressed by astrocytes in the SOD1 mouse model of ALS and in human sporadic ALS patients. *GLIA*, *63*(12), 2260–2273. https://doi.org/10.1002/glia.22891

Kageyama, S., Gudmundsson, S. R., Sou, Y. S., Ichimura, Y., Tamura, N., Kazuno, S., Ueno, T., Miura, Y., Noshiro, D., Abe, M., Mizushima, T., Miura, N., Okuda, S., Motohashi, H., Lee, J. A., Sakimura, K., Ohe, T., Noda, N. N., Waguri, S., … Komatsu, M. (2021). p62/SQSTM1-droplet serves as a platform for autophagosome formation and anti-oxidative stress response. *Nature Communications*, *12*(1). https://doi.org/10.1038/s41467-020-20185-1

Kim, H. J., Raphael, A. R., Ladow, E. S., Mcgurk, L., Weber, R. A., Trojanowski, J. Q., Lee, V. M. Y., Finkbeiner, S., Gitler, A. D., & Bonini, N. M. (2014). Therapeutic modulation of eIF2α phosphorylation rescues TDP-43 toxicity in amyotrophic lateral sclerosis disease models. *Nature Genetics*, *46*(2), 152–160. https://doi.org/10.1038/ng.2853

Kirshner, Z. Z., & Gibbs, R. B. (2018). Use of the REVERT ® total protein stain as a loading control demonstrates significant benefits over the use of housekeeping proteins when analyzing brain homogenates by Western blot: An analysis of samples representing different gonadal hormone states. *Molecular and Cellular Endocrinology*, *473*, 156–165. https://doi.org/10.1016/j.mce.2018.01.015

Kiselyov, K., & Muallem, S. (2016). ROS and intracellular ion channels. In *Cell Calcium* (Vol. 60, Issue 2, pp. 108–114). Churchill Livingstone. https://doi.org/10.1016/j.ceca.2016.03.004

Koppers, M., van Blitterswijk, M. M., Vlam, L., Rowicka, P. A., van Vught, P. W. J., Groen, E. J. N., Spliet, W. G. M., Engelen-Lee, J. Y., Schelhaas, H. J., de Visser, M., van der Kooi, A. J., van der Pol, W. L., Pasterkamp, R. J., Veldink, J. H., & van den Berg, L. H. (2012). VCP mutations in familial and sporadic amyotrophic lateral sclerosis. *Neurobiology of Aging*, *33*(4), 837.e7-837.e13. https://doi.org/10.1016/j.neurobiolaging.2011.10.006

Kowalczyk, P., Sulejczak, D., Kleczkowska, P., Bukowska-Ośko, I., Kucia, M., Popiel, M., Wietrak, E., Kramkowski, K., Wrzosek, K., & Kaczyńska, K. (2021). Mitochondrial oxidative stress—a causative factor and therapeutic target in many diseases. In *International Journal of Molecular Sciences* (Vol. 22, Issue 24). MDPI. https://doi.org/10.3390/ijms222413384

Kozera, B., & Rapacz, M. (2013). Reference genes in real-time PCR. In *Journal of Applied Genetics* (Vol. 54, Issue 4, pp. 391–406). https://doi.org/10.1007/s13353-013-0173-x

Krause, L. J., Herrera, M. G., & Winklhofer, K. F. (2022). The Role of Ubiquitin in Regulating Stress Granule Dynamics. In *Frontiers in Physiology* (Vol. 13). Frontiers Media S.A. https://doi.org/10.3389/fphys.2022.910759

Krisenko, M. O., Higgins, R. L., Ghosh, S., Zhou, Q., Trybula, J. S., Wang, W. H., & Geahlen, R. L. (2015). Syk is recruited to stress granules and promotes their clearance through autophagy. *Journal of Biological Chemistry*, *290*(46), 27803–27815. https://doi.org/10.1074/jbc.M115.642900

Lagier-Tourenne, C., Polymenidou, M., Hutt, K. R., Vu, A. Q., Baughn, M., Huelga, S. C., Clutario, K. M., Ling, S. C., Liang, T. Y., Mazur, C., Wancewicz, E., Kim, A. S., Watt, A., Freier, S., Hicks, G. G., Donohue, J. P., Shiue, L., Bennett, C. F., Ravits, J., … Yeo, G. W. (2012). Divergent roles of ALS-linked proteins FUS/TLS and TDP-43 intersect in processing long pre-mRNAs. *Nature Neuroscience*, *15*(11), 1488–1497. https://doi.org/10.1038/nn.3230

Lee, E. F., Dewson, G., Evangelista, M., Pettikiriarachchi, A., Gold, G. J., Zhu, H., Colman, P. M., & Fairlie, W. D. (2014). The functional differences between pro-survival and pro-apoptotic b cell lymphoma 2 (Bcl-2) proteins depend on structural differences in their Bcl-2 homology 3 (BH3) domains. *Journal of Biological Chemistry*, *289*(52), 36001–36017. https://doi.org/10.1074/jbc.M114.610758

Lee, Y. K., & Lee, J. A. (2016). Role of the mammalian ATG8/LC3 family in autophagy: Differential and compensatory roles in the spatiotemporal regulation of autophagy. In *BMB Reports* (Vol. 49, Issue 8, pp. 424–430). The Biochemical Society of the Republic of Korea. https://doi.org/10.5483/BMBRep.2016.49.8.081

Leibiger, C., Deisel, J., Aufschnaiter, A., Ambros, S., Tereshchenko, M., Verheijen, B. M., Büttner, S., & Braun, R. J. (2018). TDP-43 controls lysosomal pathways thereby determining its own clearance and cytotoxicity. *Human Molecular Genetics*, *27*(9), 1593–1607. https://doi.org/10.1093/hmg/ddy066

Li, A., Sé Gui, J., Heinemann, S. H., & Hoshi, T. (1998). *Oxidation Regulates Cloned Neuronal Voltage-Dependent Ca 2 Channels Expressed in Xenopus Oocytes*.

Li, H., Lin, P. H., Gupta, P., Li, X., Zhao, S. L., Zhou, X., Li, Z., Wei, S., Xu, L., Han, R., Lu, J., Tan, T., Yang, D. H., Chen, Z. S., Pawlik, T. M., Merritt, R. E., & Ma, J. (2021). MG53 suppresses tumor progression and stress granule formation by modulating G3BP2 activity in non-small cell lung cancer. *Molecular Cancer*, *20*(1). https://doi.org/10.1186/s12943-021-01418-3

Li, Y., Ray, P., Rao, E. J., Shi, C., Guo, W., Chen, X., Woodruff, E. A., Fushimi, K., & Wu, J. Y. (2010). A Drosophila model for TDP-43 proteinopathy. *Proceedings of the National Academy of Sciences of the United States of America*, *107*(7), 3169–3174. https://doi.org/10.1073/pnas.0913602107

Lin, N., Sun, L., Chai, J., Qi, H., Zhao, Y., Ma, J., Xia, M., & Hu, X. (2024). Stress granules affect the dual PI3K/mTOR inhibitor response by regulating the mitochondrial unfolded protein response. *Cancer Cell International*, *24*(1). https://doi.org/10.1186/s12935-024-03210-x

Liu, G., Ou, S., Cui, H., Li, X., Yin, Z., Gu, D., & Wang, Z. (2021). Head Injury and Amyotrophic Lateral Sclerosis: A Meta-Analysis. In *Neuroepidemiology* (Vol. 55, Issue 1, pp. 11–19). S. Karger AG. https://doi.org/10.1159/000510987

Liu, J., & Wang, F. (2017). Role of neuroinflammation in amyotrophic lateral sclerosis: Cellular mechanisms and therapeutic implications. In *Frontiers in Immunology* (Vol. 8, Issue AUG). Frontiers Media S.A. https://doi.org/10.3389/fimmu.2017.01005

Liu-Yesucevitz, L., Bilgutay, A., Zhang, Y. J., Vanderwyde, T., Citro, A., Mehta, T., Zaarur, N., McKee, A., Bowser, R., Sherman, M., Petrucelli, L., & Wolozin, B. (2010a). Tar DNA binding protein-43 (TDP-43) associates with stress granules: Analysis of cultured cells and pathological brain tissue. *PLoS ONE*, *5*(10). https://doi.org/10.1371/journal.pone.0013250

Liu-Yesucevitz, L., Bilgutay, A., Zhang, Y. J., Vanderwyde, T., Citro, A., Mehta, T., Zaarur, N., McKee, A., Bowser, R., Sherman, M., Petrucelli, L., & Wolozin, B. (2010b). Tar DNA binding protein-43 (TDP-43) associates with stress granules: Analysis of cultured cells and pathological brain tissue. *PLoS ONE*, *5*(10). https://doi.org/10.1371/journal.pone.0013250

Logroscino, G., Traynor, B. J., Hardiman, O., Chió, A., Mitchell, D., Swingler, R. J., Millul, A., Benn, E., & Beghi, E. (2010). Incidence of amyotrophic lateral sclerosis in Europe. *Journal of Neurology, Neurosurgery and Psychiatry*, *81*(4), 385–390. https://doi.org/10.1136/jnnp.2009.183525

Lu, W., Li, J.-P., Jiang, Z.-D., Yang, L., & Liu, X.-Z. (2022). Effects of targeted muscle reinnervation on spinal cord motor neurons in rats following tibial nerve transection. *Neural Regeneration Research*.

Lu, X., Alam, U., Willis, C., & Kennedy, D. (2021). Role of Chikungunya nsP3 in Regulating G3BP1 Activity, Stress Granule Formation and Drug Efficacy. *Archives of Medical Research*, *52*(1), 48–57. https://doi.org/10.1016/j.arcmed.2020.10.002

Mackenzie, I. R., Nicholson, A. M., Sarkar, M., Messing, J., Purice, M. D., Pottier, C., Annu, K., Baker, M., Perkerson, R. B., Kurti, A., Matchett, B. J., Mittag, T., Temirov, J., Hsiung, G. Y. R., Krieger, C., Murray, M. E., Kato, M., Fryer, J. D., Petrucelli, L., … Rademakers, R. (2017). TIA1 Mutations in Amyotrophic Lateral Sclerosis and Frontotemporal Dementia Promote Phase Separation and Alter Stress Granule Dynamics. *Neuron*, *95*(4), 808-816.e9. https://doi.org/10.1016/j.neuron.2017.07.025

Malik, A., & Kanneganti, T. D. (2017). Inflammasome activation and assembly at a glance. *Journal of Cell Science*, *130*(23), 3955–3963. https://doi.org/10.1242/jcs.207365

Mandrioli, J., D’Amico, R., Zucchi, E., Gessani, A., Fini, N., Fasano, A., Caponnetto, C., Chiò, A., Bella, E. D., Lunetta, C., Mazzini, L., Marinou, K., Sorarù, G., De Biasi, S., Lo Tartaro, D., Pinti, M., Nichelli, P., Vicini, R., Cabona, C., … Cossarizza, A. (2018). Rapamycin treatment for amyotrophic lateral sclerosis protocol for a phase II randomized, double-blind, placebo-controlled, multicenter, clinical trial (RAP-ALS trial). *Medicine (United States)*, *97*(24). https://doi.org/10.1097/MD.0000000000011119

Manjaly, Z. R., Scott, K. M., Abhinav, K., Wijesekera, L., Ganesalingam, J., Goldstein, L. H., Janssen, A., Dougherty, A., Willey, E., Stanton, B. R., Turner, M. R., Ampong, M. A., Sakel, M., Orrell, R. W., Howard, R., Shaw, C. E., Leigh, P. N., & Al-Chalabi, A. (2010). The sex ratio in amyotrophic lateral sclerosis: A population based study. *Amyotrophic Lateral Sclerosis*, *11*(5), 439–442. https://doi.org/10.3109/17482961003610853

Mann, J. R., Gleixner, A. M., Mauna, J. C., Gomes, E., DeChellis-Marks, M. R., Needham, P. G., Copley, K. E., Hurtle, B., Portz, B., Pyles, N. J., Guo, L., Calder, C. B., Wills, Z. P., Pandey, U. B., Kofler, J. K., Brodsky, J. L., Thathiah, A., Shorter, J., & Donnelly, C. J. (2019). RNA Binding Antagonizes Neurotoxic Phase Transitions of TDP-43. *Neuron*, *102*(2), 321-338.e8. https://doi.org/10.1016/j.neuron.2019.01.048

Marcelo, A., Koppenol, R., de Almeida, L. P., Matos, C. A., & Nóbrega, C. (2021). Stress granules, RNA-binding proteins and polyglutamine diseases: too much aggregation? In *Cell Death and Disease* (Vol. 12, Issue 6). Springer Nature. https://doi.org/10.1038/s41419-021-03873-8

Marmor-Kollet, H., Siany, A., Kedersha, N., Knafo, N., Rivkin, N., Danino, Y. M., Moens, T. G., Olender, T., Sheban, D., Cohen, N., Dadosh, T., Addadi, Y., Ravid, R., Eitan, C., Toth Cohen, B., Hofmann, S., Riggs, C. L., Advani, V. M., Higginbottom, A., ... Hornstein, E. (2020). Spatiotemporal Proteomic Analysis of Stress Granule Disassembly Using APEX Reveals Regulation by SUMOylation and Links to ALS Pathogenesis. *Molecular Cell*, *80*(5), 876-891.e6. https://doi.org/10.1016/j.molcel.2020.10.032

Matsuki, H., Takahashi, M., Higuchi, M., Makokha, G. N., Oie, M., & Fujii, M. (2013). Both G3BP1 and G3BP2 contribute to stress granule formation. *Genes to Cells*, *18*(2), 135–146. https://doi.org/10.1111/gtc.12023

McDonald, K. K., Aulas, A., Destroismaisons, L., Pickles, S., Beleac, E., Camu, W., Rouleau, G. A., & Velde, C. Vande. (2011). TAR DNA-binding protein 43 (TDP-43) regulates stress granule dynamics via differential regulation of G3BP and TIA-1. *Human Molecular Genetics*, *20*(7), 1400–1410. https://doi.org/10.1093/hmg/ddr021

McGurk, L., Gomes, E., Guo, L., Mojsilovic-Petrovic, J., Tran, V., Kalb, R. G., Shorter, J., & Bonini, N. M. (2018). Poly(ADP-Ribose) Prevents Pathological Phase Separation of TDP-43 by Promoting Liquid Demixing and Stress Granule Localization. *Molecular Cell*, *71*(5), 703-717.e9. https://doi.org/10.1016/j.molcel.2018.07.002

McIntosh, J., Mekrouda, I., Dashti, M., Giuraniuc, C. V., Banks, R. W., Miles, G. B., & Bewick, G. S. (2023). Development of abnormalities at the neuromuscular junction in the SOD1-G93A mouse model of ALS: dysfunction then disruption of postsynaptic structure precede overt motor symptoms. *Frontiers in Molecular Neuroscience*, *16*. https://doi.org/10.3389/fnmol.2023.1169075

McLeod, V. M., Chiam, M. D. F., Perera, N. D., Lau, C. L., Boon, W. C., & Turner, B. J. (2022). Mapping Motor Neuron Vulnerability in the Neuraxis of Male SOD1G93A Mice Reveals Widespread Loss of Androgen Receptor Occurring Early in Spinal Motor Neurons. *Frontiers in Endocrinology*, *13*. https://doi.org/10.3389/fendo.2022.808479

Melachroinou, K., Xilouri, M., Emmanouilidou, E., Masgrau, R., Papazafiri, P., Stefanis, L., & Vekrellis, K. (2013). Deregulation of calcium homeostasis mediates secreted α-synuclein-induced neurotoxicity. *Neurobiology of Aging*, *34*(12), 2853–2865. https://doi.org/10.1016/j.neurobiolaging.2013.06.006

Meyer, H., Bug, M., & Bremer, S. (2012). Emerging functions of the VCP/p97 AAA-ATPase in the ubiquitin system. In *Nature Cell Biology* (Vol. 14, Issue 2, pp. 117–123). https://doi.org/10.1038/ncb2407

Mori, F., Yasui, H., Miki, Y., Kon, T., Arai, A., Kurotaki, H., Tomiyama, M., & Wakabayashi, K. (2024). Colocalization of TDP-43 and stress granules at the early stage of TDP-43 aggregation in amyotrophic lateral sclerosis. *Brain Pathology*, *34*(2). https://doi.org/10.1111/bpa.13215

Mori, R., Wang, Q., Danenberg, K. D., Pinski, J. K., & Danenberg, P. V. (2008). Both β-actin and GAPDH are useful reference genes for normalization of quantitative RT-PCR in human FFPE tissue samples of prostate cancer. *Prostate*, *68*(14), 1555–1560. https://doi.org/10.1002/pros.20815

Niccoli, T., Partridge, L., & Isaacs, A. M. (2017). Ageing as a risk factor for ALS/FTD. In *Human Molecular Genetics* (Vol. 26, Issue R2, pp. R105–R113). Oxford University Press. https://doi.org/10.1093/hmg/ddx247

Nógrádi, B., Nógrádi-Halmi, D., Erdélyi-Furka, B., Kádár, Z., Csont, T., & Gáspár, R. (2024). Mechanism of motoneuronal and pyramidal cell death in amyotrophic lateral sclerosis and its potential therapeutic modulation. In *Cell Death Discovery* (Vol. 10, Issue 1). Springer Nature. https://doi.org/10.1038/s41420-024-02055-7

Oliveira, N. A. S., Pinho, B. R., & Oliveira, J. M. A. (2023). Swimming against ALS: How to model disease in zebrafish for pathophysiological and behavioral studies. In *Neuroscience and Biobehavioral Reviews* (Vol. 148). Elsevier Ltd. https://doi.org/10.1016/j.neubiorev.2023.105138

Paganoni, S., Macklin, E. A., Lee, A., Murphy, A., Chang, J., Zipf, A., Cudkowicz, M., & Atassi, N. (2014). Diagnostic timelines and delays in diagnosing amyotrophic lateral sclerosis (ALS). *Amyotrophic Lateral Sclerosis and Frontotemporal Degeneration*, *15*(5–6), 453–456. https://doi.org/10.3109/21678421.2014.903974

Parfenova, H., Basuroy, S., Bhattacharya, S., Tcheranova, D., Qu, Y., Regan, R. F., Leffler, C. W., Tcheranova, D., & Leffler Glutamate, C. W. (2006). Glutamate induces oxidative stress and apoptosis in cerebral vascular endothelial cells: contributions of HO-1 and HO-2 to cytoprotection. *Am J Physiol Cell Physiol*, *290*, 1399–1410. https://doi.org/10.1152/ajpcell.00386.2005.-In

Parvanovova, P., Evinova, A., Grofik, M., Hnilicova, P., Tatarkova, Z., & Turcanova-Koprusakova, M. (2024). Mitochondrial Dysfunction in Sporadic Amyotrophic Lateral Sclerosis Patients: Insights from High-Resolution Respirometry. *Biomedicines*, *12*(6). https://doi.org/10.3390/biomedicines12061294

Peggion, C., Calì, T., & Brini, M. (2024). Mitochondria Dysfunction and Neuroinflammation in Neurodegeneration: Who Comes First? In *Antioxidants* (Vol. 13, Issue 2). Multidisciplinary Digital Publishing Institute (MDPI). https://doi.org/10.3390/antiox13020240

Philips, T., & Rothstein, J. D. (2015). Rodent models of amyotrophic lateral sclerosis. *Current Protocols in Pharmacology*, *2015*, 5.67.1-5.67.21. https://doi.org/10.1002/0471141755.ph0567s69

Pietras, P., Aulas, A., Fay, M. M., Leśniczak-Staszak, M., Sowiński, M., Lyons, S. M., Szaflarski, W., & Ivanov, P. (2022). Translation inhibition and suppression of stress granules formation by cisplatin. *Biomedicine and Pharmacotherapy*, *145*. https://doi.org/10.1016/j.biopha.2021.112382

Poljšak, B., & Milisav, I. (2012). Clinical implications of cellular stress responses. In *Bosn J Basic Med Sci* (Vol. 12, Issue 2).

Qian, X., Li, X., Cai, Q., Zhang, C., Yu, Q., Jiang, Y., Lee, J. H., Hawke, D., Wang, Y., Xia, Y., Zheng, Y., Jiang, B. H., Liu, D. X., Jiang, T., & Lu, Z. (2017). Phosphoglycerate Kinase 1 Phosphorylates Beclin1 to Induce Autophagy. *Molecular Cell*, *65*(5), 917-931.e6. https://doi.org/10.1016/j.molcel.2017.01.027

Ramesh, N., & Pandey, U. B. (2017). Autophagy dysregulation in ALS: When protein aggregates get out of hand. In *Frontiers in Molecular Neuroscience* (Vol. 10). Frontiers Media S.A. https://doi.org/10.3389/fnmol.2017.00263

Ratti, A., Gumina, V., Lenzi, P., Bossolasco, P., Fulceri, F., Volpe, C., Bardelli, D., Pregnolato, F., Maraschi, A. M., Fornai, F., Silani, V., & Colombrita, C. (2020). Chronic stress induces formation of stress granules and pathological TDP-43 aggregates in human ALS fibroblasts and iPSC-motoneurons. *Neurobiology of Disease*, *145*. https://doi.org/10.1016/j.nbd.2020.105051

Reber, S., Stettler, J., Filosa, G., Colombo, M., Jutzi, D., Lenzken, S. C., Schweingruber, C., Bruggmann, R., Bachi, A., Barabino, S. M., Mühlemann, O., & Ruepp, M. (2016). Minor intron splicing is regulated by FUS and affected by ALS -associated FUS mutants . *The EMBO Journal*, *35*(14), 1504–1521. https://doi.org/10.15252/embj.201593791

Reineke, L. C., & Neilson, J. R. (2019). Differences between acute and chronic stress granules, and how these differences may impact function in human disease. In *Biochemical Pharmacology* (Vol. 162, pp. 123–131). Elsevier Inc. https://doi.org/10.1016/j.bcp.2018.10.009

Richner, M., Jager, S. B., Siupka, P., & Vaegter, C. B. (2017). Hydraulic extrusion of the spinal cord and isolation of dorsal root ganglia in rodents. *Journal of Visualized Experiments*, *2017*(119). https://doi.org/10.3791/55226

Ryan, L., & Rubinsztein, D. C. (2024a). The autophagy of stress granules. *FEBS Letters*, *598*(1), 59–72. https://doi.org/10.1002/1873-3468.14787

Ryan, L., & Rubinsztein, D. C. (2024b). The autophagy of stress granules. *FEBS Letters*, *598*(1), 59–72. https://doi.org/10.1002/1873-3468.14787

Ryu, H. H., Jun, M. H., Min, K. J., Jang, D. J., Lee, Y. S., Kim, H. K., & Lee, J. A. (2014). Autophagy regulates amyotrophic lateral sclerosis-linked fused in sarcoma-positive stress granules in neurons. *Neurobiology of Aging*, *35*(12), 2822–2831. https://doi.org/10.1016/j.neurobiolaging.2014.07.026

Safdar, A., Abadi, A., Akhtar, M., Hettinga, B. P., & Tarnopolsky, M. A. (2009). miRNA in the regulation of skeletal muscle adaptation to acute endurance exercise in C57Bl/6J male mice. *PLoS ONE*, *4*(5). https://doi.org/10.1371/journal.pone.0005610

Sahana, T. G., Chase, K. J., Liu, F., Lloyd, T. E., Rossoll, W., & Zhang, K. (2023). c-Jun N-Terminal Kinase Promotes Stress Granule Assembly and Neurodegeneration in C9orf72-Mediated ALS and FTD. *Journal of Neuroscience*, *43*(17), 3186–3197. https://doi.org/10.1523/JNEUROSCI.1799-22.2023

Saitoh, Y., & Takahashi, Y. (2020). Riluzole for the treatment of amyotrophic lateral sclerosis. *Neurodegenerative Disease Management*, *10*(6), 343–355. https://doi.org/10.2217/nmt-2020-0033

Samir, P., Kesavardhana, S., Patmore, D. M., Gingras, S., Malireddi, R. K. S., Karki, R., Guy, C. S., Briard, B., Place, D. E., Bhattacharya, A., Sharma, B. R., Nourse, A., King, S. V., Pitre, A., Burton, A. R., Pelletier, S., Gilbertson, R. J., & Kanneganti, T. D. (2019). DDX3X acts as a live-or-die checkpoint in stressed cells by regulating NLRP3 inflammasome. *Nature*, *573*(7775), 590–594. https://doi.org/10.1038/s41586-019-1551-2

Sanhueza, M., Zechini, L., Gillespie, T., & Pennetta, G. (2014). Gain-of-function mutations in the ALS8 causative gene VAPB have detrimental effects on neurons and muscles. *Biology Open*, *3*(1), 59–71. https://doi.org/10.1242/bio.20137070

Schram, S., Loeb, J. A., & Song, F. (2020). Disease propagation in amyotrophic lateral sclerosis (ALS): An interplay between genetics and environment. In *Journal of Neuroinflammation* (Vol. 17, Issue 1). BioMed Central Ltd. https://doi.org/10.1186/s12974-020-01849-7

Schubert, D., & Piasecki, D. (2001). *Oxidative Glutamate Toxicity Can Be a Component of the Excitotoxicity Cascade*.

Seguin, S. J., Morelli, F. F., Vinet, J., Amore, D., De Biasi, S., Poletti, A., Rubinsztein, D. C., & Carra, S. (2014). Inhibition of autophagy, lysosome and VCP function impairs stress granule assembly. *Cell Death and Differentiation*, *21*(12), 1838–1851. https://doi.org/10.1038/cdd.2014.103

Sfakianos, A. P., Mellor, L. E., Pang, Y. F., Kritsiligkou, P., Needs, H., Abou-Hamdan, H., Désaubry, L., Poulin, G. B., Ashe, M. P., & Whitmarsh, A. J. (2018). The mTOR-S6 kinase pathway promotes stress granule assembly. *Cell Death and Differentiation*, *25*(10), 1766–1780. https://doi.org/10.1038/s41418-018-0076-9

Shelkovnikova, T. A., Dimasi, P., Kukharsky, M. S., An, H., Quintiero, A., Schirmer, C., Buée, L., Galas, M. C., & Buchman, V. L. (2017). Chronically stressed or stress-preconditioned neurons fail to maintain stress granule assembly. *Cell Death and Disease*, *8*(5). https://doi.org/10.1038/cddis.2017.199

Singh, N., Ray, S., & Srivastava, A. (2018). Clinical mimickers of amyotrophic lateral sclerosis-conditions we cannot afford to miss. In *Annals of Indian Academy of Neurology* (Vol. 21, Issue 3, pp. 173–178). Wolters Kluwer Medknow Publications. https://doi.org/10.4103/aian.AIAN_491_17

Smethurst, P., Risse, E., Tyzack, G. E., Mitchell, J. S., Taha, D. M., Chen, Y. R., Newcombe, J., Collinge, J., Sidle, K., & Patani, R. (2020). Distinct responses of neurons and astrocytes to TDP-43 proteinopathy in amyotrophic lateral sclerosis. *Brain*, *143*(2), 430–440. https://doi.org/10.1093/brain/awz419

Smith, E. F., Shaw, P. J., & De Vos, K. J. (2019). The role of mitochondria in amyotrophic lateral sclerosis. In *Neuroscience Letters* (Vol. 710). Elsevier Ireland Ltd. https://doi.org/10.1016/j.neulet.2017.06.052

Solleiro-Villavicencio, H., & Rivas-Arancibia, S. (2018). Effect of chronic oxidative stress on neuroinflammatory response mediated by CD4+T cells in neurodegenerative diseases. In *Frontiers in Cellular Neuroscience* (Vol. 12). Frontiers Media S.A. https://doi.org/10.3389/fncel.2018.00114

Stephenson, J., & Amor, S. (2017). Modelling amyotrophic lateral sclerosis in mice. In *Drug Discovery Today: Disease Models* (Vols. 25–26, pp. 35–44). Elsevier Ltd. https://doi.org/10.1016/j.ddmod.2018.10.001

Suk, T. R., & Rousseaux, M. W. C. (2020). The role of TDP-43 mislocalization in amyotrophic lateral sclerosis. In *Molecular Neurodegeneration* (Vol. 15, Issue 1). BioMed Central Ltd. https://doi.org/10.1186/s13024-020-00397-1

Sun, D., Wu, R., Zheng, J., Li, P., & Yu, L. (2018). Polyubiquitin chain-induced p62 phase separation drives autophagic cargo segregation. *Cell Research*, *28*(4), 405–415. https://doi.org/10.1038/s41422-018-0017-7

Takahashi, M., Higuchi, M., Matsuki, H., Yoshita, M., Ohsawa, T., Oie, M., & Fujii, M. (2013a). Stress Granules Inhibit Apoptosis by Reducing Reactive Oxygen Species Production. *Molecular and Cellular Biology*, *33*(4), 815–829. https://doi.org/10.1128/mcb.00763-12

Takahashi, M., Higuchi, M., Matsuki, H., Yoshita, M., Ohsawa, T., Oie, M., & Fujii, M. (2013b). Stress Granules Inhibit Apoptosis by Reducing Reactive Oxygen Species Production. *Molecular and Cellular Biology*, *33*(4), 815–829. https://doi.org/10.1128/mcb.00763-12

Takayama, K. ichi, Suzuki, T., Sato, K., Saito, Y., & Inoue, S. (2024). Cooperative nuclear action of RNA-binding proteins PSF and G3BP2 to sustain neuronal cell viability is decreased in aging and dementia. *Aging Cell*. https://doi.org/10.1111/acel.14316

Tolay, N., & Buchberger, A. (2021). Comparative profiling of stress granule clearance reveals differential contributions of the ubiquitin system. *Life Science Alliance*, *4*(5). https://doi.org/10.26508/LSA.202000927

Truett, G. E., Heeger, P., Mynatt, R. L., Truett, A. A., Walker, J. A., & Warman, M. L. (2000). Preparation of PCR-quality mouse genomic dna with hot sodium hydroxide and tris (HotSHOT). *BioTechniques*, *29*(1), 52–54. https://doi.org/10.2144/00291bm09

Vargas, M. R., Johnson, D. A., Sirkis, D. W., Messing, A., & Johnson, J. A. (2008). Nrf2 activation in astrocytes protects against neurodegeneration in mouse models of familial amyotrophic lateral sclerosis. *Journal of Neuroscience*, *28*(50), 13574–13581. https://doi.org/10.1523/JNEUROSCI.4099-08.2008

Verma, A. (2021). *Amyotrophic Lateral Sclerosis* (Toshiyuki Araki, Ed.; pp. 1–13). Exon Publications.

Vicencio, E., Beltrán, S., Labrador, L., Manque, P., Nassif, M., & Woehlbier, U. (2020). Implications of selective autophagy dysfunction for als pathology. In *Cells* (Vol. 9, Issue 2). Multidisciplinary Digital Publishing Institute (MDPI). https://doi.org/10.3390/cells9020381

Volkening, K., Leystra-Lantz, C., Yang, W., Jaffee, H., & Strong, M. J. (2009). Tar DNA binding protein of 43 kDa (TDP-43), 14-3-3 proteins and copper/zinc superoxide dismutase (SOD1) interact to modulate NFL mRNA stability. Implications for altered RNA processing in amyotrophic lateral sclerosis (ALS). *Brain Research*, *1305*, 168–182. https://doi.org/10.1016/j.brainres.2009.09.105

Wang, B., Maxwell, B. A., Joo, J. H., Gwon, Y., Messing, J., Mishra, A., Shaw, T. I., Ward, A. L., Quan, H., Sakurada, S. M., Pruett-Miller, S. M., Bertorini, T., Vogel, P., Kim, H. J., Peng, J., Taylor, J. P., & Kundu, M. (2019). ULK1 and ULK2 Regulate Stress Granule Disassembly Through Phosphorylation and Activation of VCP/p97. *Molecular Cell*, *74*(4), 742-757.e8. https://doi.org/10.1016/j.molcel.2019.03.027

Wang, J., Gan, Y., Cao, J., Dong, X., & Ouyang, W. (2022). Pathophysiology of stress granules: An emerging link to diseases (Review). In *International Journal of Molecular Medicine* (Vol. 49, Issue 4). Spandidos Publications. https://doi.org/10.3892/ijmm.2022.5099

Wek, R. C. (2018). Role of eIF2α kinases in translational control and adaptation to cellular stress. *Cold Spring Harbor Perspectives in Biology*, *10*(7). https://doi.org/10.1101/cshperspect.a032870

Wiesenfarth, M., Dorst, J., Brenner, D., Elmas, Z., Parlak, Ö., Uzelac, Z., Kandler, K., Mayer, K., Weiland, U., Herrmann, C., Schuster, J., Freischmidt, A., Müller, K., Siebert, R., Bachhuber, F., Simak, T., Günther, K., Fröhlich, E., Knehr, A., … Ludolph, A. C. (2024). Effects of tofersen treatment in patients with SOD1-ALS in a "real-world" setting – a 12-month multicenter cohort study from the German early access program. *EClinicalMedicine*, *69*. https://doi.org/10.1016/j.eclinm.2024.102495

Wils, H., Kleinberger, G., Janssens, J., Pereson, S., Joris, G., Cuijt, I., Smits, V., Ceuterick-De Groote, C., Van Broeckhoven, C., & Kumar-Singh, S. (2010). TDP-43 transgenic mice develop spastic paralysis and neuronal inclusions characteristic of ALS and frontotemporal lobar degeneration. *Proceedings of the National Academy of Sciences of the United States of America*, *107*(8), 3858–3863. https://doi.org/10.1073/pnas.0912417107

Wu, Z., Mei, F., Gan, Y., Liu, A., Hu, J., Jin, Y., & Yin, Y. (2023). FAM69C functions as a kinase for eIF2α and promotes stress granule assembly . *EMBO Reports*, *24*(5). https://doi.org/10.15252/embr.202255641

Xiao, Y., Karam, C., Yi, J., Zhang, L., Li, X., Yoon, D., Wang, H., Dhakal, K., Ramlow, P., Yu, T., Mo, Z., Ma, J., & Zhou, J. (2018). ROS-related mitochondrial dysfunction in skeletal muscle of an ALS mouse model during the disease progression. *Pharmacological Research*, *138*, 25–36. https://doi.org/10.1016/j.phrs.2018.09.008

Xiong, L., McCoy, M., Komuro, H., West, X. Z., Yakubenko, V., Gao, D., Dudiki, T., Milo, A., Chen, J., Podrez, E. A., Trapp, B., & Byzova, T. V. (2022). Inflammation-dependent oxidative stress metabolites as a hallmark of amyotrophic lateral sclerosis. *Free Radical Biology and Medicine*, *178*, 125–133. https://doi.org/10.1016/j.freeradbiomed.2021.11.031

Yamaguchi, M., Omori, K., Asada, S., & Yoshida, H. (2021). Epigenetic regulation of ALS and CMT: A lesson from drosophila models. In *International Journal of Molecular Sciences* (Vol. 22, Issue 2, pp. 1–19). MDPI AG. https://doi.org/10.3390/ijms22020491

Yan, R., Lin, B., Jin, W., Tang, L., Hu, S., & Cai, R. (2023). NRF2, a Superstar of Ferroptosis. In *Antioxidants* (Vol. 12, Issue 9). Multidisciplinary Digital Publishing Institute (MDPI). https://doi.org/10.3390/antiox12091739

Yang, C., Wang, Z., Kang, Y., Yi, Q., Wang, T., Bai, Y., & Liu, Y. (2023). Stress granule homeostasis is modulated by TRIM21-mediated ubiquitination of G3BP1 and autophagy-dependent elimination of stress granules. *Autophagy*, *19*(7), 1934–1951. https://doi.org/10.1080/15548627.2022.2164427

Yang, X., Hu, Z., Fan, S., Zhang, Q., Zhong, Y., Guo, D., Qin, Y., & Chen, M. (2018). Picornavirus 2A protease regulates stress granule formation to facilitate viral translation. *PLoS Pathogens*, *14*(2). https://doi.org/10.1371/journal.ppat.1006901

Yokoyama, H., Yano, R., Kuroiwa, H., Tsukada, T., Uchida, H., Kato, H., Kasahara, J., & Araki, T. (2010). Therapeutic effect of a novel anti-parkinsonian agent zonisamide against MPTP (1-methyl-4-phenyl-1,2,3,6- tetrahydropyridine) neurotoxicity in mice. *Metabolic Brain Disease*, *25*(3), 305–313. https://doi.org/10.1007/s11011-010-9212-z

Yoshioka, D., Nakamura, T., Kubota, Y., & Takekawa, M. (2024). Formation of the NLRP3 inflammasome inhibits stress granule assembly by multiple mechanisms. *Journal of Biochemistry*, *175*(6), 629–641. https://doi.org/10.1093/jb/mvae009

Yun, D., Zhou, L., Shi, J., Li, X., Wu, X., & Sun, F. (2022). G3BP2, a stress granule assembly factor, is dispensable for spermatogenesis in mice. *PeerJ*, *10*. https://doi.org/10.7717/peerj.13532

Zaffagnini, G., Savova, A., Danieli, A., Romanov, J., Tremel, S., Ebner, M., Peterbauer, T., Sztacho, M., Trapannone, R., Tarafder, A. K., Sachse, C., & Martens, S. (2018). p62 filaments capture and present ubiquitinated cargos for autophagy. *The EMBO Journal*, *37*(5). https://doi.org/10.15252/embj.201798308

Zhang, W., Xiao, D., Mao, Q., & Xia, H. (2023). Role of neuroinflammation in neurodegeneration development. In *Signal Transduction and Targeted Therapy* (Vol. 8, Issue 1). Springer Nature. https://doi.org/10.1038/s41392-023-01486-5

Zhang, X., Wang, F., Hu, Y., Chen, R., Meng, D., Guo, L., Lv, H., Guan, J., & Jia, Y. (2020). In vivo stress granule misprocessing evidenced in a FUS knock-in ALS mouse model. *Brain*, *143*(5), 1350–1367. https://doi.org/10.1093/brain/awaa076

Zhao, C. (2023). Cell culture: in vitro model system and a promising path to in vivo applications. In *Journal of Histotechnology* (Vol. 46, Issue 1, pp. 1–4). Taylor and Francis Ltd. https://doi.org/10.1080/01478885.2023.2170772

Zhao, W., Beers, D. R., Bell, S., Wang, J., Wen, S., Baloh, R. H., & Appel, S. H. (2015). TDP-43 activates microglia through NF-κB and NLRP3 inflammasome. *Experimental Neurology*, *273*, 24–35. https://doi.org/10.1016/j.expneurol.2015.07.019

Zuo, X., Zhou, J., Li, Y., Wu, K., Chen, Z., Luo, Z., Zhang, X., Liang, Y., Esteban, M. A., Zhou, Y., & Fu, X. D. (2021). TDP-43 aggregation induced by oxidative stress causes global mitochondrial imbalance in ALS. *Nature Structural and Molecular Biology*, *28*(2), 132–142. https://doi.org/10.1038/s41594-020-00537-7

Appendix

Table 4 – Statistical Test Results

Target	Group Information	N		Mean ± SEM	Significance	P value	Test
		N1	N2				
G3BP2 Expression in Motor Neurons (late symptomatic)							Figure 16
G3BP2	Tg/Tg SPC vs NTg SPC	4	4	0.1804 ± 0.04686 vs 0.02130 ± 0.0.04686	*	0.0146	unpaired two-tailed t-test
TiaR Expression (late symptomatic)							Figure 19
TiaR	50kDa SPC Tg/Tg vs NTg	3	4	0.7654 ± 0.1775 vs 1.000 ± 0.1775	ns	0.2436	unpaired two-tailed t-test
	40kDa SPC Tg/Tg vs NTg	3	4	1.455 ± 0.1412 vs 1.000 ± 0.1412	*	0.0234	
	50 kDa Brain Tg/Tg vs NTg	3	6	1.220 ± 0.7829 vs 1.000 ± 0.7829	*	0.0260	
	42kDa Brain Tg/Tg vs NTg	3	6	1.112 ± 0.1726 vs 1.000 ± 0.1726	ns	0.5384	
Stress Granule Transcription (late symptomatic)							Figure 22
G3BP1 transcription	SPC Tg/Tg vs NTg	4	4	2.078 ± 0.417 vs 1.048 ± 0.417	*	0.0484	unpaired two-tailed t-test
HuR transcription	SPC Tg/Tg vs NTg	4	4	0.7085 ± 0.1226 vs 1.012 ± 0.1226	*	0.0481	

Tia1 transcription	SPC Tg/Tg vs NTg	4	4	0.8520 ± 0.08257 vs 1.007 ± 0.08257	ns	p = 0.1100	
Stress Granule Expression and Transcription (early symptomatic)							Figure 24
TiaR Expression	50kDa SPC Tg/Tg vs NTg	3	3	0.8365 ± 0.1229 vs 1.000 ± 0.1229	ns	0.2542	unpaired two-tailed t-test
	42kDa SPC Tg/Tg vs NTg	3	3	0.7731 ± 0.1965 vs 1.000 ± 0.1965	ns	0.3124	
	50kDa Brain Tg/Tg vs NTg	3	3	1.154 ± 0.1305 vs 1.000 ± 0.1305	ns	0.3029	
	42 kDa Brain Tg/Tg vs NTg	3	3	1.198 ± 0.2243 vs 1.000 ± 0.2243	ns	0.4265	
G3BP1 transcription	SPC Tg/Tg vs NTg	4	4	1.149 ± 0.1572 vs 1.008 ± 0.1572	ns	0.4042	
HuR transcription	SPC Tg/Tg vs NTg	3	3	0.9073 ± 0.2218 vs 1.030 ± 0.2218	ns	0.6097	
Tia1 transcription	SPC Tg/Tg vs NTg	3	3	0.9543 ± 0.2281 vs 1.032 ± 0.2281	ns	0.7516	
Iba1 Expression (late symptomatic)							Figure 25
Iba1+ Manual Counts	SPC Tg/Tg vs NTg	4	5	194.4 ± 11.15 vs 134.1 ± 11.15	*	0.0010	unpaired two-tailed t-test
Iba1+ Particle Area	SPC Tg/Tg vs NTg	4	5	55192 ± 4640 vs 40182 ± 4640	*	0.0144	
NrF2-ARE transcription							Figure 27

HMOX1	SPC Tg/Tg vs NTg	4	4	3.026 ± 0.2290 vs 1.001 ± 0.2290	*	0.0001	unpaired two-tailed t-test
NQO1	SPC Tg/Tg vs NTg	4	4	1.914 ± 0.1644 vs 1.014 ± 0.1644	*	0.0016	
NrF2	SPC Tg/Tg vs NTg	4	4	1.050 ± 0.1485 vs 1.007 ± 0.1485	ns	0.7819	
GCLM	SPC Tg/Tg vs NTg	4	4	2.150 ± 0.1583 vs 1.003 ± 0.1583	*	0.0004	
CytC	SPC Tg/Tg vs NTg	4	4	0.9303 ± 0.09414 vs 1.005 ± 0.09414	ns	0.4603	
GCLC	SPC Tg/Tg vs NTg	4	4	1.724 ± 0.4534 vs 1.073 ± 0.4534	ns	0.2012	
KEAP1	SPC Tg/Tg vs NTg	4	4	1.303 ± 0.8879 vs 1.049 ± 0.8879	ns	0.3641	
MRP1	SPC Tg/Tg vs NTg	4	4	1.193 ± 0.2110 vs 1.026 ± 0.2110	ns	0.4581	
NLRP3 Expression (late symptomatic)							Figure 28
NLRP3	SPC Tg/Tg vs NTg	4	4	2.035 ± 0.2095 vs 1.039 ± 0.2095	**	0.0031	unpaired two-tailed t-test
Reactive Oxygen Species Transcription							Figure 30
mXO	SPC Tg/Tg vs NTg	4	4	4.417 ± 0.5736 vs 1.021 ± 0.5736	**	0.0010	unpaired two-tailed t-test
SOD2	SPC Tg/Tg vs NTg	4	4	1.308 ± 0.3287 vs	ns	0.5469	

				1.098 ± 0.3287			
Autophagy Expression (late symptomatic)							Figure 31
ULK1	SPC Tg/Tg vs NTg	3	4	0.4411 ± 0.2379 vs 1.000 ± 0.2379	ns	0.0656	unpaired two-tailed t-test
	BR Tg/Tg vs NTg	4	6	1.313 ± 0.2741 vs 1.000 ± 0.2741	ns	0.2864	
p62	SPC Tg/Tg vs NTg	3	4	0.8559 ± 0.3005 vs 1.000 ± 0.3005	ns	0.6517	
	BR Tg/Tg vs NTg	4	6	0.8034 ± 0.1944 vs 1.000 ± 0.1944	ns	0.3416	
Beclin	SPC Tg/Tg vs NTg	3	4	0.8288 ± 0.09235 vs 1.000 ± 0.09235	ns	0.1229	
	BR Tg/Tg vs NTg	4	6	0.9139 ± 0.1005 vs 1.000 ± 0.1005	ns	0.4169	
LC3B II/I	SPC Tg/Tg vs NTg	3	4	0.9792 ± 0.1991 vs 1.035 ± 0.1991	ns	0.7887	
	BR Tg/Tg vs NTg	4	6	0.6410 ± 0.1065 vs 1.001 ± 0.1065	*	0.0096	
Autophagy Expression (late symptomatic)							Figure 32
ULK1	BR Tg/Tg vs NTg:			0.4685 ± 0.1690 vs 1.000 ± 0.1690	*	0.0347	
Beclin	BR Tg/Tg vs NTg			0.7325 ± 0.03547 vs 1.000	**	0.0017	

				± 0.03547			unpaired two-tailed t-test
P62	BR Tg/Tg vs NTg			0.8319 ± 0.07502 vs 1.000 ± 0.07502	ns	0.0885	
LC3B II/I	BR Tg/Tg vs NTg			1.001 ± 0.2068 vs 1.000 ± 0.2068	ns	0.9951	
G3BP2 Expression in Motor Neurons following Terazosin treatment (late symptomatic) Figure 33							
	NTg Saline vs Tg/Tg Saline	4	4	0.05870 ± 0.05569 vs 0.3024 ± 0.03082	*	0.0305	one way ANOVA with post-hoc Tukey’s multiple comparisons
	NTg saline vs Tg /Tg terazosin	4	5	0.05870 ± 0.05569 vs 0.2006 ± 0.06314	ns	0.1983	
	Tg/Tg Saline vs Tg/Tg Terazosin	4	5	0.3024 ± 0.03082 vs 0.2006 ± 0.06314	ns	0.4064	

Figure 36 – Western Blot Gels

☐ Representative band and TPS used ☐ Tg/0 genotype not included in analysis

TiaR P15 P19 SPC

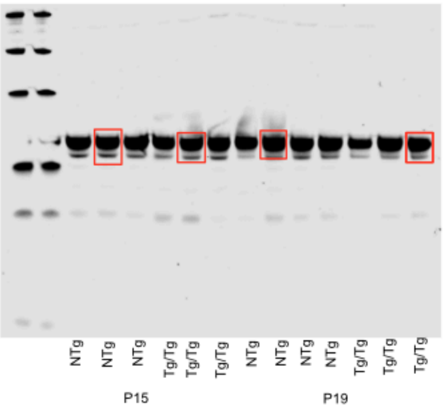

TPS

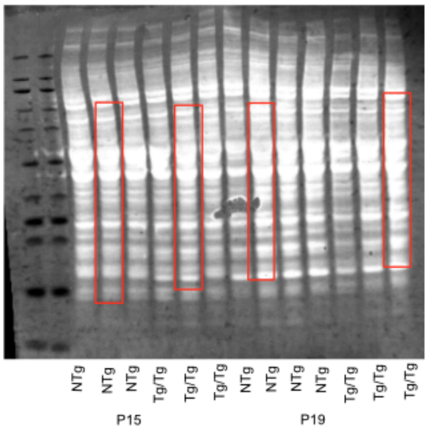

TiaR P15 P19 BR

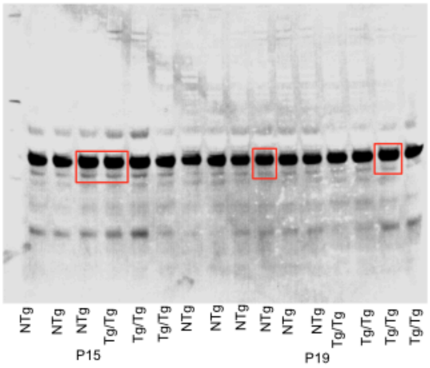

TPS

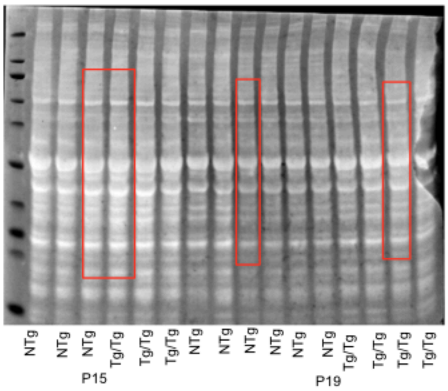

G3BP2 P15 SPC

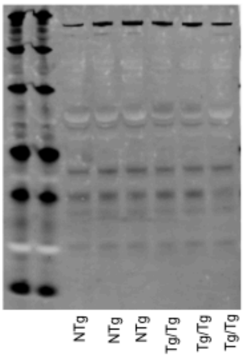

TPS

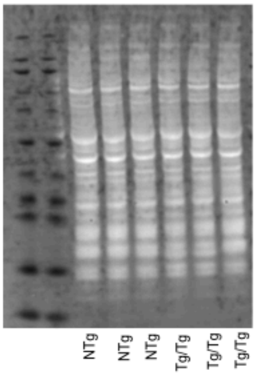

G3BP2 P19 SPC

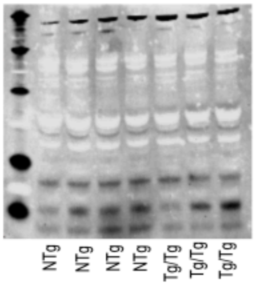

TPS

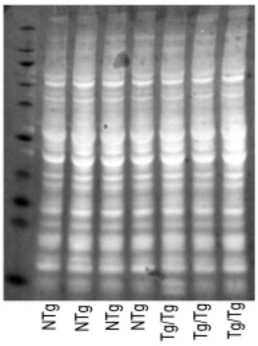

☐ Representative band and TPS used ☐ Tg/0 genotype not included in analysis

G3BP1 P15 SPC

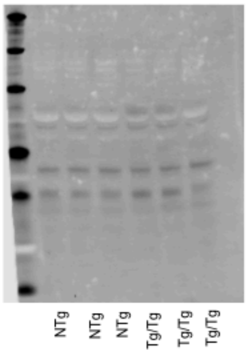

TPS

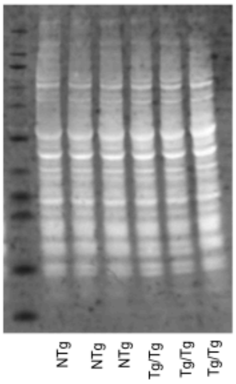

G3BP1 P19 SPC

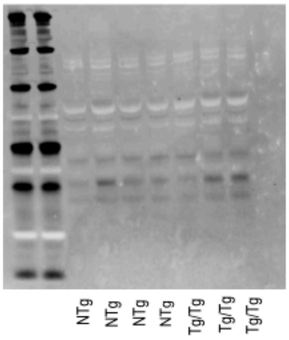

TPS

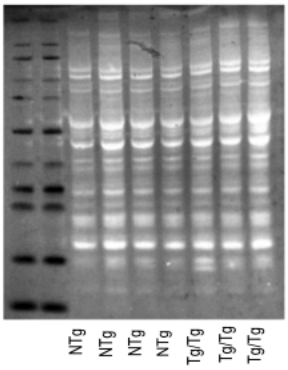

ULK1 Clinical Endstage BR

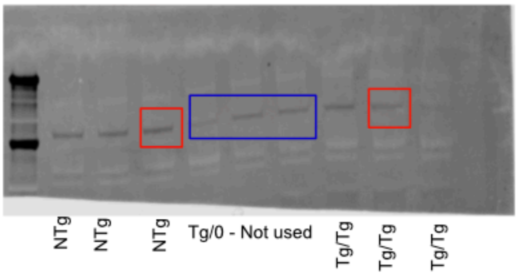

TPS

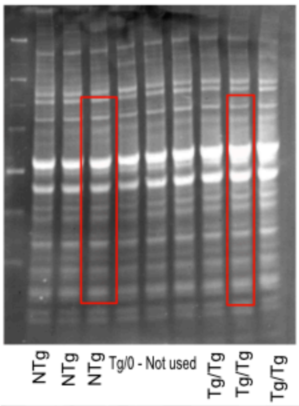

p62 Clinical Endstage BR

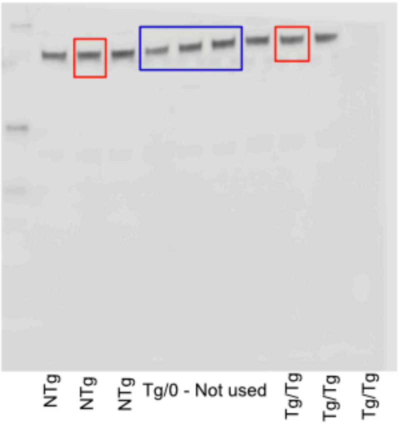

TPS

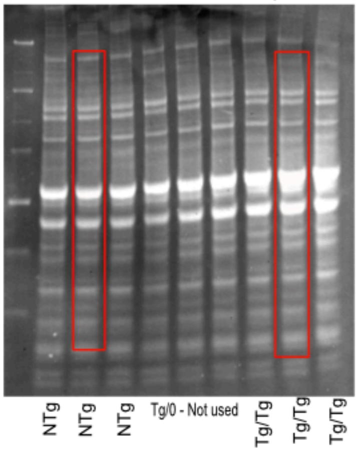

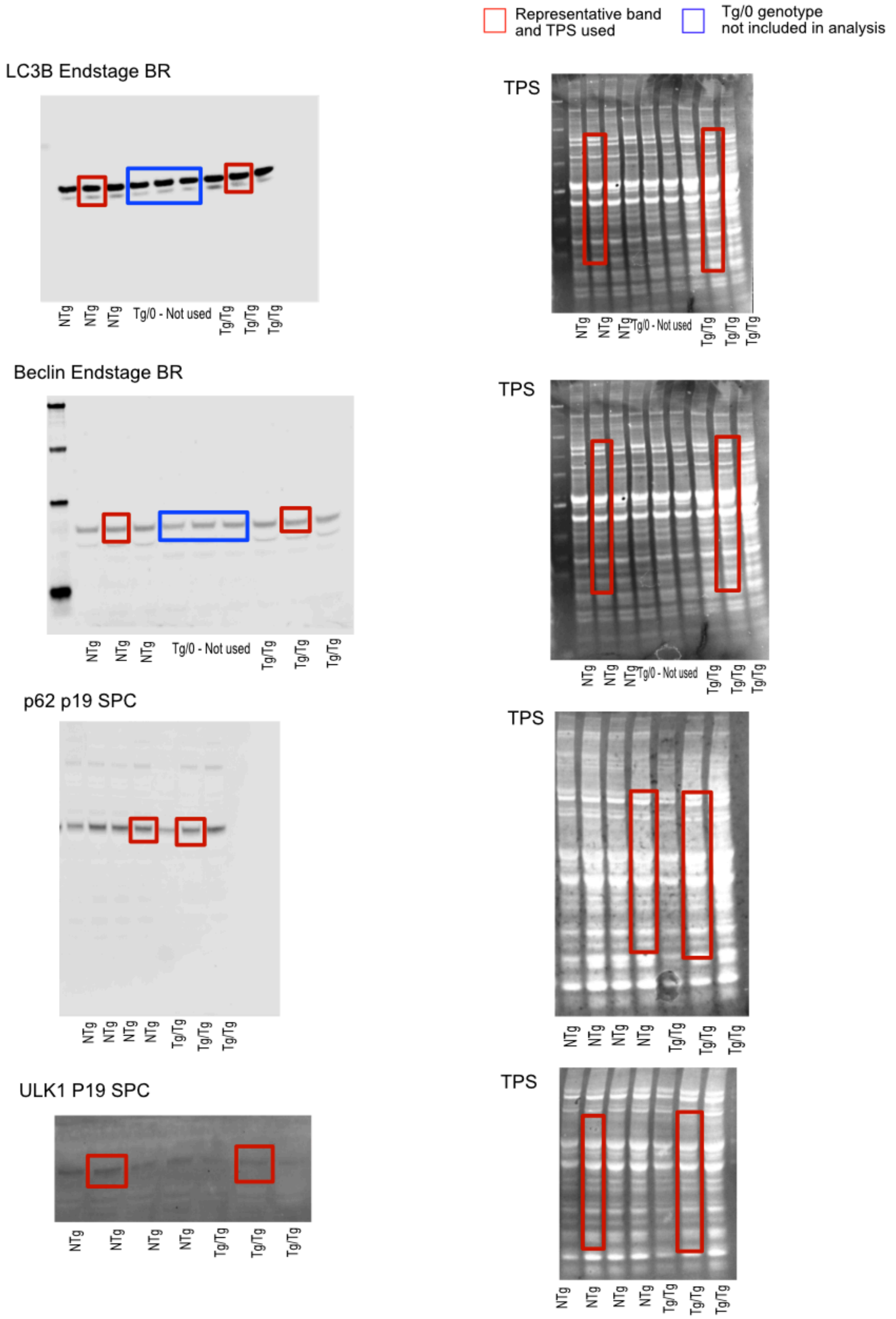
Representative band and TPS used
Tg/0 genotype not included in analysis
LC3B Endstage BR
NTg
NTg
NTg
Tg/0 - Not used
Tg/Tg
Tg/Tg
Tg/Tg
TPS
NTg
NTg
NTg
Tg/0 - Not used
Tg/Tg
Tg/Tg
Tg/Tg
Beclin Endstage BR
NTg
NTg
NTg
Tg/0 - Not used
Tg/Tg
Tg/Tg
Tg/Tg
TPS
NTg
NTg
NTg
Tg/0 - Not used
Tg/Tg
Tg/Tg
Tg/Tg
p62 p19 SPC
NTg
NTg
NTg
NTg
Tg/Tg
Tg/Tg
Tg/Tg
TPS
NTg
NTg
NTg
NTg
Tg/Tg
Tg/Tg
Tg/Tg
ULK1 P19 SPC
NTg
NTg
NTg
NTg
Tg/Tg
Tg/Tg
Tg/Tg
TPS
NTg
NTg
NTg
NTg
Tg/Tg
Tg/Tg
Tg/Tg

🟥 Representative band and TPS used

🟦 Tg/0 genotype not included in analysis

Beclin Br P19

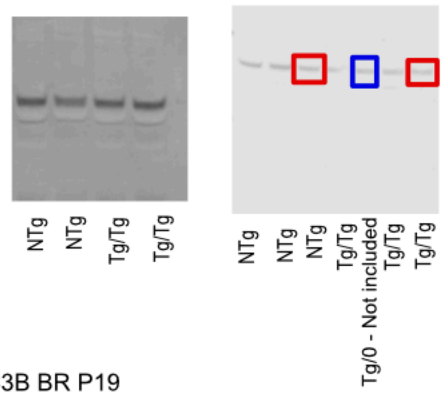

TPS

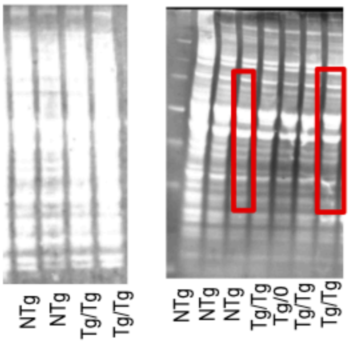

LC3B BR P19

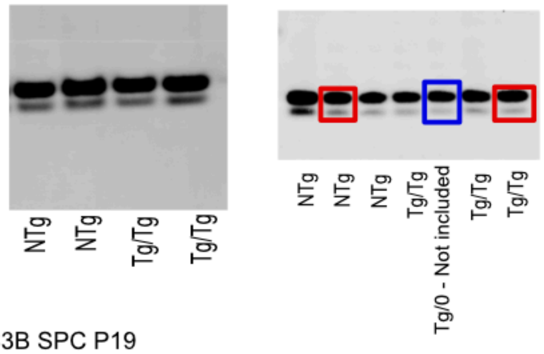

TPS

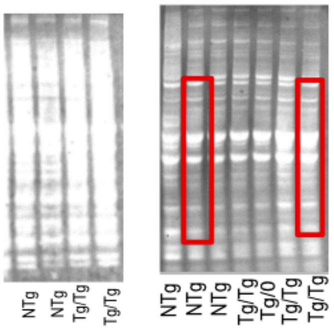

LC3B SPC P19

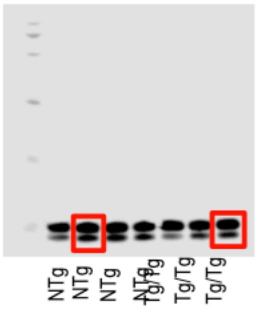

TPS

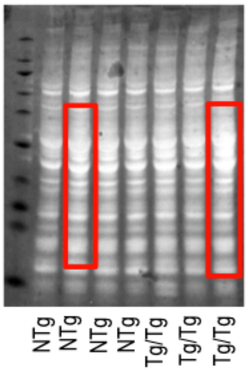

Beclin SPC P19

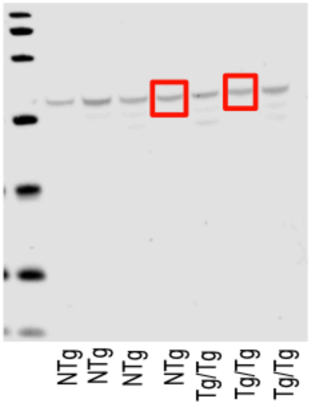

TPS

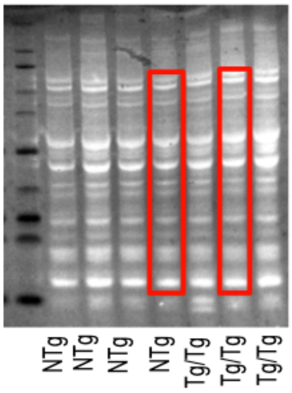

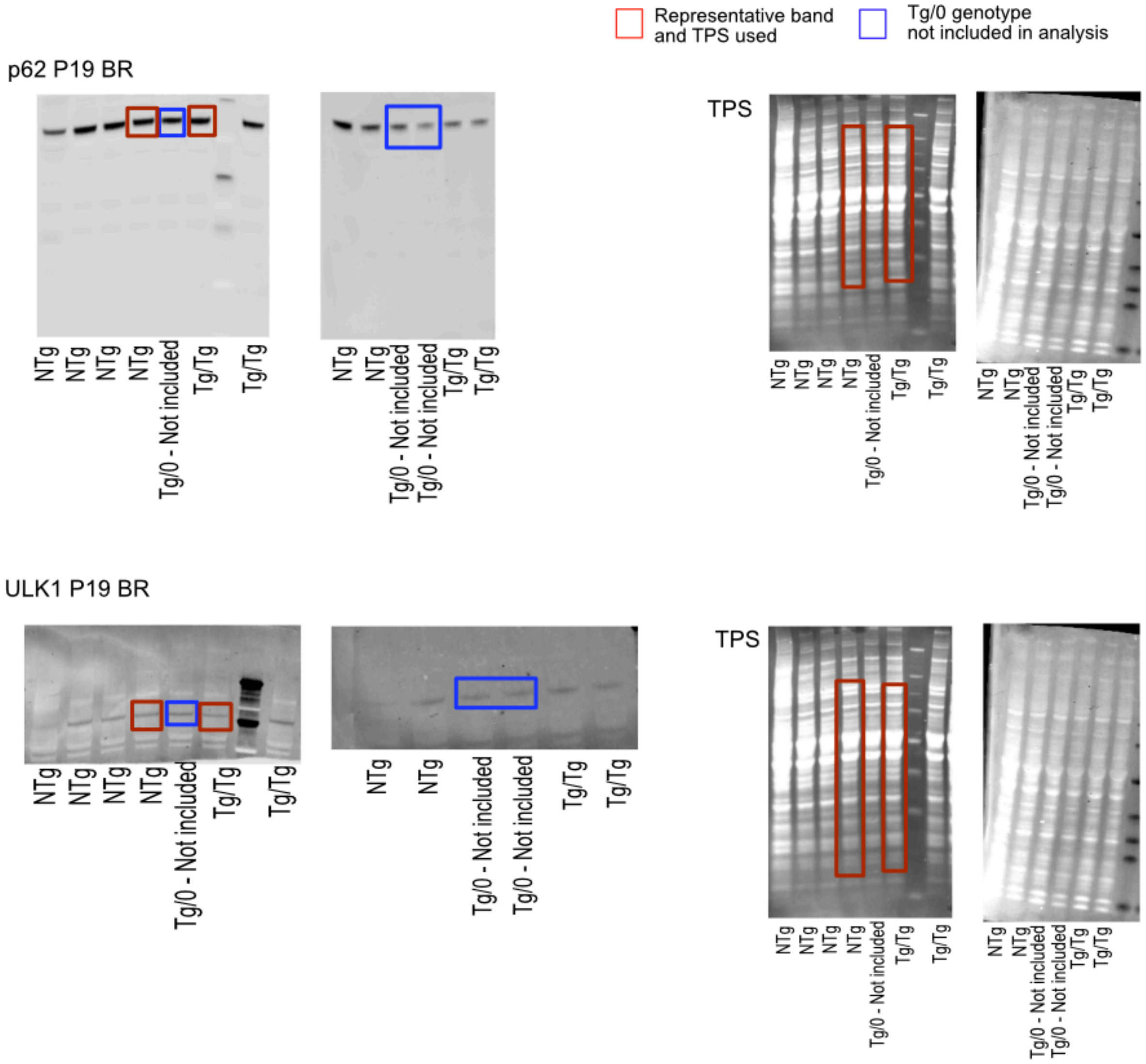

Figure 36: Western Blot Gels showing selected antigen-specific and TPS channels for figures. Red box indicates antigen specific and TPS band used in figure. Blue box shows Tg/0 mice. This genotype was not included in analysis due to insufficient sample size.

Figure 37

qPCR Optimisation Gels

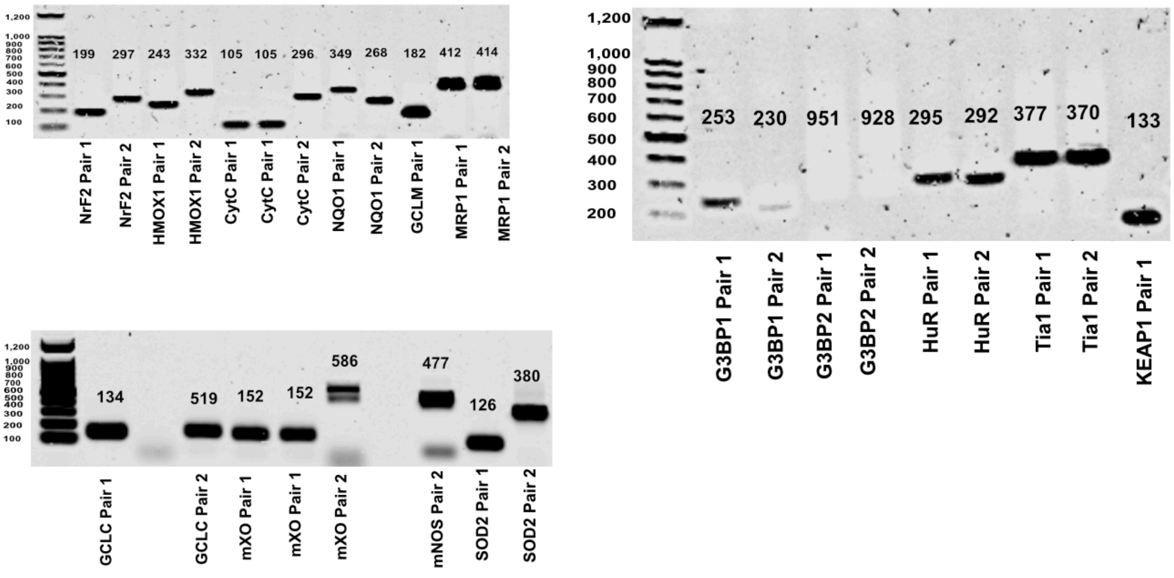

qPCR Gels

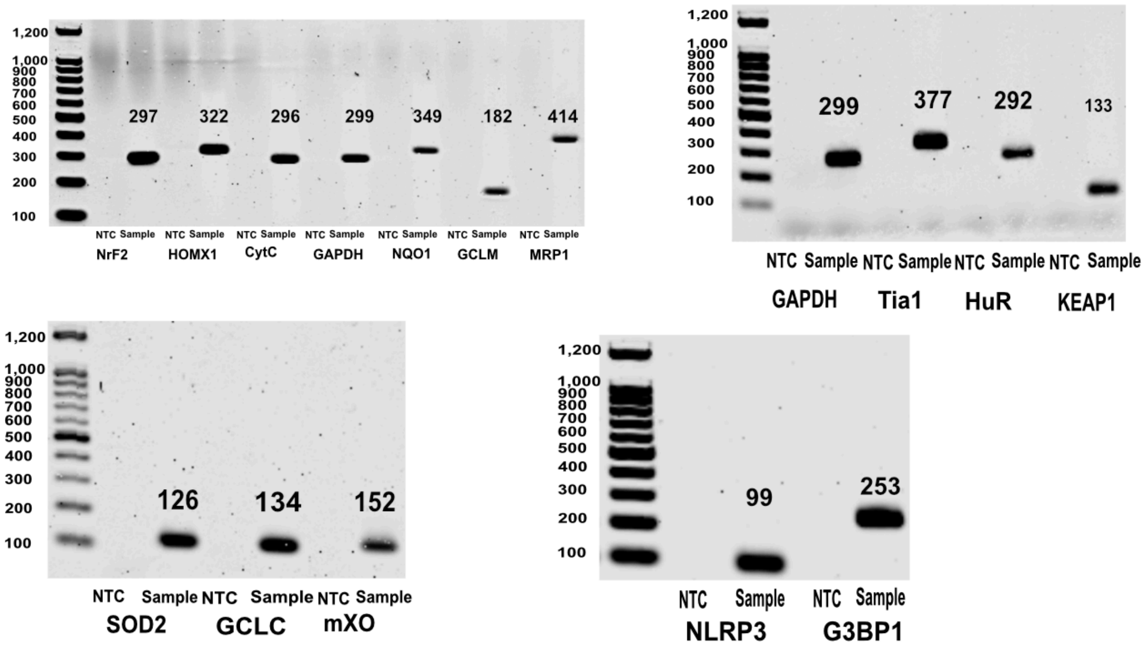

Figure 37: qPCR optimisation and confirmation gel.